Probing the properties of dark matter particles with astrophysical observations

Magalich, A.

Chapter 5

Lyman-α forest and Warm Dark Matter[1]

5.1 Introduction and summary

As we saw in the previous section, ΛCDM cosmology provides an excellent description of the observed Large Scale Structure in the Universe. It also describes very well statistical properties of the CMB, relating the temperature fluctuations detected in the CMB to the density fluctuations in the distribution of galaxies (see *e.g.* [100] for a recent description). Non-baryonic "dark matter" is a crucial ingredient of the Standard Cosmological model, reconciling the low amplitude of the temperature fluctuations in the CMB with the high amplitude of fluctuations detected in the total matter density inferred from the clustering of galaxies (see Chapters 1 and 4).

However, the detailed properties of the DM particle have little impact on the success of the ΛCDM model on large scales. As we have discussed in Chapter 1, depending on the production mechanism of Dark Matter particles in the Early Universe, initial (i.e. primordial) DM velocities may strongly suppress the amplitude of matter fluctuations on scales below a characteristic *free streaming horizon*, $\lambda_{\rm FS}$ that is more often called 'free-streaming length'(see *e.g.* the discussion by [133]). This quantity is defined in the usual way (see also Section 1.1.1 for details):

$$\lambda_{\rm FS}(t) \equiv a(t) \int_{t_i}^{t} d\tau \, \frac{v(\tau)}{a(\tau)}. \tag{5.1.1}$$

In CDM model the free streaming length in negligible, but for *Warm Dark Matter* $\lambda_{\rm FS}$ can be of the order of a co-moving megaparsec. Particle physics candidates for Warm and Cold DM can be very different from the point of view of the particle physics (masses

[1] Results of this chapter are presented in papers [1, 2]. The main contributions of Andrii Magalich are a new set of cosmological simulations exploring reionization scenarios in CDM and WDM cosmologies as well as construction of physical Lyman-α forest observables like mock quasar spectra and Flux Power Spectra (in collaboration with Antonella Garzilli).

of particles, generation mechanisms, quantum properties, etc.). But for Cosmology the difference between them could be seen only on the smallest scales – WDM shares all the success of CDM at large scales!

Therefore, it is a very important fundamental problem for physics in general to identify ways to distinguish between Cold and Warm Dark Matter observationally. In this section, we discuss one promising approach to do this – the *Lyman-α forest* method – and its current results.

The effects of free-streaming on structure formation may be detectable if $\lambda_{\rm FS}$ is larger than tens of comoving kpc. At smaller scales the effects are completely obscured by baryons and from practical point of view such WDM models are indistinguishable from CDM. To constrain WDM models there are, essentially, 3 main approaches:

1. Determine the number of collapsed structures as a function of their masses and redshifts. A large value of $\lambda_{\rm FS}$ will also dramatically reduce the abundance of low-mass DM halos (see *e.g.* [134, 135]) and consequently also of the low-mass ('dwarf') galaxies they host. The abundance of Milky Way satellites, for example, therefore provides interesting limits on $\lambda_{\rm FS}$ [136, 137]. However the impact of relatively poorly understood baryonic physics may ultimately limit the constraining power of both methods. Methods that are largely free from such uncertainties are therefore more promising; these include gravitational lensing by low-mass halos [138], and the creation of gaps in stellar streams by the tidal effects of a passing dark matter subhalo [139].

2. Determine the distribution of matter within individual DM-dominated objects (cores in galactic halos). Particle free-streaming introduces a maximum phase-space density of fermionic DM which could potentially cause Dark Matter halos to have a central density 'core' [140–142]. The smallness of such a core [142], and the potential for baryonic processes associated with star formation and gas cooling to affect the central density profile (see *e.g.* [143–145]), render this route to determining $\lambda_{\rm FS}$ challenging [146]. We shall not discuss this question in the current review and refer an interested reader to [147].

3. Measurement of the matter power spectrum at small scales. In the work we concentrate on studying statistical properties of DM distribution at small scales. As it was mentioned in Chapter 4, apart from halos of galaxies and clusters, DM forms also filamentary (one dimensional) structures that are organised into the so-called *Cosmic Web* (see Fig. 1.5). In Section 5.2 we briefly describe how the properties of the Cosmic Web differ in the cases of Cold, Warm and Hot Dark Matter and conclude that we would like to observe the effect of WDM on the Matter Power Spectrum (defined in Section 4.2)

The Cosmic Web of Dark Matter is traced by baryons. At large scales (super-Mpc) the distribution of galaxies (Fig. 4.1) follows the Cosmic Web. At smaller scales, the

Cosmic Web is traced by the so-called *Intergalactic Medium* (IGM). The IGM is largely of primordial composition, being constituted by Hydrogen and Helium, with the occasional pollution by metals (all elements beyond Helium). In particular, in Section 5.3 we discuss how we can observe the IGM through its neutral Hydrogen component.

In Section 5.4 we discuss to what extent Hydrogen follows the distribution of Dark Matter. We conclude that thermal effects caused by the formation of first stars and re-ionisation of Hydrogen can prevent it from following the distribution of Dark Matter at small scales and therefore mimic the effect of free-streaming of DM particles, creating therefore major systematic uncertainty for the whole approach. We briefly review what is known about the thermal history of Hydrogen.

We proceed in Section 5.5 by discussing that the distribution of Hydrogen can be observed through its imprints in absorption in the spectra of distant and bright sources. For example, the transitions of an electron between the ground and excited states of neutral Hydrogen are collectively called the *Lyman series* (with the individual transitions from the ground level to the excited ones called Lyman-α, -β, -γ, etc.). Neutral Hydrogen absorbs the light of a distant source (like quasars) and imprints *absorption lines* in the spectrum. The Lyman-α absorption happens in the ultraviolet, at 1215.67 Å. Since the light is traveling a large distance between the quasar and the Earth, it gets redshifted and characteristic quasar spectrum develops a set of absorption features at the locations of the intervening neutral Hydrogen (this happens if, like is the case, the intervening Hydrogen is highly ionized, being the Lyman-α transition sensitive at very small neutral Hydrogen fraction). A collection of these absorption features is called the *Lyman-α forest*.

The Fourier transform of the auto-correlation function of the spectra gives rise to the *Flux Power Spectrum* (FPS) – the main observable of the method (Section 5.6). A generic prediction of the WDM influence in the Lyman-α forest is the cutoff in the FPS at small scales.

The spatial scales that the Lyman-α forest method probes are directly proportional to the spectral resolution of the observing instrument. Initial, medium and low resolution spectra did not exhibit any suppression (the spectrum was rising as CDM would predict; see Section 5.6.2). In this situation the WDM bounds were derived from potential (within statistical error bars) deviation of the observed power spectrum from the one, predicted by the CDM (see e.g. [133, 148, 149]).

The situation has changed recently, when a few high-resolution and high-redshift quasar spectra became available [150, 151]. These data exhibit a very clear cutoff around $k \sim 0.03\,\mathrm{s/km}$ (see Fig. 5.14; for details on units used in spectroscopy, refer to Sec. 5.6). This does not mean, however, that Warm Dark Matter with $\lambda_{\rm DM} \sim \lambda_{\rm FS}$ has been discovered! In Section 5.7 we discuss the interpretation of the available data and physical conclusions about the nature of Dark Matter that could be derived from them.

We discuss there that the observed suppression can be mimicked by a number of thermal effects. This can make the data consistent with CDM. In particular, the Doppler broadening introduces its own cutoff, related to the instantaneous temperature of the intergalactic

medium (IGM), while the history of re-ionisation and of the IGM heating manifests itself via another cutoff ("pressure effects"). This, in turn, does not also mean that the "CDM + thermal effects" interpretation of the data is correct. Assuming different (but not excluded neither experimentally nor theoretically) thermal histories of IGM, one could interpret the available data to exclude CDM or to constrain WDM very strongly. We briefly discuss in what way the uncertainty could be removed and how one can use these data before that.

The Lyman-α constraints can be interpreted in terms of constraints on particle physics models. Often 'WDM' refers to a somewhat unphysical scenario where DM is produced in thermal equilibrium and then freezes out while still being relativistic – *(warm) thermal relic* or *thermal WDM* [152]. In this case there is a one-to-one relation between $\lambda_{\rm DM}$ and the DM particle mass, $m_{\rm WDM}$ ($\lambda_{\rm DM} \propto m_{\rm WDM}^{-4/3}$), see *e.g.* [153]. Although it does not correspond to any particular particle physics model, this parametrization is often chosen when deriving WDM constraints and therefore we will refer to it throughout this Chapter.

Many particle physics candidates can play the role of Warm Dark Matter (including axinos [154, 155], gravitinos [156], sterile neutrinos [54], etc.). The focus of this thesis is on a particular DM candidate – *sterile neutrinos, resonantly produced in the presence of a lepton asymmetry* [157, 158]. If such a sterile neutrino (SN in what follows) is sufficiently light (masses of the order $m_{\rm DM}c^2 \approx {\rm keV}$), the 3D linear matter power spectrum exhibits a cutoff below a scale $\lambda_{\rm FS}$ that is a function of two parameters: the mass of the DM particle, $m_{\rm DM} \equiv m_{\rm SN}$, and the primordial lepton asymmetry parameter that governs its resonant production, L_6 (see e.g. [136, 153, 158]); see *e.g.* [54] for a review on keV sterile neutrinos as a DM candidate (see also Section 2.1).

5.2 Cosmic web and Warm Dark Matter

How to distinguish between Cold and Warm Dark Matter? In CDM the clumps of DM of all sizes are possible (up to some very small clumps with masses below one solar mass [159]). Hence there should be a lot of small-mass substructures in the Cosmic Web. If DM is not cold, but has significant free-streaming, it can affect the structure formation and the number of structures that are smaller than the free streaming length is strongly suppressed. So, to distinguish between CDM and WDM it is enough to count the number of small structures. Yet another possibility is that WDM can modify properties of the DM halos themselves.

WDM observation in DM halos. Several features can be signatures of WDM (see e.g. [160] for a review):

1. **Missing satellites problem** – fewer amount of dwarf galaxies are observed in the Milky Way and M31 than CDM predicts [161–163];

2. **Core-cusp problem** – pure CDM simulations predict behavour of the DM density in the central part of haloes $\rho \propto r^{-\alpha}$ with $\alpha \approx 1$. However, it is claimed that for many objects $\alpha < 1$ describes observational data much better [164, 165];

3. **Too-big-to-fail problem** – large satellites with the maximum circular velocity $V_{\max} > 30\,\mathrm{km/s}$ should contain stars and be observed. However, the naive CDM prediction for the number of such objects in the Milky Way (~ 10) is in a tension with the fact that only 3 such objects were detected [166, 167].

All these problems, however, can be solved within CDM if one takes into account observational uncertainties, baryonic effects and variance in the initial conditions [168–172]. So, to confidently distinguish between CDM and WDM we need to look at the number of small dark halos, that are not so affected by baryonic effects, variance, etc.

The main difficulty is that small haloes may be very difficult to observe. Indeed, for a halo to be visible now it is important that at the early stage of the halo evolution it confines gas and eventually stars are formed. At the same time, if primordial hydrogen is already hot at the time of halo formation, it can fall into a halo only if this halo is massive enough. Primordial hydrogen is heated during reionization by the light of first stars. We do not know exactly to what temperature it is heated. But in simulations, this temperature can be large enough such that we can expect that small haloes cannot confine the gas and today they are made only of DM [172].

There are some clever ideas how to observe these small dark halos using the gravitational lensing. There are two possible methods: search for the perturbations in Einstein rings [173] or look at the flux ratios of multiply-imaged sources [174–176] that can be significantly increased because of the small haloes passing in front of the image. In 2022, the new telescope Euclid will be launched and will provide enough data to observe or constrain the number of small dark halos [177, 178]. This means that very soon we will either significantly constrain WDM or find a very strong evidence for it.

The study of gravitational lensing is a promising approach that does not depend on the optical visibility of the structures and not as much on the high-resolution hydrodynamical simulations. This would allow either to rule out CDM or to constrain WDM very significantly.

WDM observation in Cosmic Web. Apart from dark matter distribution in the individual haloes, it is possible to infer the free-streaming of DM particles from the structures of the Cosmic Web. At high redshifts the structures of interesting sizes are still not so far from the linear regime ($\delta\rho/\rho$ is not much greater than 1). Also, at larger redshifts we are observing larger volumes within the same solid angle. This is another advantage over the galaxy-scale measurements as the amount of observed structures is much greater.

Structure of the Cosmic Web at small scales can discriminate between Cold and Warm Dark Matter models.

If DM is cold, its power spectrum to be featureless and defined by a few fundamental parameters at the matter-radiation equality epoch. The Matter Power Spectrum is given by:

$$\begin{cases} P(k < k_{eq}) = Ak \\ P(k > k_{eq}) = B\frac{\ln k^2}{k^3} \end{cases} \tag{5.2.1}$$

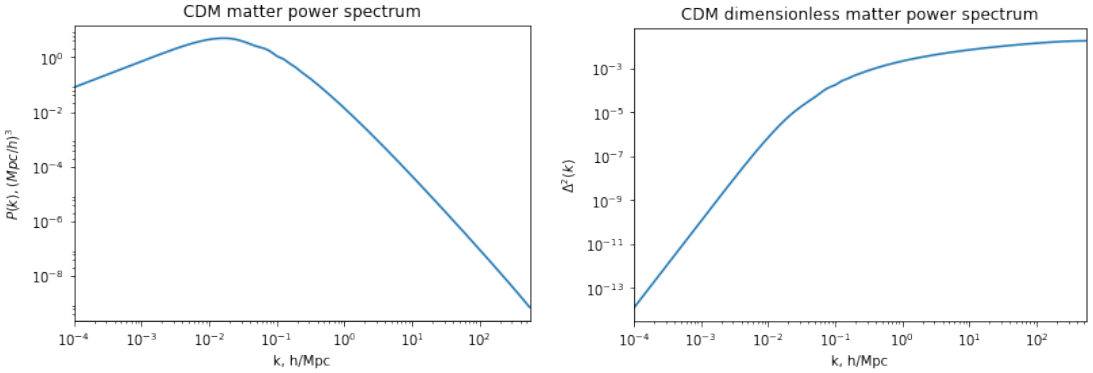

Figure 5.1: CDM Matter Power Spectrum $P(k)$ and dimensionless Matter Power Spectrum $\Delta^2(k)$

For convenience we also introduce dimensionless Matter Power Spectrum $\Delta^2(k)$:

$$\Delta^2(k) = \frac{k^3 P(k)}{2\pi^2} \tag{5.2.2}$$

$$\begin{cases} \Delta^2(k < k_{eq}) = \frac{Ak^4}{2\pi^2} \\ \Delta^2(k > k_{eq}) = \frac{B\ln k^2}{2\pi^2} \end{cases} \tag{5.2.3}$$

However if DM is warm, below some scales the number of structures will quickly decrease and therefore we expect a *cutoff* in the $P(k)$. The location and the shape of cutoff depends on the particular properties of DM particles (Fig. 5.2).

The effect of WDM on the close-to-linear scales is the suppression of small-scale correlations caused by DM particle free-streaming (see Fig. 1.5). Our goal should be therefore to detect such a cutoff of DM power spectrum.

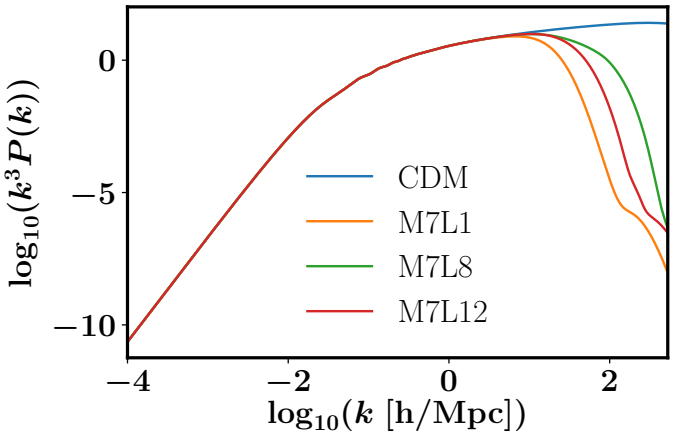

Figure 5.2: Matter Power Spectrum in CDM and various sterile neutrino WDM cosmologies. Sterile neutrinos with mass of $m_{SN} = 7\,\mathrm{keV}$ and lepton asymmetry numbers $L_6 = 1, 8, 12$ are shown.

5.3 Cosmic Web and neutral Hydrogen

Unlike galaxies that make the large-scale Cosmic Web visible, the IGM gas by itself does not shine. Indeed, the average IGM density is sufficiently low for virtually no star formation to take place there.[2] While it is not possible to observe IGM *in emission*, it may be possible to observe it *in absorption*. For this we would need a background 'flashlight'to illuminate the structures. In particular, we can observe the IGM via absorption features in the spectra of very bright and distant objects, typically quasars. In the future, it may be possible to revealing the IGM through the 21cm line in absorption or emission [182].

IGM absorption signal is due to neutral Hydrogen – the strong absorber and the most ubiquitous element in the Universe. In order to learn from these absorption features about the Dark Matter distribution, one should understand at what scales/redshifts does neutral hydrogen follow the Dark Matter.

5.3.1 The timeline

Naively, the evolution of hydrogen and Dark Matter do not have much in common. Indeed

– In radiation-dominated epoch DM density perturbations grow (at a slow logarithmic pace) while protons are tightly coupled with photons and support sound waves, rather than experience gravitational instability.

[2]We will discuss later that in some WDM cosmologies it may actually be possible to produce stars in the intergalactic filaments [179, 180]. Alternatively, it may be possible to observe the part of the IGM closer to the galaxies in fluorescent emission [181]. However, for most of the part IGM is not actively emitting.

– After matter-radiation equality DM begins to cluster faster, but baryonic plasma is still interacting rapidly with radiation. Its density perturbations remain small $\delta_b \sim 10^{-5}$ and temperature follows $T \propto a^{-1}$.

– At $z \sim 1000$ baryonic plasma recombines into neutral hydrogen. Although interaction between neutral gas and photons is much weaker than in plasma, the number density of CMB photons is enough to keep the temperature of atoms the same as CMB temperature.

– Around $z \sim 100$ the CMB-baryon scattering is inefficient and the gas becomes independent of CMB. From this point, it is cooling more quickly than photons, as $T \propto a^{-2}$. This allows matter perturbations to catch up with DM. From this point on, gas is following DM.

– At later times, first stars and galaxies form, creating highly non-linear objects and sources of heat and ionizing background.

– When the amount of ionizing radiation becomes significant to affect the ionization balance of the Universe, it triggers the event of Reionization. Relatively quickly gas becomes highly ionized except for in dense collapsed structures. The temperature reaches $\sim 10^4$ K.

5.4 Thermal history of the Intergalactic Medium

The most obvious difference between DM and baryons lies in interactions. The self-interaction cross-section of DM is limited at the level of $\sigma/m_{DM} < 1\,\mathrm{cm}^2/\mathrm{g}$ [183] and interaction with the Standard Model is constrained to be many orders of magnitude below this [184, 185]. Self-interaction of neutral gas is of the order of atomic-sized hard-ball cross-section $\sigma/m_p \sim 10^8 \mathrm{cm}^2/\mathrm{g}$. Hence despite baryons are gravitationally subdominant and generally follow the distribution of DM, due to self-interactions their distribution can differ in large density regions and on smallest scales.

The extent to which the gas deviates from DM depends on the characteristic pressure scale – the *Jeans length* $\lambda_J \sim \sqrt{\dfrac{kT}{G\rho m}}$. Below this scale the structures are washed-out by pressure. It manifestly depends on the gas temperature which can change rapidly through photoheating. However, redistribution of gas takes *dynamical time* $t_{dyn} \sim 1/\sqrt{G\rho}$ which can be larger. In this case not only the current temperature and pressure define the scale of washed-out structures, but also the whole thermal history.

Ionization state of the gas determines the opacity of the medium – i.e., the amount of absorption. There is a degeneracy between the total gas density and ionization fraction. However, as gas is expected to be in ionization-recombination equilibrium, the information about the thermal state lifts this degeneracy.

5.4.1 Pressure effects in gas

We follow [186] and consider a simplified model of two-component system of DM and baryons. The linear evolution of perturbation in the Dark Matter-baryon fluid is described by

$$\begin{array}{l} \frac{d^2\delta_X}{dt^2} + 2H\frac{d\delta_X}{dt} = 4\pi G\overline{\rho}\left(f_X\delta_X + f_b\delta_b\right) \\ \frac{d^2\delta_b}{dt^2} + 2H\frac{d\delta_b}{dt} = 4\pi G\overline{\rho}\left(f_X\delta_X + f_b\delta_b\right) - \frac{c_S^2}{a^2}k^2\delta_b \end{array}, \tag{5.4.1}$$

where δ_X and δ_b are the Fourier components of density fluctuations in the DM and baryons, f_X and f_b are the respective mass fractions, and c_s is the gas as sound speed.

Pressure term in the baryon perturbation equation suppresses the fluctuations below the characteristic pressure Jeans scale:

$$k_J = \frac{a}{c_S}\sqrt{4\pi G\overline{\rho}} \tag{5.4.2}$$

In the limit of baryon fraction f_b going to zero, this gives a filtering in baryon perturbations:

$$\delta_b(t,k) = \frac{\delta_X(t,k)}{1 + k^2/k_J^2} \tag{5.4.3}$$

5.4.2 Pressure support in expanding Universe

The distribution of matter also depends on the whole thermal history of gas temperature. At every point in time gas pressure is defined by the temperature. If the corresponding Jeans scale is larger than the size of the structure, gas expands and leaves the gravitational well.

However, while the temperature of the gas can change very fast due to radiation moving at the speed of light, the gas itself redistributes at the dynamical timescale $\sim \sqrt{\frac{1}{G\rho}}$. This means that during events like reionization gas temperature and pressure change rapidly, but the Jeans scale does not characterize the distribution of gas if the dynamical timescale is larger than the heating timescale. Vice versa, pressure at early times suppresses small structures and delays their growth until much later.

According to [186], a relevant scale for pressure suppression in the linear regime is given by

$$\frac{1}{k_F^2(a)} = \frac{3}{a}\int_0^a \frac{da'}{k_J^2\left(a'\right)}\left[1 - \left(\frac{a'}{a}\right)^{1/2}\right] \tag{5.4.4}$$

(above the matter-dominated epoch with $\Omega_m = 1$ is assumed – which is applicable to the high enough redshifts $z \gtrsim 3$)

We consider two illustrative cases for the thermal history:

1. For gas coupled to CMB at $z \gtrsim 100$ with $T \propto 1/a$ the filtering scale equals to the Jeans scale: $k_J \equiv k_F$. In case when gas temperature evolves as $T \propto 1/a^2$ (as happens between reionization and $z = 100$) $k_F < k_J$. And for rapidly heating gas like during reionization $k_F > k_J$.

2. In a case of a schematic thermal history with $T \propto 1/a$, $T \propto 1/a^2$ and reionization regimes, the filtering scale turns out to be about 4 times different from the Jeans scale at the end of reionization: $k_F \sim 4k_J$

In static conditions, pressure support creates a minimal scale for gas clouds – the *Jeans scale* λ_J that depends on the instantaneous gas temperature. However because of finite time required to redistribute the gas, the minimum cloud size in the expanding Universe with changing temperature is the *filtering scale* λ_F, defined by the whole thermal history.

5.4.3 Epoch of Reionization

Effect of the ionizing radiation in linear approximation can be described by the following system of equations [187]:

$$\frac{dT}{dt} = -2HT + \frac{2T}{3(1+\delta)}\frac{d\delta}{dt} - \frac{T}{\sum \tilde{X}_i}\frac{d\sum \tilde{X}_i}{dt} + \frac{2}{3k_B n_b}\frac{dQ}{dt} \tag{5.4.5}$$

$$\frac{d\tilde{X}_i}{dt} = -\tilde{X}_i\Gamma_i + \sum \tilde{X}_j\tilde{X}_k R_{jk}\frac{\bar{\rho}_b(1+\delta)}{m_p} \tag{5.4.6}$$

where equation on temperature accounts for expansion, adiabatic heating, redistribution of energy per particle due to changes in abundances and external heating ($\dot{Q}$). The abundance equations explicitly account for ionizations and recombinations. The quantities $\tilde{X}_i$ are defined by $n_i = \frac{(1+\delta)\bar{\rho}_b}{m_p}\tilde{X}_i$ such that e.g. $X_{HI} = \frac{\tilde{X}_{HI}}{\tilde{X}_{HI}+\tilde{X}_{HII}}$. The photoionization Γ_i and photoheating $\dot{Q}$ rates are given by:

$$\Gamma_i = \int_{\nu_i}^{\infty} 4\pi J(\nu)\sigma_i \frac{d\nu}{h\nu} \tag{5.4.7}$$

$$\frac{dQ}{dt} = \sum n_i \int_{\nu_i}^{\infty} 4\pi J(\nu)\sigma_i(h\nu - h\nu_i)\frac{d\nu}{h\nu} = n_i\epsilon_i \tag{5.4.8}$$

Γ_i has units of s^{-1}, ϵ_i is $\mathrm{erg\,s}^{-1}$ and $J(\nu)$ is $\mathrm{erg\,s^{-1}cm^{-2}sr^{-1}Hz^{-1}} = \mathrm{erg\,cm^{-2}sr^{-1}}$.

The quantity $J(\nu)$ is the mean intensity of the radiation that encompasses all information about the sources. Since the cross-sections σ_i are strongly peaked at ν_i, most of the information about the ionization and heating rates is provided by the amplitude and slope of $J(\nu)$ at ionization thresholds ν_i. Radiation intensity is computed based on the properties of the sources, but the intervening material is known to modify the spectrum of radiation as well [188].

After reionization, the gas is highly ionized by collisions with UV-background photons counteracted by recombination of electrons with the nuclei. Demanding the equilibrium of

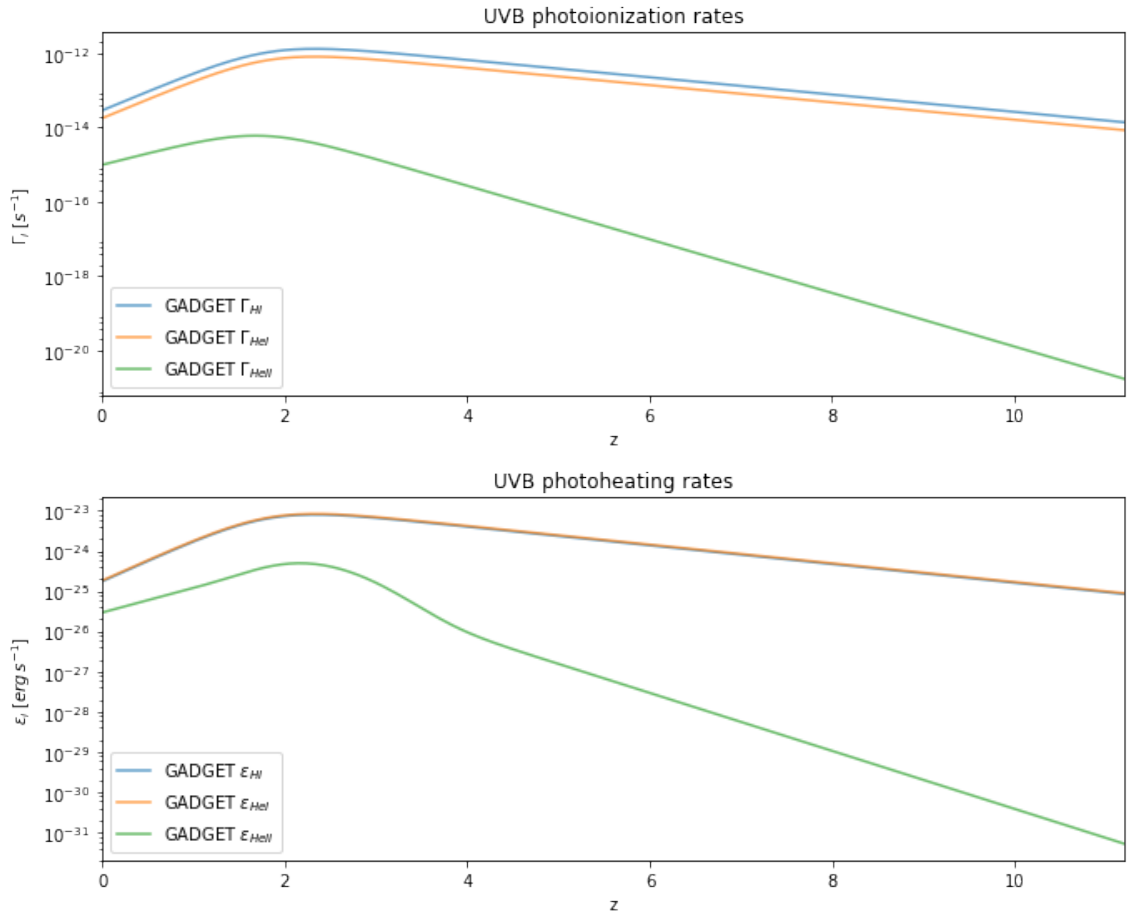

Figure 5.3: Example of an ultraviolet background created by stars typically used in simulations. *Upper panel* shows the photoionization rates for Hydrogen and Helium species, while *lower panel* shows the corresponding photoheating rates.

the system, we can write

$$n_{HI}\Gamma_{\gamma HI} = \alpha_{HII} n_e n_{HII} \tag{5.4.9}$$

In the highly ionized state $n_H \approx n_{HII}$, hence

$$\frac{n_{HI}}{n_H} \approx \frac{n_{HI}}{n_{HII}} = \frac{\alpha_{HII}}{\Gamma_{\gamma HI}} \frac{n_e n_{HII}}{n_{HII}} = \frac{\alpha_{HII}}{\Gamma_{\gamma HI}} n_e \tag{5.4.10}$$

The electron density is given by total density of baryons and non-Hydrogen mass fraction ($\approx 1 - Y$ with $Y \approx 0.24$ being the Helium mass fraction)

$$n_e = n_H + 2n_{He} = n_H \left(1 + 2\frac{Y}{1-Y}\frac{m_H}{m_H e}\right) \approx n_H \left(1 + \frac{Y/2}{1-Y}\right) = n_H \frac{1 - Y/2}{1-Y} \tag{5.4.11}$$

Then,

$$n_{HI} = \frac{\alpha_{HII}}{\Gamma_{\gamma HI}} n_H^2 \frac{1 - Y/2}{1 - Y} \tag{5.4.12}$$

We see that neutral Hydrogen density in ionization equilibrium is proportional to the square of the total Hydrogen density. Also note that $\alpha_{HII} \propto T^{-0.7}$ – so both increasing temperature and higher UVB ionization rate decrease the neutral Hydrogen fraction.

Next, according to [186], as long as the UVB is sufficient to ionize the Universe, the average temperature of the gas does not depend on the precise spectrum of photons and can be expressed as

$$n_{HI} \to 0 \;\; \Rightarrow \;\; T_0 \to \frac{\epsilon_{HI}}{3 k_B \Gamma_{\gamma HI}} \tag{5.4.13}$$

i.e., temperature is given only by the ratio of photoheating and photoionization rates.

The details of galaxies emission are thought to be crucial for the state of the IGM. In fact, the temperature of the gas is thought to result from a balance between photo-heating from the ultraviolet background generated by the galaxies and the adiabatic cooling of the Universe [187, 189]. This balance results in a tight power-law relation between gas temperature and density, the *temperature-density* (or $T - \rho$) *relation*:

$$T = T_0 \left(\frac{\rho}{\bar{\rho}} \right)^{\gamma - 1}, \tag{5.4.14}$$

where $\bar{\rho}$ denotes the mean density. In particular, the details of the hardness of the sources of reionization is crucial for the discussion of the state of the IGM at high redshift.

As gas is impulsively heated during reionisation, the heat input per hydrogen atom is mostly independent of density, driving $\gamma \to 1$. The heating rate then drops as the gas becomes ionised, but more so at low density than at high density. This steepens the temperature-density relation asymptotically to $\gamma - 1 = 1/(1 + 0.7) \sim 0.6$, with the factor 0.7 coming from the temperature dependence of the CASE-A H II recombination coefficient [189, 190]. The characteristic timescale for approaching the asymptotic value is of the order of the Hubble time. If reionisation indeed happens late, $z \sim 7.5$, then we would expect $1 < \gamma < 1.6$.

5.4.3.1 Sources of reionization

What about the mechanism of this *reionization* event? Initially neutral atoms form when the Cosmic Microwave Background decouples from the baryons – i.e., when the interaction rate between plasma and photons becomes less than the Universe expansion rate. This happens at very early times ($z \sim 1100$) when the temperature of radiation is very high ($T \sim 3000\,\mathrm{K}$). Since then, because of the expansion of the Universe, the temperature

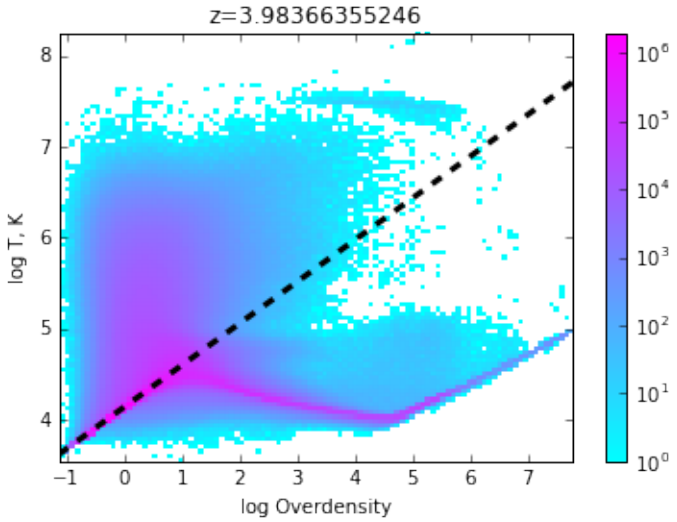

Figure 5.4: Temperature-density relation observed in simulations. Color shows the number of particles. The dashed line shows the linear fit to the range of overdensities $0.1 \ldots 1$

decreased as $\propto 1/a = (1+z)$, so at $z \ll 100$ the CMB could not possibly be the cause of the reionization.

The reionization of hydrogen and of the first level of helium happen respectively at $E \sim 13.6\,\mathrm{eV}$ and $E \sim 24.6\,\mathrm{eV}$, and they are considered consistent with stellar reionization. The reionization of the second level of Helium happens at $E \sim 54.4\,\mathrm{eV}$, hence it requires much harder sources spectra than the ones of hydrogen and first level of helium. Hence, it is believed to be driven mainly by quasars. However, poor knowledge of the halo mass function (especially at small masses and high redshifts) and quasar population makes it unclear in what proportion quasars, high- and low-mass galaxies contribute at different times.

Among other the possible sources of the ionizing radiation are evaporating black holes, various annihilating or decaying particles (see e.g. [191–193]).

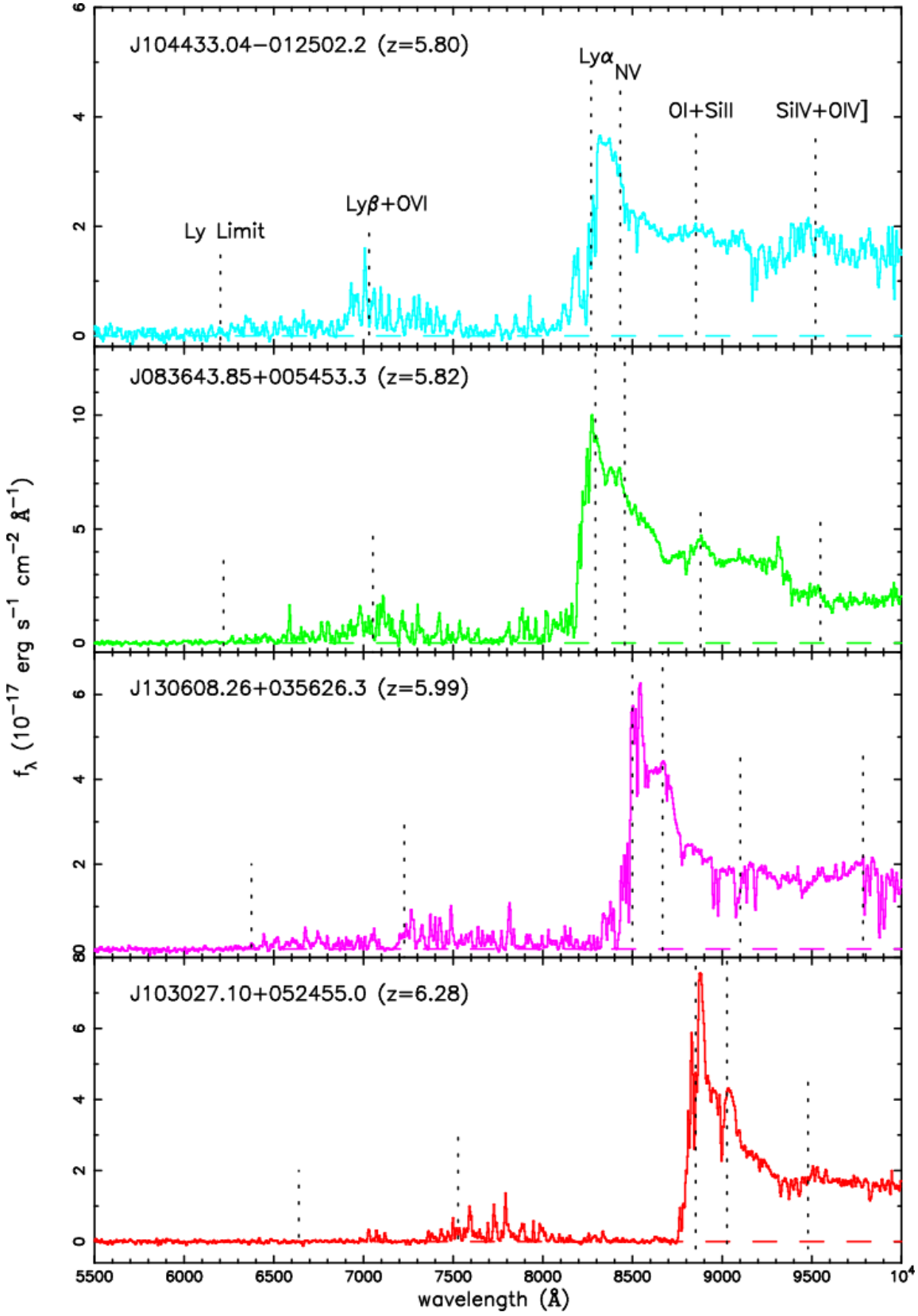

Figure 5.5: Spectra of 4 quasars located around redshift $z \sim 6$. Note how flux to the left of the Lyman-α emission peak disappears after redshift $z = 6$. *Credit: Becker et al.* [194]

5.4.3.2 Timing of reionization

After recombination the Universe becomes cold, neutral and transparent to photons. However, observations indicate that the galaxies and clusters contain mostly hot ionized gas. This discrepancy is associated with heating up of the gas falling into gravitational wells as well as photoheating and photoionization. It is plausible to assume that star formation and winds originating from galaxies are responsible for ionization of the gas.

It has been observed that the flux bluewards of the Lyman-α emission peak in quasar spectra rapidly decreases around redshift $z \sim 6$. This phenomenon can be explained by the fact that Lyman-α transition is a relatively strong one and even a small density of neutral hydrogen can completely absorb all photons. Indeed, given typical cosmological hydrogen density, a neutral fraction of $\gtrsim 10^{-4}$ is capable of creating the region of full absorption – the so-called Gunn-Peterson trough [195] (Fig. 5.5). And vice versa, for transmission, the neutral fraction should not exceed this value. Figure 5.5 shows spectra of four quasars around redshift 6.

Since this happens universally for all distant-enough quasars (albeit with some redshift variation), we can conclude that hydrogen undergoes a process of ionization at $z \gtrsim 6$ that results in appearance of the highly ionized regions and overdense (or slightly more neutral) structures that correspond to absorption features.

Moreover, at $z \lesssim 6$ the IGM is ionized up to a very high degree – fraction of neutral hydrogen is less than 10^{-4}:

$$\tau(z) \sim 6.6 \cdot 10^3 \frac{\Omega_b h}{0.02}(1+z)^{\frac{3}{2}} x_{HI}(1+\delta) \tag{5.4.15}$$

Given there is enough time to establish the photoionization equilibrium, the gas should also be hot – of the order $10^4 K$. This is corroborated by the Doppler broadening of individual absorption features.

From this we can conclude that the Universe was somehow heated up and ionized around $z \sim 6$. This event is referred to as the *Epoch of Reionization*.

5.4.4 Summary of the reionization

We observe that at the time of formation of CMB the Universe became non-ionized, while at the moment it is ionized up to a very high degree. This means that at some point reionization happened. Among the possible sources of reionization are star-forming galaxies and quasars. The Lyman-α data point that reionization has been completed by $z \sim 6$.

However, the reionization history is weakly constrained by the experimental data. In [196] the constraints on reionization were put using data from CMB and Lyman-α emission at redshifts 7-8. The results are shown in Fig. 5.6. We see that very different histories of ionization fractions are possible, including even non-monotonic ones. As we will see in Sec. 5.7, these different thermal histories may cause deviations of the Hydrogen distribution from the distribution of dark matter at very different scales.

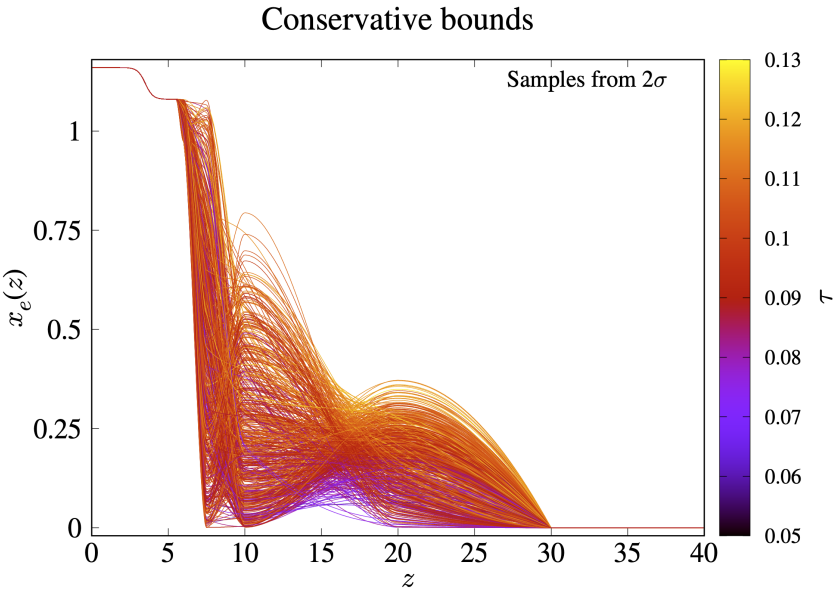

Figure 5.6: A collection of reionization histories consistent with CMB and Lyman-α emission data. Curves present individual histories of free electron fraction evolution $x_e(z)$ coloured by the corresponding optical depth to reionization τ. *Credit: Hazra et al.* [196]

We conclude that thermal effects caused by the formation of first stars and reionization of Hydrogen can prevent it from following the distribution of Dark Matter at small scales and therefore mimic the effect of free-streaming of DM particles. Our current knowledge about reionization and thermal history of intergalactic medium does not allow to predict at what scales these thermal effects will show up. This creates a major systematic uncertainty for the whole approach. Once we see a cutoff in the distribution of Hydrogen, we have to investigate its origin before interpreting the results.

5.5 How to measure Hydrogen power spectrum

Even if at the smallest scales neutral Hydrogen can be affected by thermal effects that take place during (and after) reionization (see Sec. 5.4), it can still be used to trace dark matter distribution in the Cosmic Web for a wide range of scales.

There are two main observational approaches to do this – the *21 cm line* [182] (related to the transition between hyperfinely split levels of the Hydrogen atom ground state) and the *Lyman-α absorption*. To date, the measurement of the 21cm signal is an extremely active area of research, but even the most rough density distributions obtained in this manner are still years in the future [197]. Hence here we discuss the second approach. For this we need distant sources, preferably with a featureless spectrum in the corresponding part of the spectrum. The best available candidates are quasars.

5.5.1 Quasi-Stellar Objects

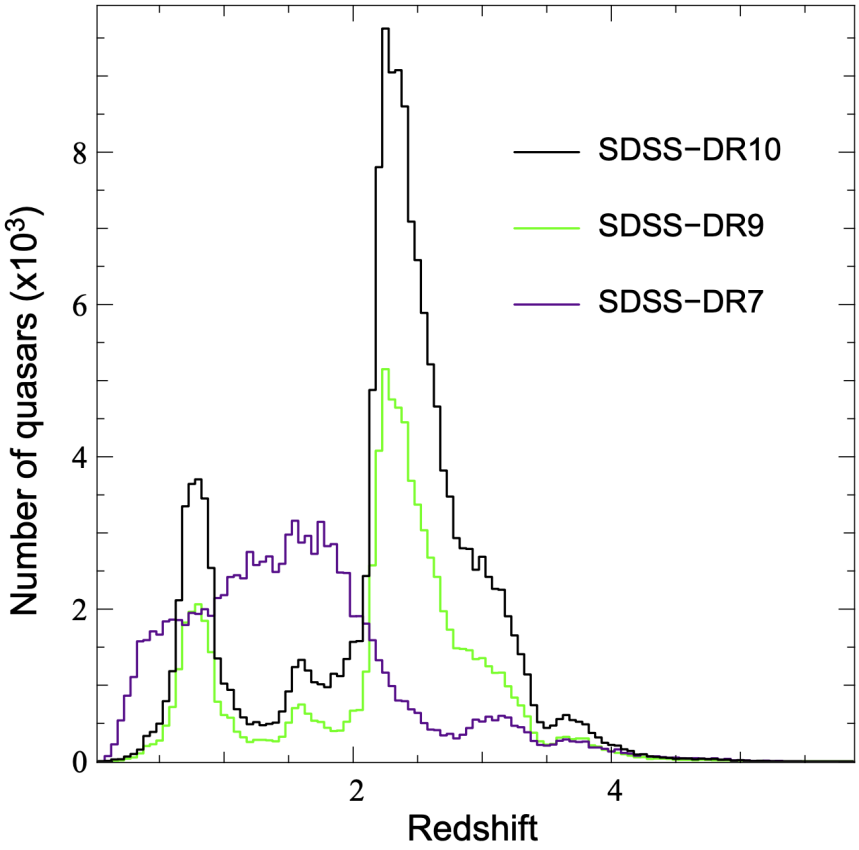

Figure 5.7: Quasar redshift distribution observed by Sloan Digital Sky Survey. *Credit: Paris et al.* [198]

Quasars are extremely bright objects found at huge range of redshifts up to $z \sim 10$, see Fig. 5.7 with quasars distribution by redshift. Most of the quasars are located around $z \sim 2.5$, but their numbers sharply fall at larger z. They emit significant radiation at wide range of wavelengths (as opposed to the stellar black-body spectrum centered around the temperature).

Quasar spectra contain numerous emission peaks corresponding to atomic transitions, see Fig. 5.8. As the light emitted travels from the quasar, it gets redshifted. If the light at the redshifted frequency is close to the one of the baryonic transitions, the photons might be absorbed by the intervening atoms, and later re-emitted in a random direction. This means that *bluewards* of each emission feature, we expect a set of absorption features, due to scattering of the light with the IGM. Moreover, as quasars emit at large range of frequencies, these sets of features can significantly overlap, making the identification difficult.

Luckily, some ranges of wavelengths with little interference were identified. They belong to Lyman series of transitions of the lightest elements – hydrogen and helium. Due to their primordial large abundances, these features are the most intense.

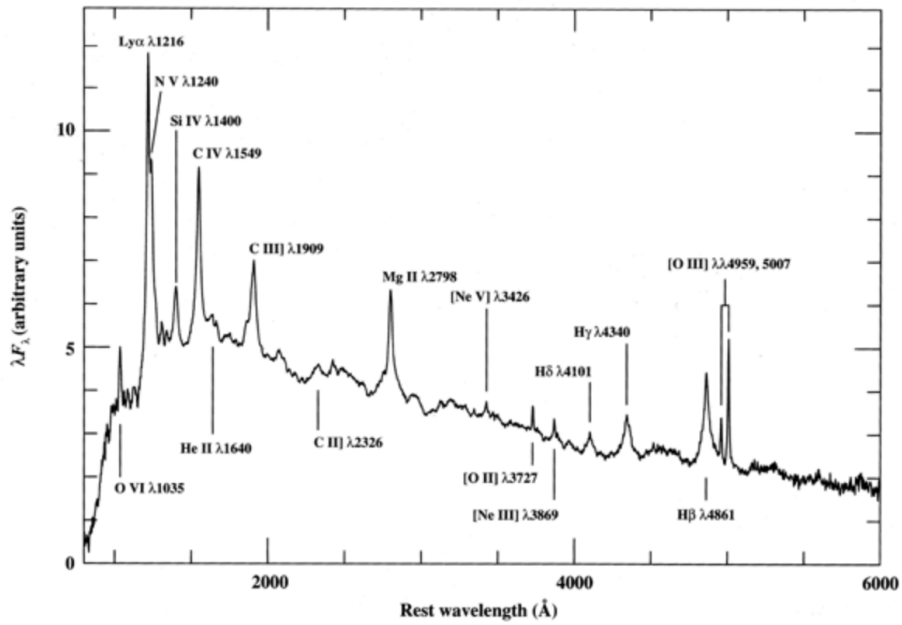

Figure 5.8: A mean QSO spectrum formed by averaging spectra of over 700 QSOs from the Large Bright Quasar Survey. Prominent emission lines are indicated. *Credit: Francis et al.* [199]

Especially interesting is the Lyman-α transition with wavelength $\lambda_\alpha = 1215.67\,\text{Å}$. It corresponds to transition between the ground level and first excited level of the electron in the atomic hydrogen. This is the most prominent peak in quasar spectra, as shown in Figure 5.9. Large numbers of absorption features at all redshifts can be identified between Lyman-α frequency and the next one in the series – Lyman-β.

We can use the section of the quasar spectrum between Lyman-α and Lyman-β emission peaks to measure the distribution of H I in the Universe.

5.5.2 Absorption features

The properties of the absorbers are defined by the matter distribution as well as the thermal state of the gas.

For an isolated cloud of gas, the resulting quasar spectrum feature is defined by:

- Size of the cloud along the line of sight (light passing along the filament will get a wide feature)
- Neutral hydrogen density (ionized clouds are transparent; recombined gas in galaxies is opaque)
- Peculiar motion of the cloud with respect to the Hubble flow (similar to an error in determination of redshift)

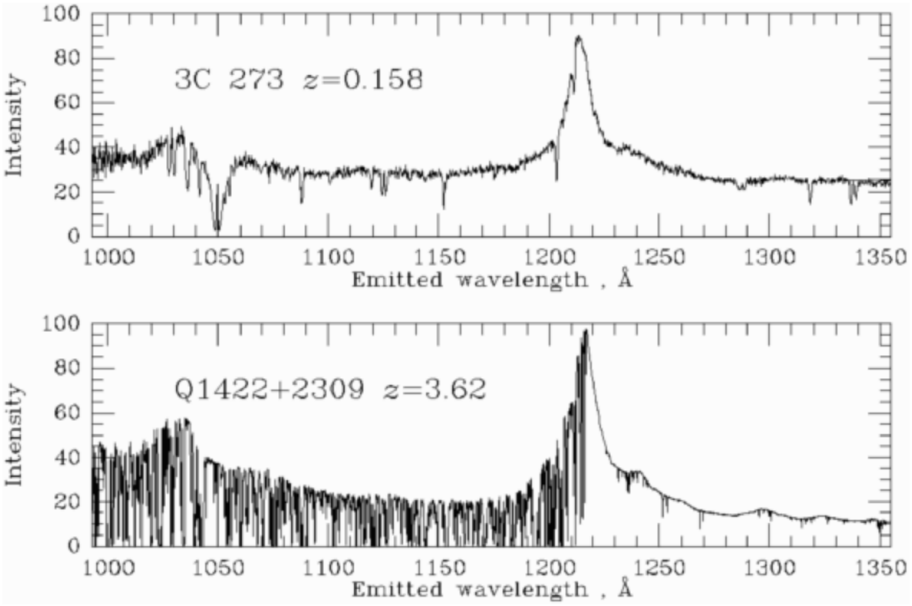

Figure 5.9: Two examples of quasar spectra in the emission wavelength. In the top panel we show the quasar spectra around of a quasar at $z = 0.158$, in the bottom panel the spectra of a quasar at $z = 3.62$. In both panels we observe the Lyman-α emission peak. In the bottom panel, bluewards of the peak, we observe a prominent Lyman-α forest, whereas in the top panel we observe more isolated absorption line. In both panel we observe on the left the Lyman-β peak. *Credit:* [www.astro.ucla.edu]

- Velocity gradient inside of the cloud (gas in non-collapsed structures retains a portion of Hubble expansion; gas in virialized halos has a narrower distribution of velocities)
- Gas temperature (motions of individual atoms)

Each absorption line has two main characteristics: its depth and width. The depth of the absorption line is defined by the column density of the neutral Hydrogen along the line of sight. The line width depends on the Doppler effect (peculiar velocities and temperature of the gas) and physical size of the structure.

5.5.3 Optical depth

Observed quasar spectra are similar to the rays of light shining through the Universe which are focused on the Earth. When we study them, we aim to abstract from the properties of the particular quasar and to measure the fractional transmission $F(\nu) \equiv N_{observed}/N_{emitted}$. Hence we are not required *per se* to model the quasars. We will be modelling the quasar spectra using the *optical depth*

$$\tau = -\ln F. \tag{5.5.1}$$

The optical depth of light at some observed wavelength λ through Lyman-α transition by the neutral hydrogen gas with density n_{HI} along some distance R is given by the integral transition cross-section σ multiplied by the column density of the gas:

$$\tau(\lambda) = \int_R^0 \sigma\left(\frac{c}{\lambda}\right) n_{HI} dR, \tag{5.5.2}$$

where Lyman-α transition cross-section is given by:

$$\sigma(\nu) = \frac{\pi e^2}{m_e c} f \phi(\nu - \nu_\alpha), \tag{5.5.3}$$

where ν_α is the Lyman-α transition frequency, ϕ is the normalized line profile and $f = 0.416$ is the oscillator strength. ϕ can be taken either as delta-function, or as a Lorentz profile $\phi(\nu - \nu_\alpha) = \frac{1}{\pi} \frac{\gamma/2}{(\nu-\nu_\alpha)^2 + (\gamma/2)^2}$

Effect of cosmological expansion. To adapt this statement to the expanding Universe, we need to establish the relation between redshift z and proper distance R:

$$dR = adr = cdt = c\frac{\dot{a}dt}{\dot{a}} = c\frac{da}{\dot{a}} = -c\frac{dz}{(1+z)H} \tag{5.5.4}$$

where $dr = \frac{cdt}{a}$ follows from the definition of the light-like interval ($-c^2dt^2 + a^2dr^2 = 0$) Additionally, absorption at some distance happens at earlier moment of time, implying additional blue-shift of the argument of σ:

$$\tau(\lambda) = \int_0^z \sigma\left(\frac{c(1+z)}{\lambda}\right) n_{HI}(z) \frac{cdz}{(1+z)H(z)} \tag{5.5.5}$$

meaning that the light was absorbed at some smaller wavelength which was stretched by the expansion of the Universe.

Effect of thermal broadening and peculiar velocities. Let's assume that the medium is characterized by some temperature $T(z)$ and include the Doppler broadening into consideration. For simplicity, we will include this effect into the transition cross-section σ.

The one-dimensional distribution of velocity for a gas with average mass m and temperature T is the following Maxwell distribution:

$$f(v_z) = \sqrt{\frac{m}{2\pi kT}} e^{-\frac{m v_z^2}{2kT}} = \frac{1}{\sqrt{\pi} b_T} e^{-\frac{v_z^2}{b_T^2}} \tag{5.5.6}$$

with $b_T = \sqrt{\frac{2kT}{m}}$ being the thermal dispersion.

Now, let's integrate the cross-section with the velocity distribution substituting the wavelength with the value from the Doppler formula:

$$\sigma_T\left(\frac{c}{\lambda}\right) = \int_{-\infty}^{\infty} \sigma\left(\frac{c}{\lambda}\gamma(1-\beta)\right) \frac{1}{\sqrt{\pi} b_T} e^{-\frac{v_z^2}{b_T^2}} dv_z \tag{5.5.7}$$

We also can include the peculiar velocities along the radial direction by shifting the exponent

$$\sigma_T\left(\frac{c}{\lambda}\right) = \int_{-\infty}^{\infty} \sigma\left(\frac{c}{\lambda}\gamma(1-\beta)\right) \frac{1}{\sqrt{\pi} b_T} e^{-\frac{(v_z-v_0)^2}{b_T^2}} dv_z \tag{5.5.8}$$

Intrinsic broadening of the line together with Doppler effect constitute the so-called Voigt profile of the Lyman-α line.

Substituting modified Lyman-αtransition cross-section (5.5.8) into Eq. (5.5.5) we can obtain the optical depth that include effects of thermal broadening and peculiar velocities:

$$\tau(\lambda) = \int_0^z \frac{cdz}{(1+z)H(z)} n_{HI}(z) \int_{-\infty}^{\infty} dv\ \sigma\left(\frac{c(1+z)}{\lambda}\sqrt{\frac{1-v/c}{1+v/c}}\right) \frac{1}{\sqrt{\pi} b_T(z)} e^{-\frac{(v-v_0)^2}{b_T(z)^2}} \tag{5.5.9}$$

5.5.4 Lyman-alpha forest in simulations

The integrand in Eq.5.5.9 is strongly peaked around $v = v_0$ and $\frac{c}{\lambda_\alpha} = \frac{c(1+z)}{\lambda}\sqrt{\frac{1-v/c}{1+v/c}}$ (where λ_α is the rest frame Lyman-α wavelength). It is convenient to use the 'Doppler' velocity instead of the redshift as the integration variable:

$$\lambda = \lambda_\alpha(1+z)(1+v/c) \tag{5.5.10}$$

This parametrization corresponds to the distance along the line of sight according to the Hubble law $\vec{v} = H\vec{r}$ under assumption of no peculiar velocities and Doppler broadening.

If we split the velocity space into bins of the size Δv, the Lyman-α optical depth in the velocity bin v_i will get contributions from species X in velocity bins v_j like so:

$$\tau(i) = \sum_X \sum_j \sigma_X \sqrt{\frac{m_X c^2}{2\pi k_B T(j)}} \rho_X(j) a \Delta v \exp\left(-\frac{m_X (v(i)-v(j))^2}{2k_B T(j)}\right) \tag{5.5.11}$$

Gas quantities associated to the velocity bins are estimated from the SPH particles

using the following definitions [200]:

$$\rho_X(i) = a^3 \sum_j \chi_X(j) W_{ij} \tag{5.5.12}$$

$$(\rho T)_X(i) = a^3 \sum_j \chi_X(j) T(j) W_{ij} \tag{5.5.13}$$

$$(\rho v)_X(i) = a^3 \sum_j \chi_X(j) (a\dot{x}(j) + \dot{a}(x(j) - x(i)) W_{ij} \tag{5.5.14}$$

where W_{ij} is the SPH kernel interpolation for locations $x(i)$ and $x(j)$ and $\chi_X(i)$ is the relative abundance of the specie X at the particle i.

The elements abundances are computed assuming the ionization-recombination equilibrium.

5.5.5 Our simulations of Intergalactic Medium

Hydrodynamical cosmological simulations usually expose the gas in the IGM to a uniform (homogeneous and isotropic) but evolving ionising background that mimics the combined emissivity of radiation from galaxies and quasars [see e.g. 201]. As a result, the mean neutral fraction is very low: $x \equiv n_{\rm H\,I}/n_{\rm H} \ll 1$. Without such an ultraviolet background (UVB), the effective optical depth would be much higher than observed [195].

Assuming that the UVB is uniform may be a good approximation long after reionisation, when fluctuations around the mean photoionisation rate, $\Gamma_{\rm H\,I}$, are small [202, 203]. However, this may no longer be the case closer to reionisation when the UVB may be much more patchy [e.g. 204, 205]. The current best-estimate for the redshift of reionisation is $z_{\rm reion} = 7.82 \pm 0.71$, with a reionisation history consistent with a relatively rapid transition from mostly neutral to mostly ionised, and suggesting the presence of regions that were reionised as late at $z \sim 6.5$ [206]. These inferences obtained from the CMB are also consistent with hints of extended parts of the IGM being significantly neutral, $x \sim 0.1 - 0.5$, in the spectra of $z \gtrapprox 7$ quasars [207, 208]. Such late reionisation, and the patchiness associated with it, make it much harder to perform realistic simulations of the IGM that yield robust constraints on $\lambda_{\rm FS}$. In fact, the impact of large fluctuations in $\Gamma_{\rm H\,I}$ is not just restricted to inducing fluctuations in x, the neutral fraction, because the UVB also heats gas.

In this work, we have considered a suite of dedicated cosmological hydrodynamical simulations, and one of the simulations from the Eagle simulation suite. Our dedicated simulation suite has been performed using the simulation code used by [214]. This code is a modified version of the publicly available GADGET-2 TREEPM/SPH code described by [45]; the runs performed are summarised in Table 5.1. The values of the cosmological parameters used are in Table 5.2; runs labelled 'Planck' use parameters taken from [213], those labelled 'Viel' use parameters taken from [150] to allow for a direct comparison with the latter work.

Name	$L\,[\mathrm{Mpc}/h]$	N	Dark Matter	UVB	Cosmology
CDM_L128N64	128	64^3	CDM	no UVB	Viel
CDM_L20N512	20	512^3			
CDM_L20N896	20	896^3			
CDM_L20N1024	20	1024^3			
M7L1	20	1024^3	$m_{SN} = 7\,\mathrm{keV}, L_6 = 1$	no UVB	Viel
M7L8			$m_{SN} = 7\,\mathrm{keV}, L_6 = 8$		
M7L12			$m_{SN} = 7\mathrm{keV}, L_6 = 12$		
CDM_Planck_Late	20	1024^3	CDM	*LateR*	Planck
CDM_Planck_Early			CDM	*EarlyR*	
M7L12_Planck_Late			$m_{SN} = 7\,\mathrm{keV}, L_6 = 12$	*LateR*	
EAGLE_REF	100 $/h$	1504^3	CDM	Eagle	Planck

Table 5.1: Hydrodynamical simulations considered in this work together with corresponding parameters. All simulations were performed specifically for this work, except `EAGLE_REF` [209]. Columns contain from left to right: simulation identifier, co-moving linear extent of the simulated volume (L), number of Dark Matter particles (N, there is an equal number of gas particles), type of Dark Matter (CDM or sterile neutrino WDM with the indicated particle mass, m_{SN} – expressed in natural units – and lepton asymmetry parameter, L_6), ultra-violet background imposed during the simulation (no UVB indicates no UVB was imposed; *LateR* and *EarlyR* refer to the UVBs from the *LateR* and *EarlyR* reionization models in [210], *Eagle* indicate the standard UVB from [211]), choice of cosmological parameters from Table 5.2, and figure where the particular simulation is used. The gravitational softening length for gas and Dark Matter is kept constant in co-moving coordinates at 1/30$^{\mathrm{th}}$ of the initial interparticle spacing. All simulations were started from the initial conditions generated by the `2LPTic` [212] with the same 'glass'like particle distribution generated by GADGET-2 [45].

Cosmology	*Planck* [213]	*Viel* [150]
Ω_0	0.308 ± 0.012	0.298
Ω_Λ	0.692 ± 0.012	0.702
$\Omega_b h^2$	0.02226 ± 0.00023	0.022393
h	0.6781 ± 0.0092	0.7
n_s	0.9677 ± 0.0060	0.957
σ_8	0.8149 ± 0.0093	0.822

Table 5.2: Cosmological parameters used in our simulations. *Planck* cosmology is the conservative choice of TT+lowP+lensing from [213] (errors represent 68% confidence intervals), while *Viel* cosmology corresponds to the bestfit model in [150].

Initial conditions for the runs were generated using the `2LPTic` code described by [212], for a starting redshift of $z = 99$ that guarantees all sampled waves are still in the linear regime. The initial linear power spectrum for the CDM cosmology was obtained with the linear Boltzmann solver CAMB [215]. Sterile neutrino Dark Matter is also modelled as

non-interacting massive particles, with the effects of free streaming imprinted in the initial transfer function as computed with the modified CAMB code described by [153], using the primordial phase-space distribution functions for sterile neutrinos computed in [158]. Using instead results from the most recent computations [216, 217] would not change our results. We neglect the effects of peculiar velocities of the WDM particles other than the cutoff they introduce in the transfer function. The linear matter power spectra for the different models used in this work are shown in Fig.5.2.

Although it is possible to carry out approximately self-consistent simulation of the IGM during reionisation (e.g. [218]), such calculations are still relatively computationally demanding. We therefore use the following strategy in this work: we perform some of the simulations *without* imposing a UVB, meaning that effectively $\lambda_p = 0$. We then apply an 'effective' UVB in post-processing, by imposing a given temperature-density relation of the form given by Eq. (5.4.14) and scaling the neutral fraction x to obtain the observed effective optical depth (as described in more detail below). We stress therefore that many of our runs are not realistic, nor are they intended to be. Quite the opposite, we work in an idealised scenario that allows us to vary individually every relevant effect separately. In addition to these runs, we also carry out simulation that do impose a UVB on the evolving IGM – we use these to demonstrate that our limits on $\lambda_{\rm FS}$ are also valid in this more realistic scenario.

For simulations that include a UVB, we specify the redshift-dependent values of the photoionisation and photoheating rates for hydrogen and helium as input parameters. The version of GADGET that we use solves for the radiative heating and cooling of the photoionised gas, given these input rates. Imposing the rates of [210] results in a $T - \rho$ relation that is consistent with that of the latter authors. We use the same UVB in the SN cosmology as an *example* of the reionisation history with a small filtering scale.

SPH (gas) particles are converted to collisionless 'star' particles when they reach an overdensity $\rho/\bar{\rho} > 1000$ provided their temperature $T < 10^5$ K. This 'quick-Lyman-α' set-up reduces run time by avoiding the formation of dense gas clumps with short dynamical times, that would in reality presumably form stars in a galaxy. We can do so, because the impact of forming galaxies on the IGM is thought to be small, particularly at high redshifts and for the low density gas regions to which our analysis is sensitive [214, 219].

5.5.5.1 Calculation of mock spectra

We compute mock spectra of the simulations using the SPECWIZARD code that is based on the method described by [189]. This involves computing a mock spectrum along a sight line through the simulation box along one of the coordinate axis.

For simulations without a UVB (`CDM_L20N1024`, `M7L12`), we first impose a temperature-density relation of the form of Eq. (5.4.14) on all gas particles. At the high redshifts that we are considering, the Lyman-α transmission is non-negligible only for sufficiently small overdensities, $\delta \lesssim 1$. We checked explicitly that the effect of cooling at the highest densities is negligible for our analysis. Therefore, one can safely apply the temperature-density rela-

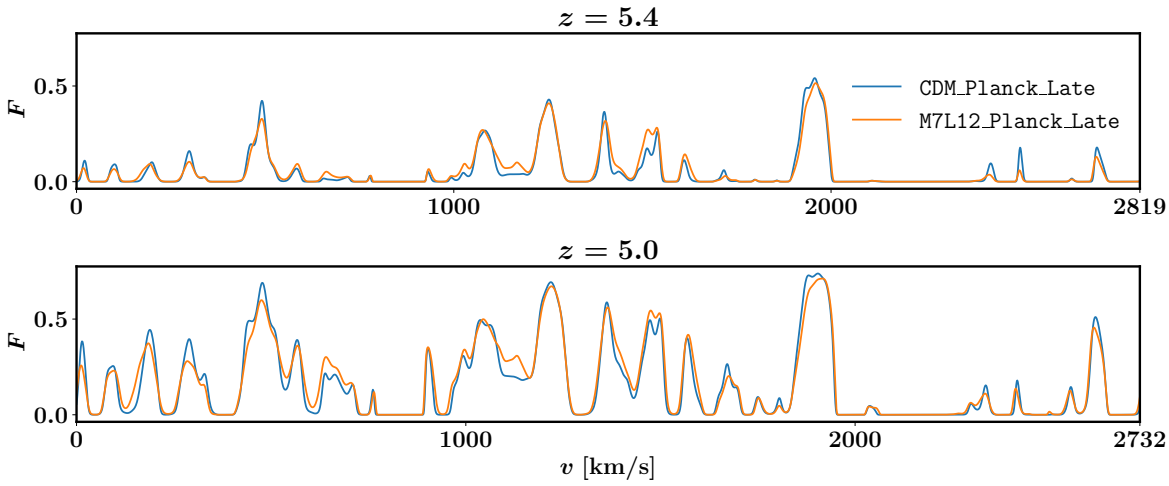

Figure 5.10: Example mock spectra extracted along the same line of sight in `CDM_Planck_Late` (blue line) and `M7L12_Planck_Late` (orange line), simulations at redshifts 5.4 (*top panel*) and 5.0 (*bottom panel*). The temperature T_0 of the gas at the mean density at these redshifts is ~ 7700K for both redshifts. Note that a sightline through the full extent of the box corresponds to a different velocity extent at different redshifts. The evolution of the mean transmission is apparent. The CDM and WDM spectra look quite similar, nevertheless on closer inspection it is clear that the CDM spectrum has some sharper features.

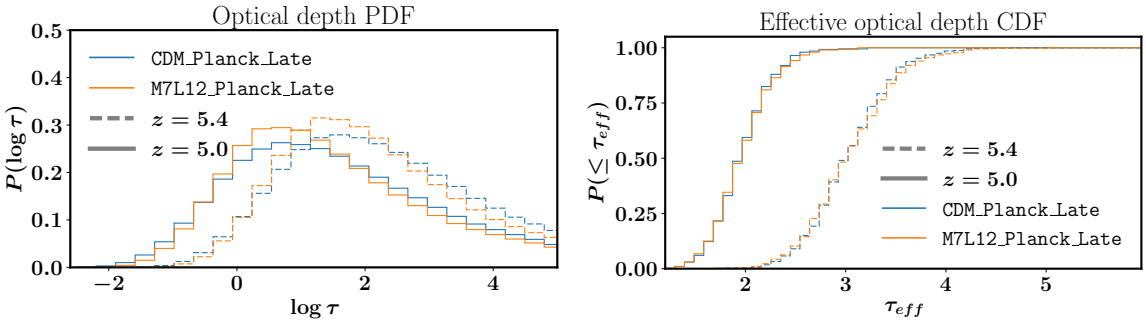

Figure 5.11: *Left panel:* probability distribution function of the optical depth per pixel. *Right panel:* cumulative probability distribution of the effective optical depth, $\tau_{\rm eff}$, measured in chunks of 50 Mpc h^{-1}. The `CDM_Planck_Late` model is plotted in *blue*, the `M7L12_Planck_Late` in *orange*, redshift $z = 5.4$ corresponds to *dashed lines* and $z = 5.0$ to *full lines*.

tion to the whole range of densities considered, without worrying about it being applicable only in the range $\delta \lesssim 10$ [187].

We use the same post-processing also for simulations which do include a UVB. The rationale behind this is the following. As already mentioned, we use [210] ionisation history only as an example of the model with small pressure effects, not as a holistic model. We then vary the T_0 in post-processing and determine the range of admissible temperatures in

CDM and WDM cosmologies. We verify *a posteriori* that the actual temperature predicted by the *LateR* model lies within the range of admissible temperatures.

Given T and ρ of each particle, we compute the neutral fraction x using the interpolation tables from [220], which assume photoionisation equilibrium,

$$\frac{dn_{\mathrm{H\,1}}}{dt} = -\Gamma_{\mathrm{H\,1}} n_{\mathrm{H\,1}} - \Gamma_c \, n_e \, n_{\mathrm{H\,1}} + \alpha(T) \, n_e \, n_{\mathrm{H\,II}} = 0 \, . \tag{5.5.15}$$

Here the terms from left to right are photoionisation by the imposed UVB, collisional ionisation, and recombination (with $\alpha(T)$ the temperature-dependent case-A recombination coefficient); n_e is the electron density; the photoionisation rate is that described by [211].

We then interpolate the temperature, density, and peculiar velocity to the sight line in bins of $\Delta v = 1$ km s^{-1} using the Gaussian method described by [221]. We verified that this spectral resolution is high enough to give converged results. We then compute the optical depth as function of wavelength, $\tau(v)$, thus accounting for Doppler broadening and the effects of peculiar velocities.

To allow for a fair comparison to the observed spectra, we convolve the mock spectra with a Gaussian to mimic the effect of the line-spread function, and rebin to the observed pixel size with parameters as described in Section 5.6.2. The Gaussian white noise has a uniform relative Standard Deviation of $\sigma = 0.066$, corresponding to a signal to noise ratio of $S/N = 15$ per pixel at the continuum level, following [150]. Further details on the application of noise to mock spectra and comparison with previous work are given in Appendix 5.C. We calculate a set of such spectra for the snapshot at redshifts $z = 5$, and $z = 5.4$.

After repeating this procedure for $\mathcal{N} = 10^3$ sight lines, we compute the mean transmission, $\langle F \rangle = \langle \exp(-\tau) \rangle$ and scale the optical depth so that the ensemble of mock spectra reproduces the observed value of $\langle F \rangle$ discussed in Section 5.6.2.

We compare spectra along the same sight line for the CDM and the `M7L12_Planck_Late` models in Fig. 5.10 (blue and orange curves, respectively), at redshifts $z = 5.4$ (top panel), and $z = 5.0$ (bottom panel); the temperature and thermal history are the same for both models. The Lyman-α spectra look very similar in these models, although it can be seen that the CDM model has some sharper features. The probability distribution function (PDF) of the optical depth is compared between these two models in Fig. 5.11. It is unlikely that we will be able to distinguish the CDM and WDM using the information in individual spectra.

Ideally, we would like to measure a quasar spectrum and use it to reconstruct the Hydrogen density along the line of sight. However in reality beside the finite instrument resolution, the broadening of the absorption lines caused by thermal effects is typically larger than the distance between the lines.

This means that we cannot use the individual absorption features to study the small-scale statistics of the matter distribution. Instead, we will use statistical methods to characterise the properties of the Lyman-α forest from many absorbers and lines of sight.

5.6 Comparison of simulations and observations

Using quasar spectra as a proxy to Dark Matter distribution, our goal is to reconstruct the Matter Power Spectrum.

Having a sufficiently dense distribution of quasars on the sky, it would in principle be possible to estimate the 3D distribution of gas by interpolating between the sightlines in the transverse direction. Then we could compute the corresponding 2-point correlation function – the Matter Power Spectrum.

Unfortunately, quasars are not numerous enough for this exercise (however, correlation between close quasar pairs provides an important test for the structure sizes since the transverse correlations are independent of the thermal Doppler effect and peculiar velocities).

5.6.1 Flux power spectrum

As outlined above, in the present work we compare the mock FPS computed from simulations to the observed FPS presented by [150]. Traditionally the FPS is computed in 'velocity space'. Integrating the Doppler shift relation between wavelength and velocity, $dv/c = d\lambda/\lambda$, the redshift or wavelength along a line-of sight to a quasar can be written in terms of a 'Hubble' velocity v as

$$v = c\ \ln\left(\frac{\lambda}{\lambda_0(1+z)}\right) = \frac{H(z)}{1+z}y\,, \tag{5.6.1}$$

where $\lambda_0 = 1215.67\,\text{Å}$ is the laboratory wavelength of the Lyman-α transition, and z is a constant reference redshift. The zero-point of v is defined by z and is arbitrary. In data, z is often chosen to be the mean redshift of the data or the quasar's emission redshift, in simulations we take it to be the redshift of the snapshot. In this equation, $H(z)$ is the Hubble constant at redshift z, and the right-hand side also defines a co-moving position y along the spectrum.

The input to the FPS (either observed or obtained from simulations) is then flux as function of velocity, *i.e.* $F(v)$, over some velocity interval V (in the data set this interval is chosen so that one avoids the Lyman-β forest, the quasar near zone, and potentially some strong absorbers; in the simulations it is set by the linear extent of the simulated volume).

Given F and its mean, $\langle F \rangle$, we calculate the 'normalised flux'

$$\delta_F \equiv \frac{F - \langle F \rangle}{\langle F \rangle} \,. \tag{5.6.2}$$

The FPS is written in terms of the dimensionless variance $\Delta^2_F(k)$ (strictly speaking a variance in δ_F per dex in k), defined by

$$\Delta^2_F(k) = \frac{1}{\pi} k P_F(k) \tag{5.6.3}$$

$$P_F(k) = V \left\langle |\tilde{\delta}_F(k)|^2 \right\rangle \tag{5.6.4}$$

$$\tilde{\delta}_F(k) = \frac{1}{V} \int_0^V dv \, e^{-ikv} \delta_F(v) \,. \tag{5.6.5}$$

Here, $\langle \cdot \rangle$ denotes the ensemble average, and $k = 2\pi/v$ is the Fourier 'frequency' corresponding to v and has dimensions of (s/km). To find the conversion to a wave-vector in inverse comoving Mpc, k_x, recall that the Hubble law of Eq. (5.6.1) states that $\Delta v = H(z)\Delta y/(1+z)$. Then, since $k_y \, y = k_v \, v$, where $k_v \equiv k$, we find that

$$k_y = k_v \frac{H(z)}{1+z} \,. \tag{5.6.6}$$

Individual quasar spectra provide only 1D information, similar to the Matter Power Spectrum projected along the line of sight:

$$\Delta^2_{1d}(q) = \frac{q}{2\pi} \int d^2 k_\perp \frac{\Delta^2_{3d}(q, k_\perp)}{(q^2 + k_\perp^2)^{3/2}} = q \int_q^\infty \frac{dk}{k^2} \Delta^2_{3d}(k) \tag{5.6.7}$$

with Δ^2_{3d} being the 3D Matter Power Spectrum.

Residual neutral hydrogen gas in the intergalactic medium (IGM) produces a series of absorption lines in the spectrum of a background source such as a quasar, through scattering in the $n = 1 \to 2$ Lyman-α transition (see *e.g.* the review by [222]). The set of lines for which the column density of the intervening absorber is low, $N_{\rm H\,1} \leq 10^{16} {\rm cm}^{-2}$, is called the Lyman-$\alpha$ forest. The transmission F, i.e. the fraction of light of the background source that is absorbed, is often written in terms of the optical depth τ, as $F = \exp(-\tau)$; we will refer to this quantity that is independent of the quasar spectrum and only depends on the intervening distribution of neutral gas, as the flux[3]. The observed power spectrum of F exhibits a cutoff on scales below $\lambda_F \approx 30 \, {\rm km \, s^{-1}}$ at high redshift, and currently

[3]Let $\mathcal{F}$ be the observed quasar flux, and $\mathcal{C}$ what would be the observed flux in the absence of absorption, then $F \equiv \mathcal{F}/\mathcal{C}$ is the transmission. This quantity is commonly but somewhat inaccurately referred to as the 'flux', we will do so as well. Since $\mathcal{C}$ is not directly observable, neither is F. Estimating F from $\mathcal{F}$ is called 'continuum fitting'.

provides the most stringent constraints on $\lambda_{\rm FS}$ [133, 148, 150, 223–225]. The reason that the Lyman-α forest provides such tight constraints on $\lambda_{\rm FS}$ is that the neutral gas follows the underlying Dark Matter relatively well, because the absorption occurs in regions close to the cosmological mean density, particularly at higher redshifts $z \geq 5$. Nevertheless there are complicating factors, which include:

(*i*) the density is probed along a single sightline; the measured one dimensional (1D) power spectrum is an integral of the 3D underlying matter power spectrum (as discussed in details in Appendix 5.7.1.1);

(*ii*) the flux is related to the density by a non-linear transformation [226];

(*iii*) absorption lines are Doppler broadened;

(*iv*) the gas distribution is smoothed compared to the Dark Matter due to its thermal pressure [227].

As a consequence, $\lambda_{\rm DM} \neq \lambda_F$, and numerical simulations that try to account for all these effects are used to infer $\lambda_{\rm FS}$ by calculating mock absorption spectra, and comparing λ_F from the simulations to the observed value. However, the temperature of the gas, and hence the level of Doppler broadening, λ_b, that needs to be applied, is not accurately known (see *e.g.* [228, 229]), especially at higher redshifts, $z \gtrapprox 5$, where the density field is more linear which makes it easier to simulate the IGM more accurately. The smoothing due to gas pressure [230] can be described in linear theory [227] and the smoothing scale, λ_p, depends on the thermal *history* of the gas; that history is not well constrained.

5.6.2 Experimental detection

The study of the FPS has been applied for many years to distinct releases of data from SDSS (BOSS). This dataset contains a few thousands quasar spectra: this allows to reconstruct the FPS very well (Fig. 5.12). However, spectral resolution is limited and the smallest scales resolved are $\Delta v \sim 50 {\rm km/s}$. The accurate measurement of the FPS was used to constrain WDM in [233].

In this work we compare our simulation results to the same flux power spectrum (FPS) computed from a set of $z \gtrsim 4.5$ quasar spectra previously analysed by [150, 234–236], and [237] (Fig. 5.13). These data are based on 25 high-resolution quasar spectra with emission redshifts in the range $4.48 \leq z_{\rm QSO} \leq 6.42$ obtained with the HIRES spectrograph on KECK, and the Magellan Inamory Kyocera Echelle (MIKE) spectrograph on the Magellan Clay telescope. We do not analyse the original spectra – they are not yet publicly available – but simply compare to the published FPS. We note that for $z = 5.0$ MIKE dataset contains 4 QSOs with the emission redshifts $z > 4.8$ [238, 239], while the HIRES dataset consists of 16 QSOs [238–240]. At this redshift the interval $\Delta z = 0.4$ used for binning in [150] corresponds to $\sim 140\,{\rm Mpc}/h$. Taking into account quasar proximity zones these quasar spectra cover $\sim 240\,{\rm Mpc}/h$ (MIKE) and $1230\,{\rm Mpc}/h$ (HIRES) at $z = 5$ and $\sim 810\,{\rm Mpc}/h$

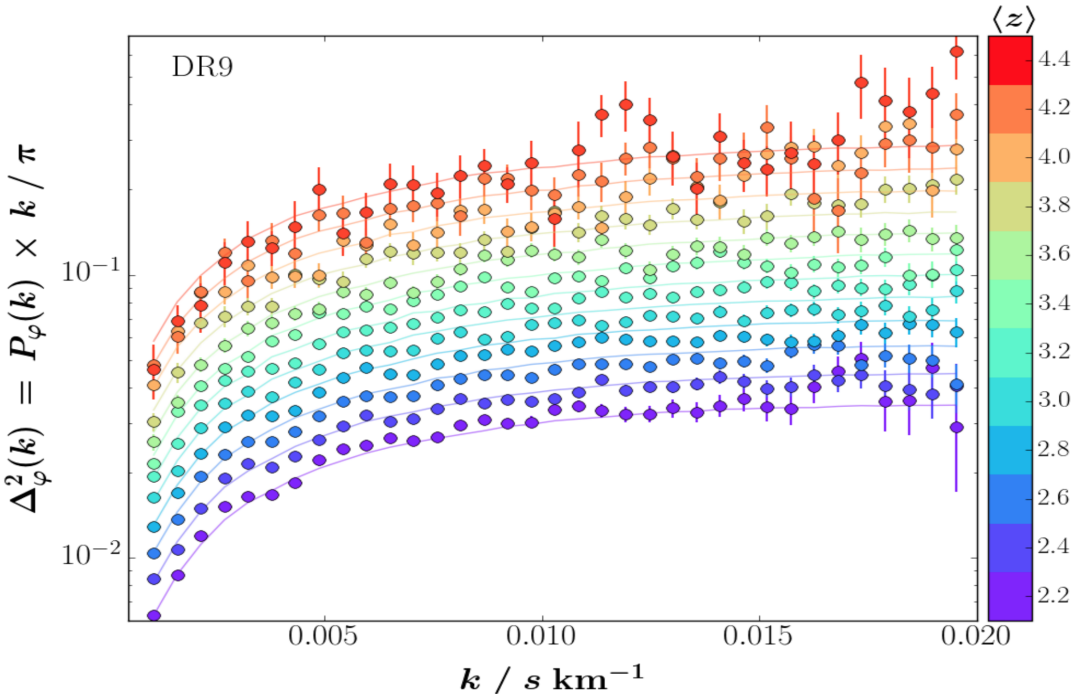

Figure 5.12: FPS measured by SDSS BOSS DR9 [231]. *Credit: Baur et al. [232]*

for HIRES at $z = 5.4$. From this we can already anticipate that the sample variance errors will be quite large for both datasets. We will use this information in Section 5.4 below when estimating errors due to this finite sampling.

The HIRES and MIKE spectra have a spectral resolution of 6.7 and 13.7 $\mathrm{km\ s^{-1}}$ full width at half maximum (FWHM), and pixel size of 2.1 and $5.0\,\mathrm{km\ s^{-1}}$, respectively. The median signal-to-noise ratios at the continuum level are in the range 10–20 per pixel [150]. We generate mock FPS with similar properties, as described below. The finite spectral resolution introduces another cutoff scale in the FPS, $\lambda_s \sim \mathrm{FWHM}$.

The ionisation level of the IGM is quantified by the *effective optical depth*, $\tau_{\rm eff} \equiv -\ln\langle F\rangle$, where $\langle F\rangle$ is the observed mean transmission, averaged over all line-of-sights. [150] report values of $\tau_{\rm eff}(z = 5.0) = 1.924$ and $\tau_{\rm eff}(z = 5.4) = 2.64$, without quoting associated uncertainties which can be quite large, stemming from the systematic errors in continuum fitting and statistical errors due to sample variance. We provide our own estimates of the statistical errors due to sample variance on $\langle F\rangle$ in Appendix 5.D. For details on the properties of the dataset, the associated noise level, and the way the FPS and its covariance matrix were estimated, we refer the reader to [150].

In our analysis we also use a more recent data on FPS measured by upgraded HIRES with only three redshift bins, see Fig. 5.14. For a description of this dataset see [151].

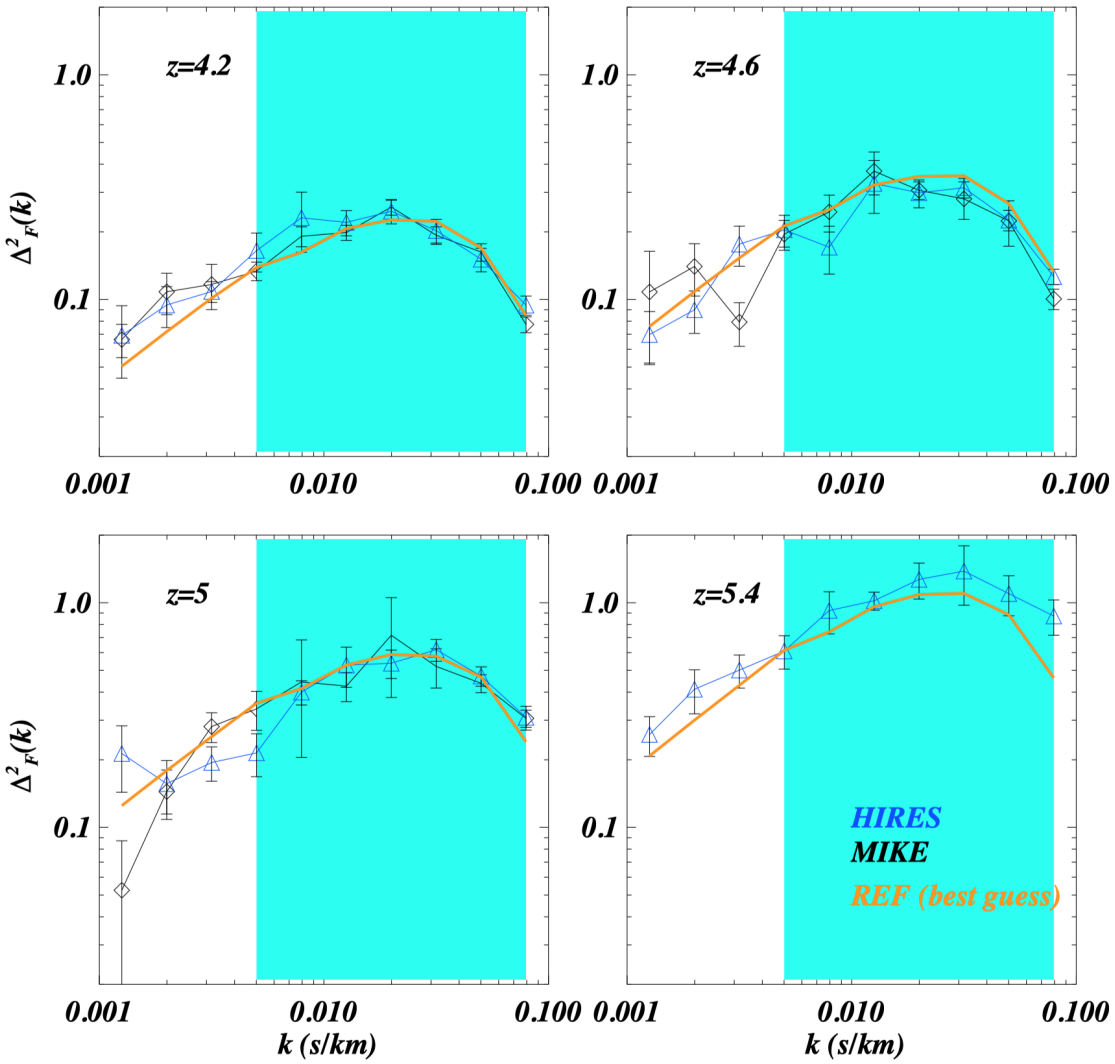

Figure 5.13: FPS measurements by Viel et al. [150]. Triangles and squares represent the actual data from MIKE and HIRES experiments, while the lines are models discussed in the paper. The highlighted regions show the range of wavenumbers used in analysis (large scale points are subject to continuum fitting systematic errors).

Using the high-resolution data we observe a cutoff in the FPS. We will discuss the possible interpretation and bounds on the WDM from it in the next section.

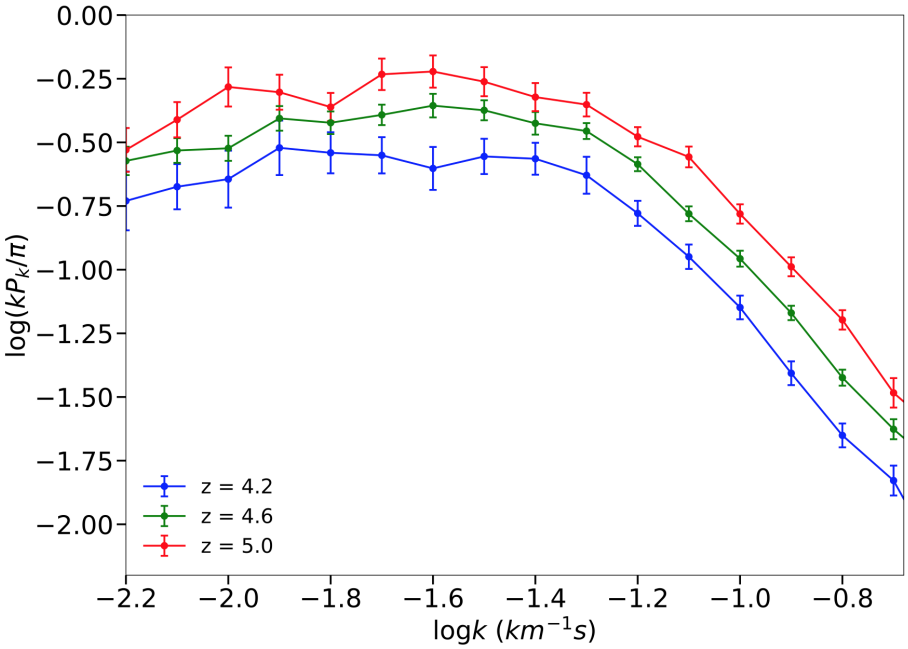

Figure 5.14: The most recent and high-resolution measurements of FPS by Boera et al. [151]

5.7 Interpretation and constraints

Before the availability of high-resolution quasar spectra, the constraints on WDM were put by constraining the deviations of the predicted flux power spectrum from the experimental data (e.g. SDSS BOSS on Fig. 5.12). The FPS in BOSS data grew with the wavenumber being consistent with CDM.

> Constraints derived from the low-resolution SDSS BOSS data put a limit for thermal WDM relic at $m \gtrsim 3.5\,\mathrm{keV}$ [241].

The high-resolution quasar spectra uncover a clear cutoff at the scales $\lambda \lesssim 30\,\mathrm{km/s}$ (Fig. 5.14). It could be generated by the thermal effects alone – e.g. indicating the temperature of the IGM at the level $T \gtrsim 10000\,\mathrm{K}$. These values are compatible with the typically considered thermal histories.

Does this mean that the cutoff is primarily due to thermal effects? As we saw before (Section 5.5.2) this kind of feature can be generated by thermal effects (even in CDM) or by the free-streaming of Dark Matter.

5.7.1 At what scale do we expect a cutoff in Cold Dark Matter?

5.7.1.1 Effect of peculiar velocities on Flux Power Spectrum

In CDM cosmologies the real-space MPS, $\Delta^2_{r,3d}(k)$, is a monotonically increasing function of k. However, in *velocity space* over which the FPS observable is built, an additional

effect – the *redshift space distortions* (RSD) – affect the shape [242–245]. RSD may erase small-scale power in the FPS because peculiar velocities of baryons are non-zero.

At linear level MPS in velocity space is related to real space by:

$$\Delta^2_{s,3d}(k) = \Delta^2_{r,3d}(k)(1 + \beta(\vec{k} \cdot \hat{z})^2)^2 \tag{5.7.1}$$

where $\hat{z}$ is the direction of observation and constant β for linear scales is given by expression $\delta_r = -\beta^{-1}\vec{\nabla} \cdot \vec{v}$ [242].

Real-space MPS projected along the line of sight is given by:

$$\Delta^2_{r,1d}(q) = \frac{q}{2\pi} \int d^2k_\perp \frac{\Delta^2_{r,3d}(q, k_\perp)}{(q^2 + k_\perp^2)^{3/2}} \tag{5.7.2}$$

$$= q \int_q^\infty \frac{dk}{k^2} \Delta^2_{r,3d}(k) \tag{5.7.3}$$

Clearly, in CDM linear $\Delta^2_{r,1d}(k)$ remains a monotonic function of k. Non-linear MPS experiences additional growth at small scales, therefore $\Delta^2_{r,1d}(k)$ does not exhibit a cutoff also at non-linear level.

Beyond the linear regime it is not possible to compute analytically the effect of RSD on the MPS. [246] have attempted to address this case, by considering a fitting formula calibrated to N-body simulations by [247]:

$$\Delta^2_{s,1d}(q) = q \int_q^\infty dk \frac{\Delta^2_{r,NL}(k)}{k^2} \left[1 + \beta \left(\frac{q}{k}\right)^2\right]^2 D\left[q\sigma_{12}(k)\right] \tag{5.7.4}$$

$$D\left[x\right] = \left[1 + \frac{1}{2}x^2 + \eta x^4\right]^{-1} \tag{5.7.5}$$

where $\sigma_{12}(k)$ is a pairwise velocity dispersion of dark matter particles, $\Delta^2_{s,NL}$ is a nonlinear $3d$ MPS and η is a constant. [246] predicted a cutoff on the scales similar to the cutoff observed in the HIRES and MIKE data.

In order to verify the predictions of [246], we have performed simulations where thermal effects were switched off, (Figure 5.15). Obviously, the simulation results for *e.g.* the IGM temperature are unrealistic in this case. The purpose of this exercise was to identify the position of a RSD-induced cutoff, which might have been obscured by thermal broadening. We find that the resolution of simulations by [247] stays significantly below the required resolution of our convergence analysis: number of particles $N = 128^3$ and box-size $L = 100\,\mathrm{Mpc}/h$ [247] against $N = 1024^3,\ L = 20\,\mathrm{Mpc}/h$. We conclude that the relevant scales have not been resolved in past simulations. To support this claim, we compare the FPS for various resolutions in model cosmologies designed to remove baryonic effects as much as possible, see Figure 5.15. Since our high-resolution simulations exhibit a cutoff at a position k's that is significantly larger than the reach of the data, we conclude

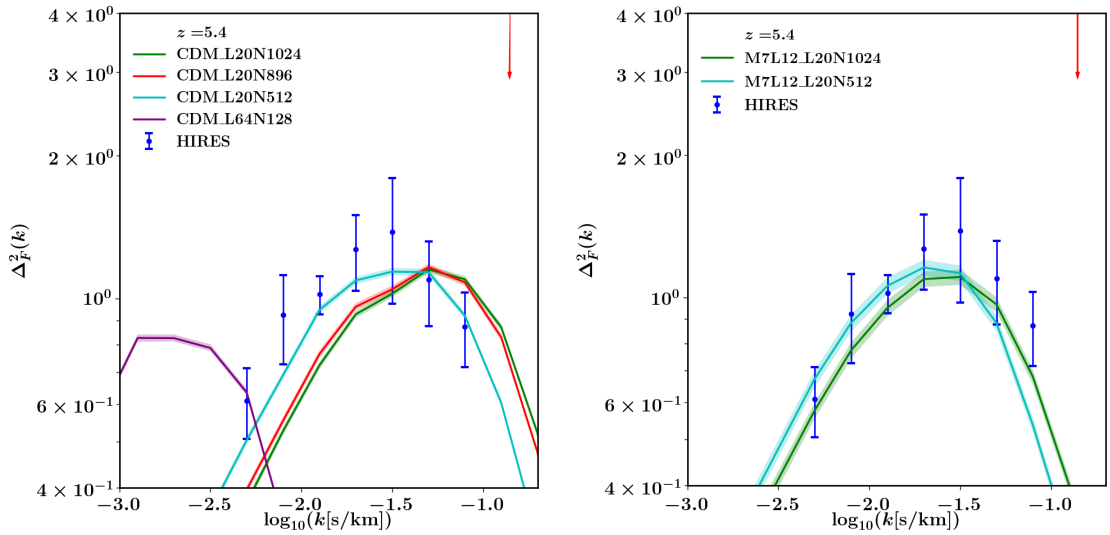

Figure 5.15: Effect of numerical resolution on the mock FPS for CDM (*left panel*) and WDM (*right panel*) of simulations performed without an imposed UVB. Both models are for the imposed power-law $T - \rho$ relation of Eq. (5.4.14) with $(T_0, \gamma) = (25\ \mathrm{K}, 1)$, are scaled to the observed value of the effective optical depth, $\tau_{\rm eff} = 3.0$ for $z = 5.4$, and mimic the spectral resolution and pixel size of the HIRES spectrograph on the KECK telescope (FWHM=6.7 km s^{-1}, pixel size=2.1 km sec^{-1} (see Section 5.6.2) but without adding noise. The data points show the error bars as reported by [150] that do not take into account sample variance (see below). The different colours correspond to different numbers of particles N, as per the legend. The observed FPS from [150] (blue) is plotted to indicate the range of relevant wave numbers. There is a numerical resolution-dependent cutoff in each simulation. Increasing the number of particles, the position of this cutoff shifts to larger k values. In our highest resolution simulations, $N = 1024^3$ DM and gas particles (green line), the resolution-dependent cutoff is outside the range of scales probed by the Lyman-α data, the corresponding Nyquist scale $k_{\rm max,sim}$ is outside the boundary of the plot. Therefore, we use such resolution in all subsequent simulations. The red arrow shows the scale associated with $k_{\rm max,DM}$. The figure also demonstrates that the simulations considered by [247] (*purple line*) lacked the necessary resolution to be used in [246].

that the role of RSD in the formation of the cutoff is negligible.

> Although the redshift space distortions produce a cutoff in FPS, the corresponding scale is $\lambda_z \ll 1\,\mathrm{km/s}$. This effect cannot be responsible for the cutoff in the data.

5.7.1.2 Cutoff due to thermal effects

The temperature T of a photoionised IGM depends on the density and on the spectral shape of the ionising radiation [248, 249]. Unlike the more familiar case of galactic H II regions, T is not set by a balance between photoheating and radiative cooling, but by the

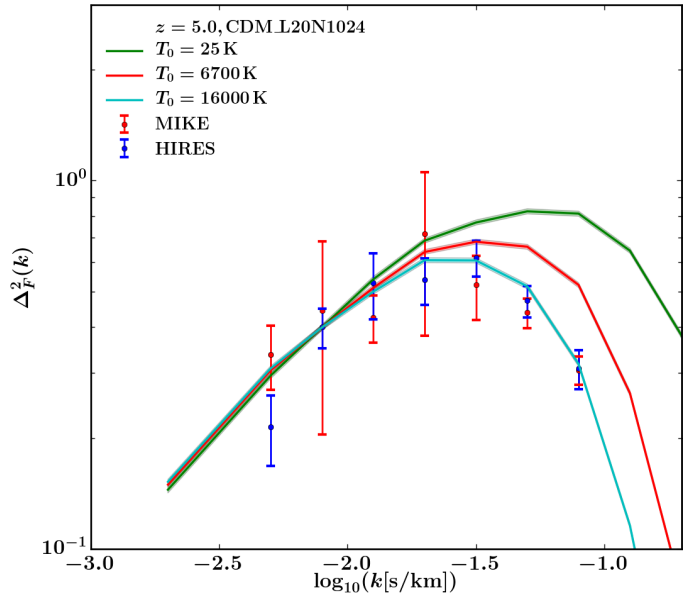

Figure 5.16: The cutoff in the mock flux power spectrum compared to the HIRES and MIKE data. We show a CDM model with three imposed temperature-density relations for $T_0 = 25\,\mathrm{K}, 6700\,\mathrm{K}$ and $16000\,\mathrm{K}$.

mostly impulsive heating during reionisation and the adiabatic expansion of the Universe. Nevertheless, the temperature T_0 in the temperature-density relation of Eq. (5.4.14) is expected to be of the order $T_0 \sim 10^4$ K with $\gamma \approx 1$ close to reionisation. Once heated, pressure will smooth the gas distribution relative to the underlying Dark Matter introducing the filtering scale λ_p discussed previously, below which the amplitude of the density power spectrum is strongly suppressed. The patchiness of reionisation will therefore introduce large-scale fluctuations in the neutral fraction x, but also in the value of λ_p, as well as in that of the Doppler-broadening λ_b.

Doppler broadening cutoff. To describe the cutoff using the thermal Doppler broadening alone (Section 5.5.3) , we need the temperature to be $T \gtrsim 16000\,\mathrm{K}$ (Fig. 5.16). While this temperature is not improbable, we don't have evidence for it at the moment.

On the other hand, how low the IGM temperature could be? When neutral gas is overrun with an ionisation front during reionisation, the difference between the energy of the ionising photon and the binding energy of H I, $\Delta E = h\nu - 13.6\,\mathrm{eV}$, heats the gas. In the case of H II regions, gas will also cool through line excitation and collisional cooling, resulting in a temperature immediately following reionisation of $T_{0,\mathrm{reion}} \leqslant 1.5 \times 10^4$ K [248, 250]. In the case of reionisation, the low density of the IGM suppresses such in-front cooling, and the numerical calculations of [251] suggest $T_{0,\mathrm{reion}} = 1 - 4 \times 10^4$ K, depending on the spectral slope of the ionising radiation. Following reionisation, the IGM cools adiabatically while being photoheated, preserving some memory of its reionisation history [219, 252]. Therefore the value of T_0 at $z = 5.4$ is set by $T_{0,\mathrm{reion}}$, the redshift

$z_{\rm reion}$ when reionisation happened, and the shape of the ionising radiation that photoheats the gas subsequently. For T_0 to be sufficiently low then requires that $T_{0,\rm reion}$ is low, that $z_{\rm reion} \gg 5.4$, and that the ionising radiation is sufficiently soft.

Taking $z_{\rm reion} = 7.82$ from [100] and $T_{0,\rm reion} = 1.5 \times 10^4$ K yields a guesstimate for the lower limit of $T_0 \sim 0.8 \times 10^4$ K at $z = 5.4$, consistent with the value of $T_0 \sim 10^4$ K suggested by [253] that we used in the previous section. There is now good evidence that He II reionised at $z \sim 3.5$, much later than H I and He I [254–257], as the ionising background hardens due the increased contribution from quasars. This suggests that the ionising background during reionisation was unable to ionise He II significantly and hence was relatively soft. So conditions for low T_0 seem mostly satisfied.

Observationally, the IGM temperature is constrained to be at the level $T_0 \gtrsim 8000$ K at $z \lesssim 4.6$ [238, 255, 258, 259] (see e.g. [190] for a recent discussion). At $z \approx 6.0$ there is a single measurement in the near zone of a quasar that yields $5000 < T_0 < 10000$ K (68% CL, [260]). Fundamentally, all of the techniques used to infer T_0 observationally are based on identifying and computing the statistics of sharp features in Lyman-α forest spectra, and comparing these to simulated spectra. This implies that the T_0 inferred implicitly depends on $\lambda_{\rm DM}$.

Combining the theoretical prejudice and the measurements, we conclude that a value of $T_0 \sim 8000$ K or even colder at redshifts around $z = 5$ is not unreasonable and definitely not ruled out. Using Eq. (5.7.6), such a value of T_0 yields $k_{{\rm max},b} = 0.12\,{\rm s/km}$. The maximum temperature still consistent with the cutoff is $T_0 = 16000\,{\rm K}$ that yields $k_{{\rm min},b} = 0.09\,{\rm s/km}$.

Pressure support cutoff. What do we know about pressure effects (Section 5.4.1) and the filtering length λ_p?

Using the analytical model by [186] for the evolution of the filtering length, we can attempt to bracket the pressure effects as well. In general, for the gas cooling in the expanding Universe $\lambda_F > \lambda_J$ and for rapid heating $\lambda_F < \lambda_J$.

Hence the absolute minimal pressure scale can be computed assuming infinitely fast reionization ($\lambda_p \sim 0.2\lambda_J$) and the maximum is given by the system with no reionization ($T \propto 1/a^2, \lambda_p \sim 2\lambda_J$).

Inhomogeneous reionization. The plausible patchiness of reionisation introduces complications. For example the large-scale amplitude of the FPS may be more a measure of the scale and amplitude of temperature fluctuations or of fluctuations in the mean neutral fraction, rather than being solely due to density fluctuations that we simulate. If that were the case, then our simulations should not match the measured FPS on large-scales, since

we have not included these effects (see e.g. [261]). Furthermore, what is the meaning of λ_b or λ_p in such a scenario, where these quantities are likely to vary spatially? Matching the cutoff in the FPS might pick-out in particular those regions where both λ_b and λ_p are unusually small.

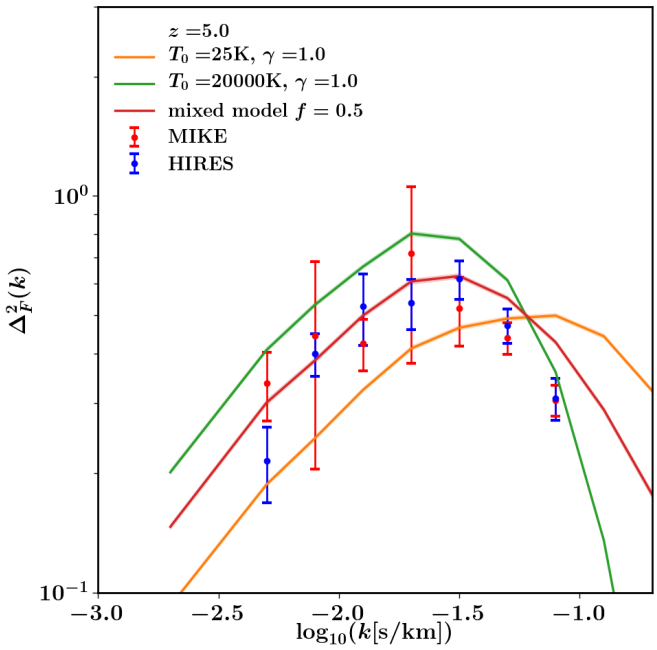

Figure 5.17: The effect of temperature fluctuations on FPS, for the case that bubbles are much larger than our simulated volume at $z = 5.0$. This case corresponds to a mixing fraction $f = 0.5$. For reference, we have drawn the data points of the MIKE and HIRES samples.

To illustrate the effect of fluctuations on the FPS, we contrast the FPS of two sets of mock spectra with an imposed temperature-density relation with different values of T_0: 25 K (i.e. negligible Doppler broadening and $T_0 = 2 \times 10^4$ K in Fig. 5.17, as well as a mock sample that uses half of the spectra from each of the two models. The FPS for the single-temperature models are normalized to have the same mean effective optical depth, $\tau_{\rm eff} = 2.0$, the mixed-temperature model is computed from the two normalized single-temperature models, and it is not normalized further. We find that in the mixed model the FPS is intermediate between the FPS of the hot and cold models. Hence, if the hot model represents the recently reionized regions in the IGM and the cold model the patches that were reionized previously and then cooled down, the mixed model looks like a model that is colder than the regions in the IGM that were reionized more recently.

Fig. 5.17 illustrates that fluctuations essentially decouple the behaviour of the FPS at large and small scales. If this is the case of the real IGM, then what we determine to be T_0 from fitting the cutoff does not correspond to either the hot or the cold temperature.

We leave a more detailed investigation of patchiness on the FPS and how that impacts on constraints on $\lambda_{\rm FS}$ to future work.

5.7.1.3 Redshift dependence of the cutoff

Finally, we need to check the redshift dependence of the cutoff scales.

The simplest case is that of Doppler broadening. Consider a sharp feature in $F(v)$, smoothed by Doppler broadening due to gas being at temperature T. The width of the smoothed feature in velocity space will be of order $\Delta v_b = (2k_{\rm B}T/m_{\rm H})^{1/2}$ (where $k_{\rm B}$ is Boltzmann's constant and $m_{\rm H}$ the proton mass). In terms of the Fourier transform of $F(v)$, this will correspond to a feature at the proper wavenumber[4]

$$k_{{\rm max},b} = \frac{\sqrt{2}}{\Delta v_b} = 0.11 \left(\frac{T}{10^4\,{\rm K}}\right)^{-1/2} ({\rm km\ s^{-1}})^{-1}\,, \tag{5.7.6}$$

which is independent of z, provided that T is constant.

How about pressure smoothing? The extent of the smoothing is approximately of order of the Jeans length [262], which in proper units is

$$\lambda_J = \sqrt{\frac{c_s^2\pi}{{\rm G}\rho}}\,. \tag{5.7.7}$$

Here, ρ is the total mass density (Dark Matter plus gas) of the absorber and c_s the sound speed. The corresponding velocity broadening is then $\Delta v_p = H(z)\lambda_J/(2\pi)$ [228]. At high enough redshift, the Hubble parameter scales like $\propto (1+z)^{3/2}$, and the density dependence of λ_J also scales like $\rho^{-1/2} \propto (1+z)^{3/2}$, making Δv_p also independent of redshift[5]. The corresponding value of $k_{\rm max}$ is

$$k_{{\rm max},p} = \frac{\sqrt{2}}{\Delta v_p} = 0.0760 \left(\frac{T}{10^4\,{\rm K}}\right)^{-1/2} \left({\rm km\ s^{-1}}\right)^{-1}\,. \tag{5.7.8}$$

The width of a feature due to Dark Matter free-streaming, $\lambda_{\rm FS}$, is imprinted in the linear transfer function, and is therefore constant in co-moving (as opposed to proper) coordinates. The velocity extent of such a feature is therefore $\Delta v_\lambda = H(z)\lambda_{\rm DM}/(1+z) \propto (1+z)^{1/2}$ at high-enough z, and in the FPS scales like $k_{\rm max,DM} \propto \Delta v_\lambda^{-1} \propto (1+z)^{-1/2}$ and hence is *not* independent of z. We can write its value as

$$k_{\rm max,DM} \;=\; \frac{1+z}{H(z)}\,\frac{1}{\lambda_{\rm DM}} \;=\; 0.007 \left(\frac{\lambda_{\rm DM}}{h^{-1}{\rm cMpc}}\right)^{-1} \left(\frac{6}{1+z}\right)^{1/2} \left({\rm km\ s^{-1}}\right)^{-1}\,. \tag{5.7.9}$$

[4]This is the case for Gaussian smoothing in the linear regime, with the factor 2 arising from the fact that the power spectrum is the square of the Fourier transform.

[5]We note that this no longer true at low redshift, where Δv_b and Δv_p scale differently with z.

The free-streaming scale $\lambda_{\rm FS}$ can be estimated as a position of the maximum of the linear matter power spectrum, see Fig. 5.2. For a particular case of 7 keV sterile neutrino that we will investigate in this work, this scale can be found e.g. in [136] as a function of lepton asymmetry. For the model with lepton asymmetry parameter $L_6 = 12$ [see 133, for the definition of L_6] the resulting scale is $\lambda_{\rm DM} \sim 0.07\,{\rm Mpc}/h$ which corresponds to $k_{\rm DM,max} \approx 0.1\,{\rm sec/km}$ at $z = 5$.

Finally, the finite resolution of the spectrograph imprints a feature that is constant in velocity space since the spectral resolution has a given value of $\mathcal{R} \equiv \Delta\lambda/\lambda = c/\Delta v_s$. The feature occurs at the redshift independent wavenumber

$$k_{{\rm max},s} = \frac{\sqrt{2}}{\Delta v_s} = 0.21 \left(\frac{6.6\,{\rm km\,s^{-1}}}{\Delta v_s}\right)^{-1} \left({\rm km\,s^{-1}}\right)^{-1} . \tag{5.7.10}$$

When simulating the above effects using a hydrodynamical simulation, yet another scale enters: the Nyquist frequency, set by the mean interparticle spacing. For a simulation with N^3 particles in a cubic volume with linear extent L, the corresponding scale is $\lambda_{\rm sim} = L/N^{1/3}$, and is constant in co-moving units. The corresponding $k_{\rm max}$ is of order

$$k_{\rm max,sim} = \frac{(1+z)}{H(z)} \frac{N^{1/3}}{L} \approx 0.27\ ({\rm km\,s^{-1}})^{-1} , \tag{5.7.11}$$

where the numerical value is for $z = 5$, $L = 20\,h^{-1}{\rm Mpc}$ and $N = 512^3$, suggesting that the numerical resolution needs to be at least this good in order not to compromise the location of any cutoff in mock spectra.

The conclusion of this is that the effects of free-streaming, compared to those of thermal broadening, pressure smoothing, finite spectral or numerical resolution, scale differently with z. The redshift dependence is sufficiently weak so to make little difference between $z = 5.4$ and $z = 5$, but the difference does become important comparing the FPS at $z = 3$ versus $z = 5$. The numerical values also suggest that free-streaming, Doppler and pressure broadening set-in at very similar values of k, and that the finite spectral resolution of KECK is unlikely to compromise the measurements.

5.7.1.4 Summary about cutoff in Cold Dark Matter

We find that indeed there are thermal histories that have a cutoff at scales smaller than those of the observed cutoff ($\lambda \sim 30\,{\rm km/s}$). These are the so-called late reionization (LateR) models described by [210] shown in Fig. 5.18. Mock FPS computed from CDM simulations with LateR reionization history and temperature of the order $T_0 \sim 5000\,{\rm K}$ exhibits a cutoff at the scale $\lambda \sim 18\,{\rm km/s} < \lambda_F \sim 30\,{\rm km/s}$ (Figures 5.16 and 5.19).

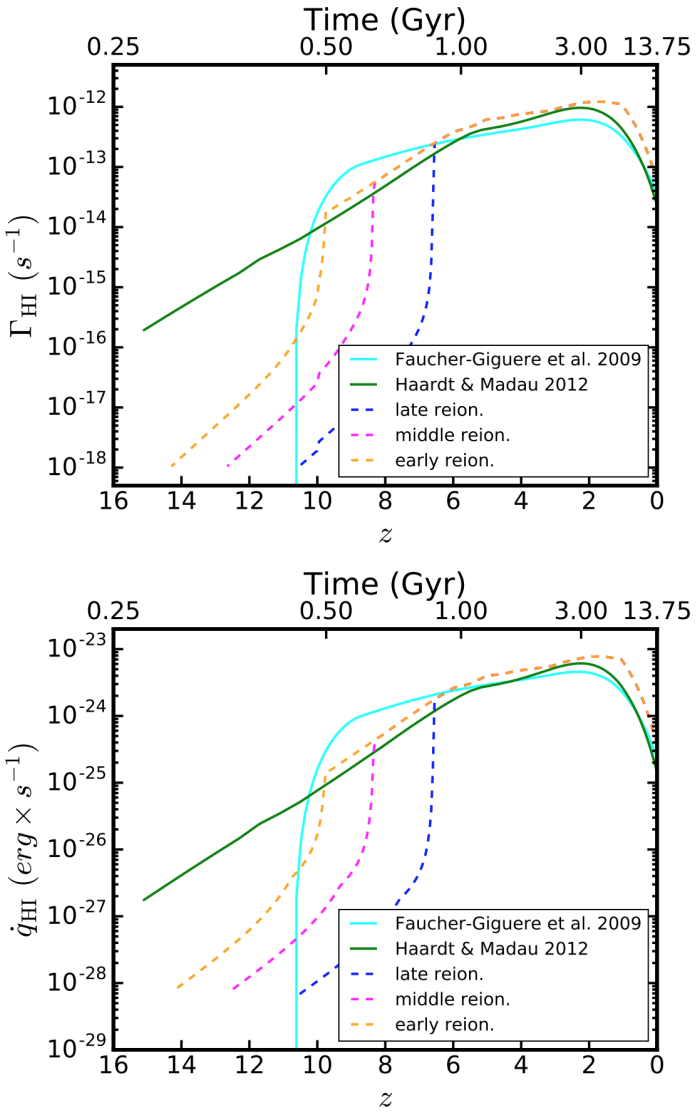

Figure 5.18: Photoionization rates Γ_{HI} and photoheating rates $\dot{q}_{HI}$ of some of the UVB models consistent with observations by [210] (*dashed lines*). Solid lines show analytical models by [263, 264] for comparison.

There exist realistic thermal histories in which the cutoff due to thermal effects is located at smaller scales. If a true thermal history is such, the cutoff needs to be explained by a different mechanism.

5.7.2 Cutoff in Warm Dark Matter

Even in the absence of thermal effects, WDM free-streaming introduces a cutoff in the FPS which resembles the observed cutoff for sufficiently 'cold' WDM models. Sterile neutrino

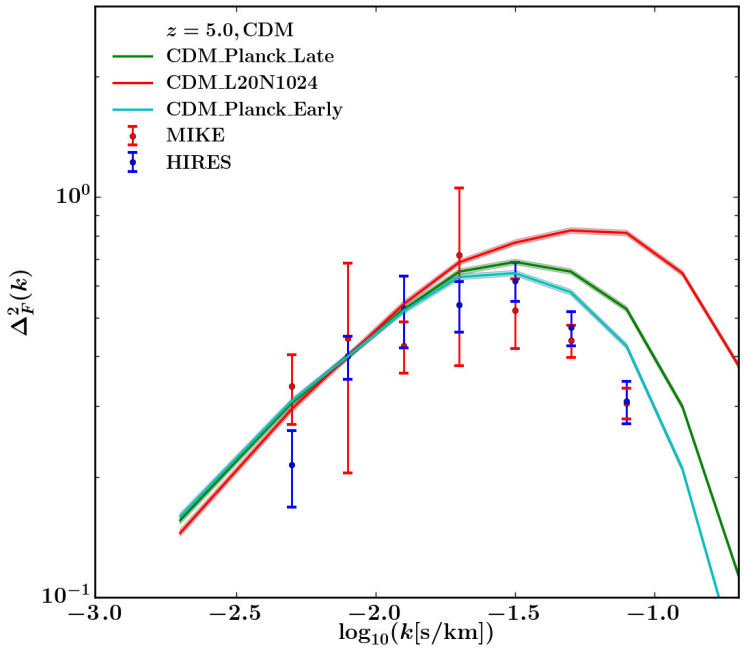

Figure 5.19: Mock FPS computed in simulations with late (*green line*), early (*cyan line*) and no reionization (*red line*). To demonstrate the effects of pressure, the temperature of the gas is set to $T_0 = 25\,\mathrm{K}$.

models with mass $7\,\mathrm{keV}$ and lepton asymmetry parameter $L_6 = 8$ or 12 (Fig. 5.20), appear consistent with the HIRES data.

But can WDM in combination with thermal effects produce the observed cutoff? As we saw in Section 5.7.1.3, the cutoffs due to different effects evolve differently. In addition to that, we expect both the temperature of the IGM and the filtering length to change with time. Since the data is available for 4 different redshifts, it is no longer practical to fit the data manually.

We have varied the parameters of our models to obtain the best fit to the cutoff in the FPS by performing a χ^2 analysis. To this end we use the evolution of the photo-ionisation and photo-heating rate of the *LateR* reionization model of [210], impose the temperature-density relation with $\gamma = 1$ in post-processing, and scale the simulated mean transmission to a range of values characterised by $\tau_{\mathrm{eff}} \equiv -\log\langle F \rangle$. As described in Section 5.5.5.1, we convolve the mock spectra with a Gaussian to mimic instrumental broadening, rebin to the pixel size of the spectrograph, and add Gaussian noise with standard deviation independent of wavelength and flux, corresponding to a signal to noise of 15 at the continuum level. We compute a grid of mock FPS, varying T_0 and τ_{eff} for CDM and WDM models. We compare the mock FPS to the observed FPS at redshifts $z = 4.2, 4.6, 5.0$ and 5.4. When doing the comparison we take into account that the scattering between different realisations is large due to the small size of QSO samples (see Section 5.6.2 for details). We take into account the sample variance by computing the χ^2 of a model using the covariance matrix computed from EAGLE_REF (as the boxsize of our reference simulation is not large

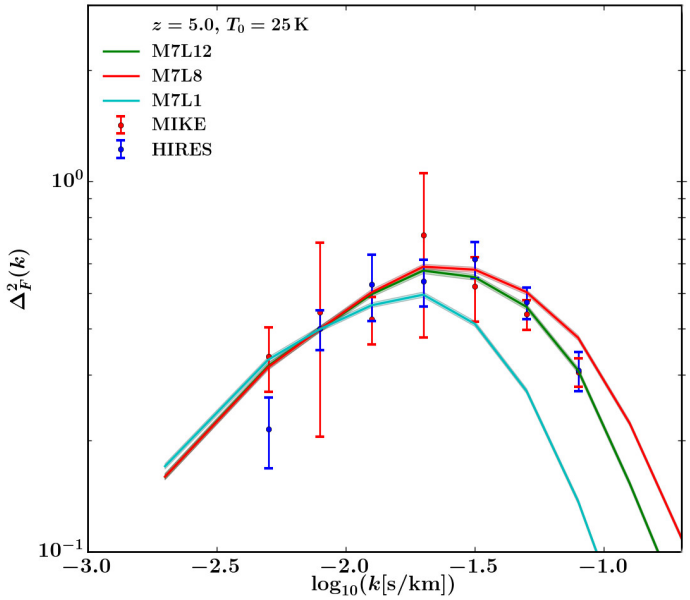

Figure 5.20: The cutoff in the mock flux power spectrum for various models, compared to the HIRES (*blue dots with error bars*) and MIKE data (*red dots with error bars*) at redshifts $z = 5.0$. For illustration purposes, we have scaled the amplitudes of the mock FPS in all cases such that it agrees with the HIRES value for the second point from the left, as a result different FPS in the same panel have different $\tau_{\rm eff}$. Here WDM simulations `WDM_L1`, `WDM_L8` and `WDM_L12` (*cyan, red and green curves, respectively*), with negligible Doppler broadening, $T_0 = 25$ K. DM free-streaming alone produces a cutoff in the FPS that resembles the observed cutoff for $L_6 = 8$ and 12.

enough to compute the covariance matrix). The rationale behind choosing `EAGLE_REF` was its large boxsize. the total length of the lines-of-sight in simulation was chosen equal to the total length of the observed QSO sample for each redshift range. Although EAGLE simulations do not have sufficient resolution at the smallest scales, we expect that the covariance is reproduced correctly.

The resulting contours for 68% and 95% confidence levels for HIRES data are shown in Fig. 5.21. In Table 5.3 we have compiled the values of the χ^2 for the best-fitting models.

As can be seen already from Fig. 5.20, the WDM model M7L12 has the FPS suppression due to the free-streaming that is consistent with the data. Therefore when varying T_0 in post-processing, WDM prefers temperatures with the scale $\lambda_b \ll \lambda_{\rm DM}$, see Fig. 5.21. At the same time, our simulation `M7L12_Planck_Late` predicts a temperature $T_0^{\rm sim} \simeq 6500$ K at all redshifts (this is also in agreement with findings of [210]). From Fig. 5.21 we see that the HIRES data is consistent with $T_0^{\rm sim}$ within its 95% confidence interval. Thus our procedure of post-processing is self-consistent – the temperature predicted by the simulations is consistent with the data. We show in Fig. 5.22 WDM model with this T_0 K as an example of a model with realistic thermal history, compatible with the data.

Table 5.3: Values of χ^2 for the best-fitting models shown in Figure 5.21. The number of dof is 5.

model	z	χ^2
CDM_Planck_Late	4.2	9.91
	4.6	4.61
	5.0	2.20
	5.4	3.25
M7L12_Planck_Late	4.2	6.04
	4.6	3.99
	5.0	3.44
	5.4	2.85

We cannot distinguish CDM and WDM without precise knowledge of the true thermal history. Determination of the temperature history during the Epoch of Reionization will categorically exclude one of the models.

Until there are observations allowing to identify the thermal history, the constraints being put on the Dark Matter candidates are model-dependent.

Marginalising over thermal histories.

We have demonstrated [1] that the cutoff in the FPS can be explained by any of the three effects (Doppler, pressure, DM free-streaming). This means that in order to obtain *robust* constraints on the properties of WDM particles one would need to marginalize over all astrophysical effects that can produce similar suppression in the FPS. The marginalisation over thermal histories (*i.e.* pressure effects) cannot be computed by brute-force: each thermal history requires its own full scale hydrodynamical simulation. On the other hand, marginalisation over Doppler broadening is possible in post-processing and is not computationally expensive.

To put robust constraints on the WDM, we need to *marginalize* over thermal histories. However, dependence of pressure effects on the whole thermal evolution forbids the direct exploration of the parameter space. The in order to constrain the WDM, we aim to find the *boundary* WDM model that would be excluded under any thermal history.

Therefore, we suggest the following procedure for obtaining *robust Lyman-α forest bounds [2]:*

(1) We have modelled the IGM using cosmological numerical simulations, using GADGET-2 [45]. The details about the numerical simulations can be found in [1]. In order to minimise the pressure effects, we have run our simulations with model of ultraviolet

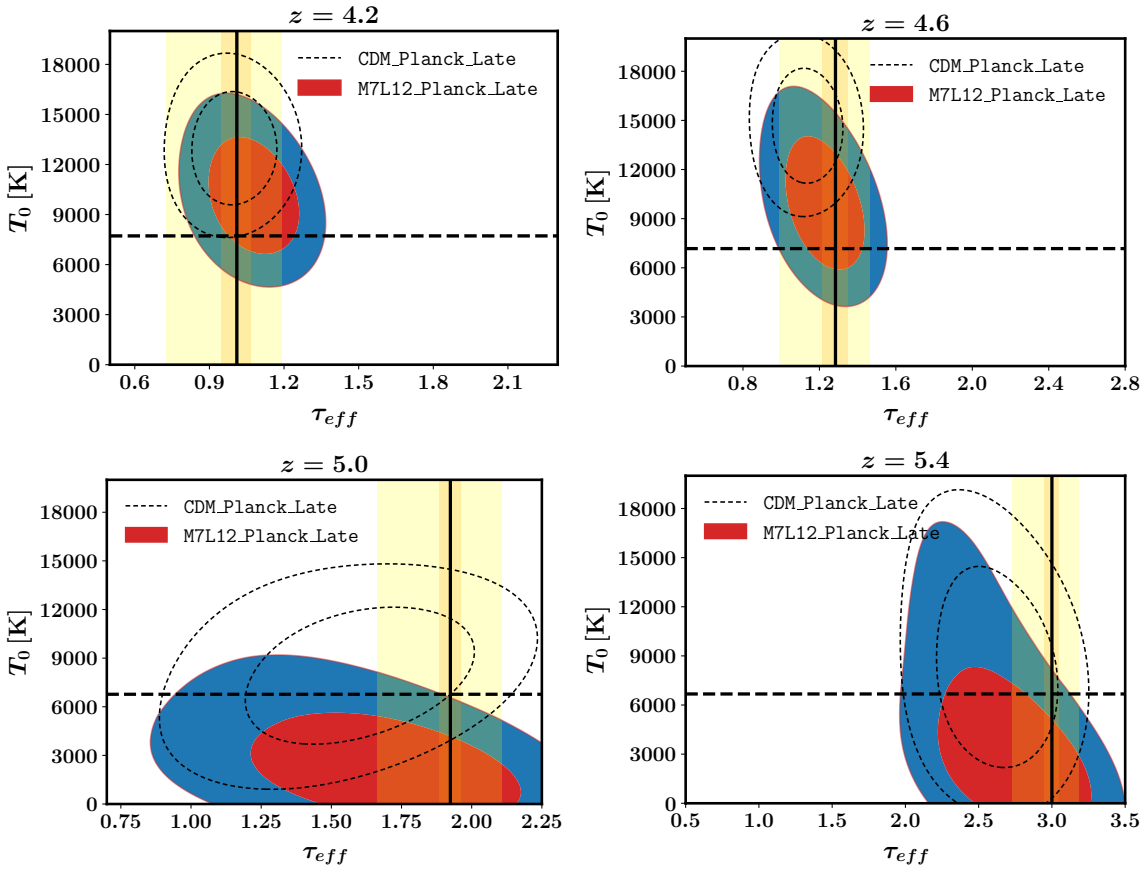

Figure 5.21: Confidence levels of mock FPS compared to the observed FPS of HIRES. We vary the temperature at the mean density, T_0, keeping $\gamma = 1$, and the value of the effective optical depth $\tau_{\rm eff}$. Solid lines and colour shaded areas correspond to 68% and 95% uncertainty intervals for the $m_{\rm SN} = 7\,{\rm keV}$ and $L_6 = 12$ WDM model, dashed lines are the same for the CDM model. Both models used the late reionisation model *LateR* from [210]. The contours take into account both HIRES error bars as reported by [150] and additional errors due to finite number of quasars in the dataset. The black solid vertical line is the directly estimated $\tau_{\rm eff}$ as reported in [150]. The horizontal line shows the value of T_0 as obtained in simulations with *LateR* UVB and without post-processing. It is in full agreement with the results of [210]. The systematic uncertainty on $\tau_{\rm eff}$ coming from the sample variance is estimated to be $\sim 10\%$, and we have indicated the resulting uncertainty on $\tau_{\rm eff}$ with the orange shade. The uncertainty on $\langle F \rangle$ due to continuum fitting is reported to be at the level $\sim 20\%$, and we have indicated the resulting uncertainty on $\tau_{\rm eff}$ with the yellow shade.

background (UVB) LATECOLD from [210]. This model starts at redshift $z = 6.7$, later than other thermal histories, considered in [210] but reproduces the measured temperature at late redshift. This choice of the thermal history is compatible with the constraint on reionization time [210]. By construction it gives the minimal filaments size.[6]

[6]We thank J. Onorbe for sharing with us the data of the LATECOLD thermal history that were not published

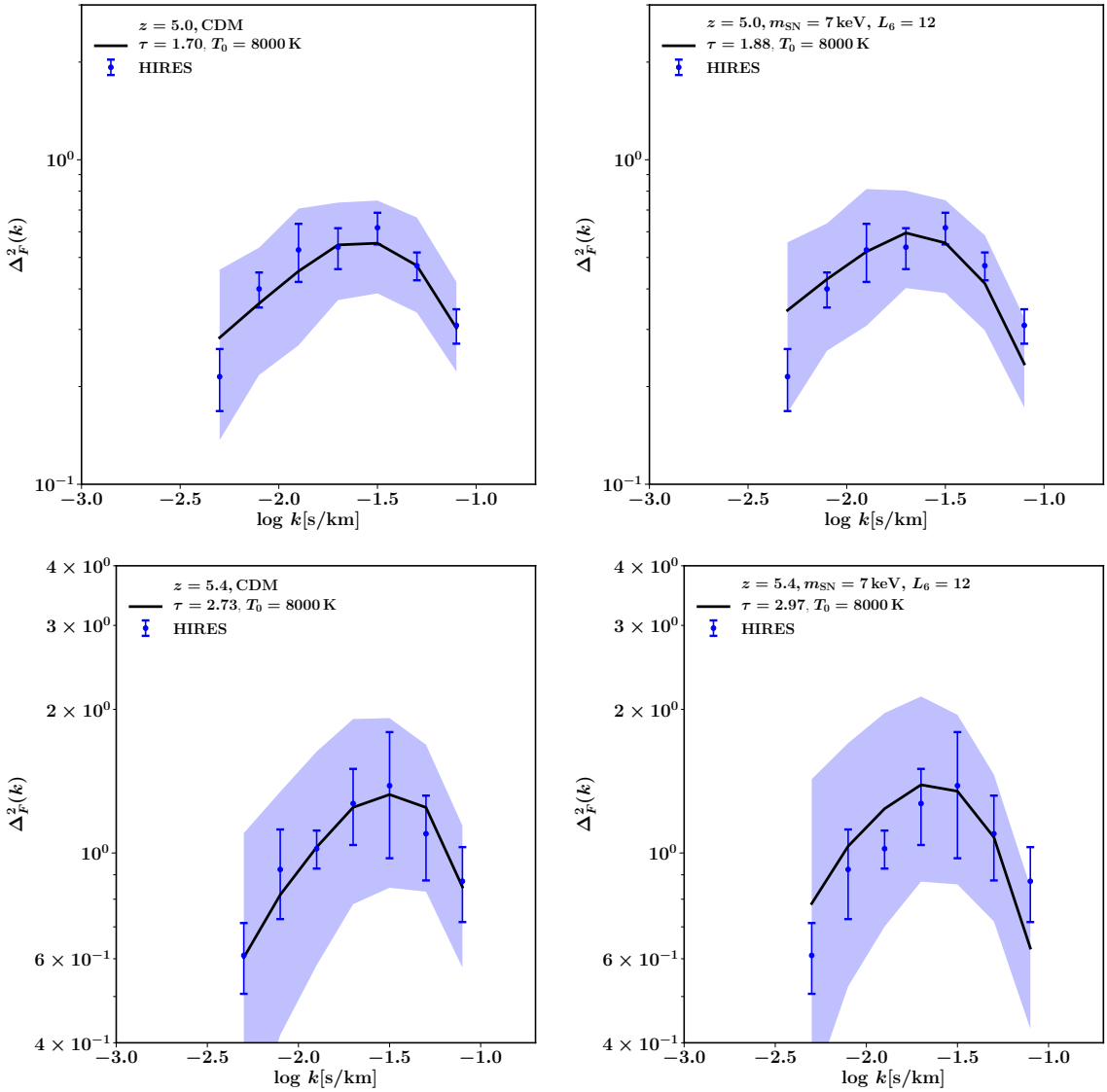

Figure 5.22: Examples of CDM and WDM models with realistic thermal histories, consistent with the high-resolution Lyman-α data. For both models we choose $T_0 = 8000$ K as predicted by our simulations with *LateR* UVB from [210]. The observed FPS inferred from HIRES is plotted as blue symbols with error bars as reported by [150]. One should keep in mind that the data points are correlated and therefore do not fluctuate independently. Shaded regions around the model show the variance due to different realisations of mock FPS (with the total length of the lines-of-sight in simulations equal to the length of observed spectra in the dataset for each redshift interval). The mock spectra have best-fit effective optical depth $\tau_{\rm eff} \equiv -\log\langle F\rangle$ for the fixed uniform temperature T imposed in post-processing. Top panels are for redshift $z = 5$ and bottom panels – for redshift $z = 5.4$ for CDM (*left panels*) and M7L12 SN model (*right panels*). The simulations are `CDM_Planck_Late` (left panels) and `M7L12_Planck_Late` (right panels).

together with the other thermal histories.

(2) We explicitly marginalise over the IGM temperature (*i.e.* Doppler broadening) adding their effects to the FPS in post-processing.

(3) We also marginalise over the *effective optical depth* $\tau_{\rm eff} = -\ln\langle F\rangle$. $\tau_{\rm eff}$ encompasses the information about the average absorption level (*i.e.* overall level of ionization of the IGM). The work [151] provided measurements of $\tau_{\rm eff}$ in each of the redshift bins together with the errorbars. We can vary $\tau_{\rm eff}$ in the post-processing of the spectra, by rescaling the optical depth in the spectra by a suitable factor.

(4) Our resulting model describing evolution of FPS contains 7 parameters: WDM mass $m_{\rm WDM}$, IGM temperature at cosmic mean density T_0 and $\tau_{\rm eff}$ (the latter two quantities are evaluated at redshifts $z = 4.2, 4.6, 5.0$). We consider logarithmic priors on the temperature and on the mass of Warm Dark Matter. We perform cosmological hydrodynamical numerical simulations, using GADGET-2 [45], for two distinct cosmological models: Cold Dark Matter (CDM) and WDM constituted of pure thermal relics with masses of $m_{\rm WDM} = 2.0\,{\rm keV}$. The details about the numerical simulations can be found in [1]. Starting from our simulations, we compute in post-processing the FPS for the parameter arranged on a tri-dimensional regular grid. Our final theoretical model is obtained by interpolating linearly the FPS across the grid. We perform a joint analysis on all the redshift intervals.

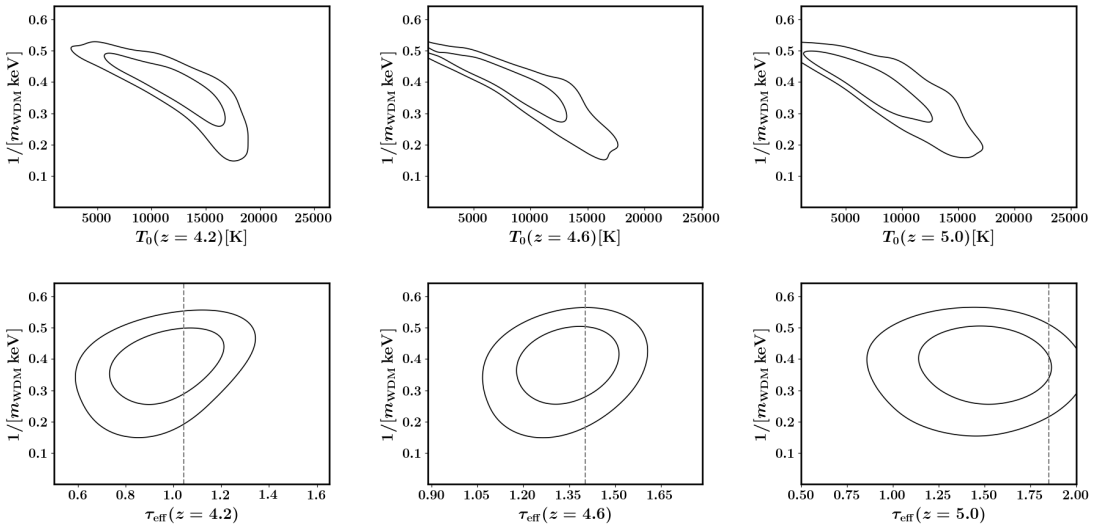

Figure 5.23: Confidence regions between the WDM mass, $m_{\rm WDM}$, the IGM mean temperature, T_0 and the effective optical depth $\tau_{\rm eff}$ at redshifts $z = 4.2,\ 4.6,\ 5.0$. Our analysis shows that if LATECOLD were the true history of reionisation, then the CDM would be ruled out. However, it is not possible to use this analysis to determine the IGM temperature in CDM for reionisation histories outside LATECOLD. By the same our analysis does not allow to determine the *lower* bounds on T_0 for a given WDM mass.

We run MCMC analysis and our 2σ contours are shown in Fig. 5.24 (full triangle) and Fig. 5.23 for the most relevant parameters. Two important comments are in order here:

1) Our contours do not reach CDM values ($1/m_{\rm WDM} = 0$). This does not mean that the CDM cosmology is excluded by the data. This simply indicates that in the LATECOLD reionizaiton scenario, the temperature alone is not sufficient to explain the suppression of the FPS.

2) Unlike the usual case, our temperature contours are only meaningful as the upper temperature limits. Indeed, they demonstrate that when minimizing pressure effects (as in LATECOLD) and switching off free streaming one is not able to explain the shape of the observed cutoff even with the temperatures in excess of $20000\,\mathrm{K}$. Best fit or higher temperature limits are exaggerated as they compensate pressure history that may be too low.

Results. We find that $m_{\rm WDM} \geq 2.0\,\mathrm{keV}$ at 2-σ level. Only the lower bounds for the temperature are shown. As mentioned above, the upper bound has no physical meaning, being an artifact of our procedure that fixed pressure effects at their lowest value. We show the 1 and 2-σ contours of the cosmic mean temperature T_0, the optical depth $\tau_{\rm eff}$, and the mass of the WDM $m_{\rm WDM}$ in Figure 5.24.

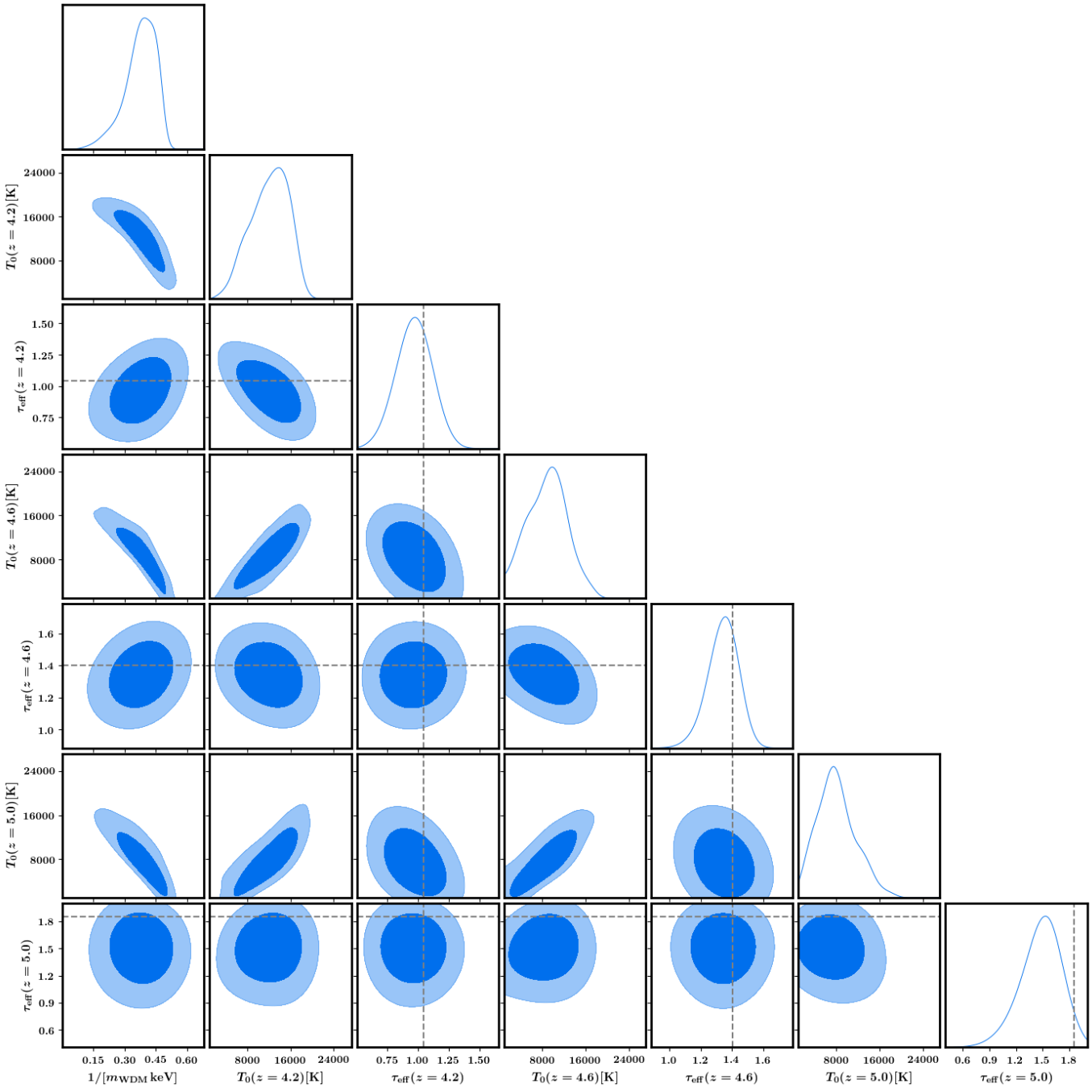

Figure 5.24: Confidence regions between the WDM mass $m_{\rm WDM}$ and the IGM mean temperature T_0 and effective optical depth at redshifts $z = 4.2, 4.6, 5.0$. The dashed grey lines are the $\tau_{\rm eff}$ as measured in [151]

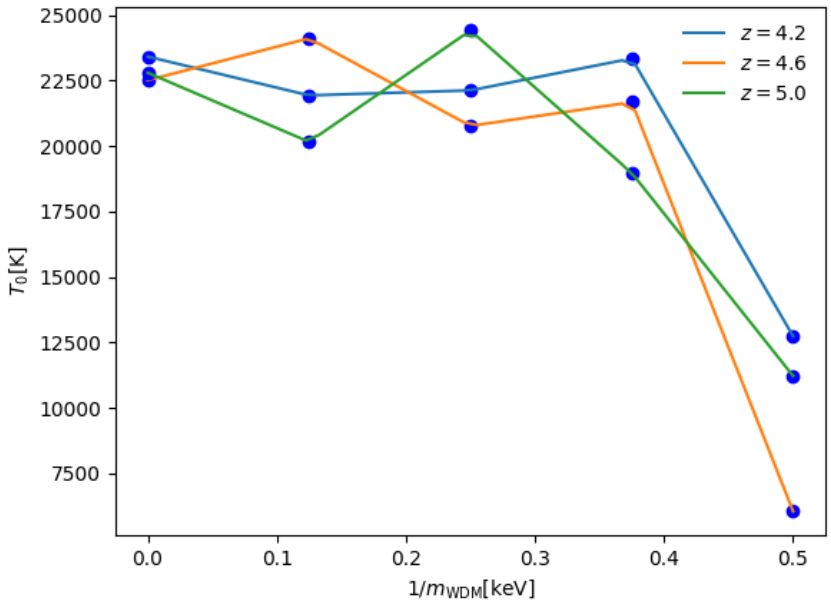

Figure 5.25: The 2-σ level upper limit on T_0 as a function of the inverse of $m_{\rm WDM}$. The upper limit has been estimated separately for each redshift interval, with fixing $m_{\rm WDM}$. We only show the interval $0 \leq m_{\rm WDM} \leq 0.5$, that is within the 2-$\sigma$ limit of the analysis of Figure 5.23. This result is in substantial agreement with the global fit that we have shown in Figure 5.23.

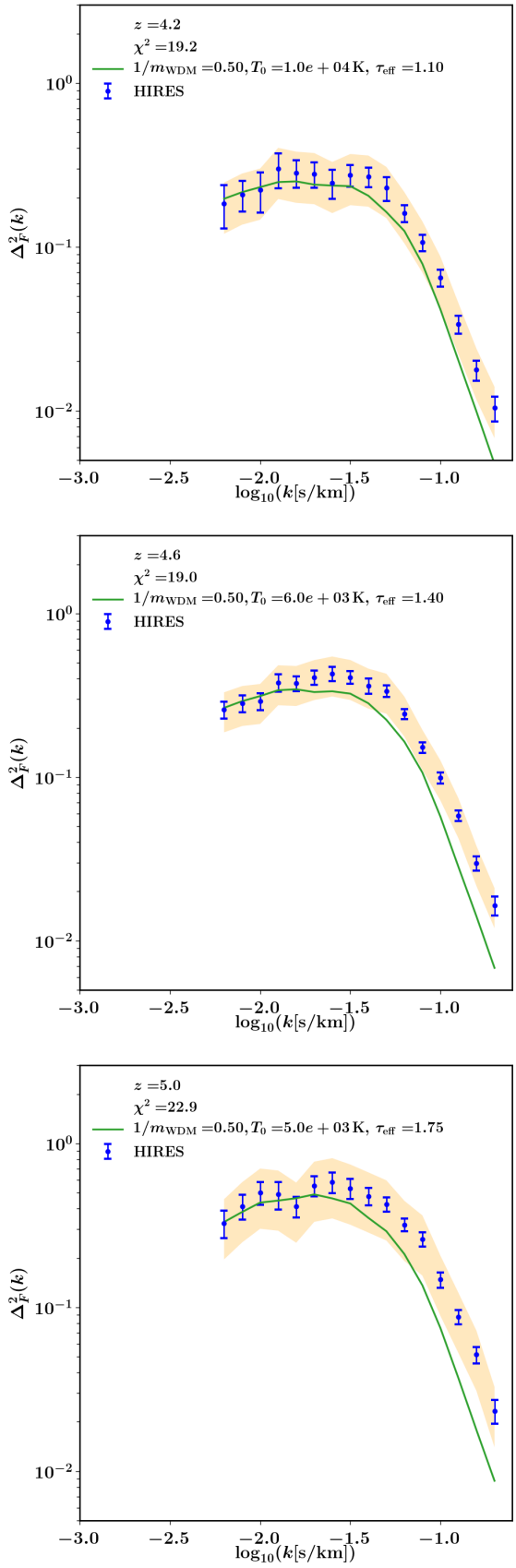

Figure 5.26: An example of cosmology with $m_{\rm WDM} = 2\,{\rm keV}$ and thermal history that is compatible within 2-σ with the observed flux power spectra. Orange shaded region shows the uncertainty in the measurement of FPS due to the sampling variance.

5.8 Conclusions

The power spectrum of the transmission in the Lyman-α forest (the flux power spectrum, FPS), exhibits a suppression on scales smaller than $\lambda_{\rm min} = 1/k_{\rm max} \sim 30\ {\rm km\ s^{-1}}$. Several physical effects may contribute to this observed cutoff: (*i*) Doppler broadening resulting from the finite temperature T_0 of the IGM, (*ii*) Jeans smoothing due to the finite pressure of the gas, and (*iii*) Dark Matter free streaming; these suppress power below scales λ_b, λ_p and $\lambda_{\rm FS}$, respectively. We have shown in Section 5.7 that, when λ is expressed in velocity units, λ_b and λ_p are independent of redshift z for a given value of T_0, whereas $\lambda_{\rm DM} \propto (1+z)^{1/2}$. This means that any smoothing of the density field due to WDM free-streaming will be most easily observable at high-redshift, and the observed FPS may provide constraints on the nature of the Dark Matter [150, 235–237], and possible be a 'WDM smoking gun'.

In our work we tried to answer two questions:

- Does the observed cutoff in the FPS favour Cold or Warm Dark Matter, or can both models provide acceptable fits to the existing data?
- Are the WDM models with large $\lambda_{\rm FS}$ that were previously excluded allowed if one considers a less restrictive thermal history?

To answer these questions we run a set of cosmological hydrodynamical simulations at very high resolution, varying λ_b, λ_p and $\lambda_{\rm FS}$ independently. We then compute mock spectra that mimic observational limitations (noise, finite spectral resolution and finite sample size), and compare the mock FPS to the observed FPS.

We demonstrate that all three effects (*i.e.* Doppler broadening, Jeans smoothing and DM free-streaming) yield a cutoff in the FPS that resembles the observed cutoff. Of course in reality all three effects will contribute at some level. In particular, Doppler broadening and Jeans smoothing both depend on the temperature T_0 of the IGM, and so always work together.

To answer the two questions posed above, we have tried to fit the observed FPS at redshifts $z = 5$ and 5.4 with (*i*) a CDM model (which has $\lambda_{\rm DM} = 0$), varying T_0 and the thermal history, and (*ii*) the particular case of a resonantly produced sterile neutrino WDM model (characterised by the mass of the particle, $m_{\rm DM}c^2 = 7$ keV, and the Lepton asymmetry parameter L_6, [153]), varying L_6, T_0 and the thermal history.

In addition to motivations based on particle physics (see *e.g.* [54]) our particular choice of WDM particle is motivated by the fact that: (*i*) its decay may have been observed as a 3.5 keV X-ray line in galaxies and clusters of galaxies [55–57], (*ii*) it produces galactic (sub)structures compatible with observations [136, 137], and (*iii*) it is apparently ruled out by the observed FPS [225].

Fig. 5.22 shows how the HIRES data is compatible with CDM and SN cosmologies if we choose relatively late reionisation model (*LateR* of [253]) so that λ_p is small and $T_0 \approx (7-8)\cdot 10^3$ K as predicted by this model. Both the assumed late reionisation redshift,

and the relatively low value of T_0, are reasonable and consistent with expectations and previous work. Crucially, a WDM model with $L_6 = 12$ and the same late redshift of reionisation also provides an acceptable fit to the data, provided $T_0 \leqslant 7000$ K. With such a low value of λ_b and λ_p, the FPS cutoff is mostly due to WDM free streaming.

From this comparison we conclude that the observed suppression in the FPS can be explained by thermal effects in CDM model but also by the free-streaming in a WDM model: current data do not strongly favour either possibility. We also find a reasonable fit for a WDM model that was previously ruled out by [150] and [235–237]. Our present analysis differs in a number of ways:

1. We vary the thermal history of the IGM within the allowed observational limits as discussed by [210, 253]. The previous works modeled the UVB according to [211]. The latter scenario is known to reionise the Universe too early with respect to current observations [210], plausibly overestimating λ_p.

2. We did not use any assumptions about the evolution $T_0(z)$ but inferred ranges of T_0 at $z = 5.0$ and $z = 5.4$ based on theoretical considerations and limits inferred from the Lyman-α data (see also [234]).

We also reconsidered the impact of peculiar velocities ('redshift space distortions'), which were claimed to affect the appearance of a cutoff at the smallest scales [246], but found these not to be important at the much higher resolution of our simulations.

We also demonstrated that spatial fluctuations in temperature, which are expected to be present close to reionisation, may dramatically affect the FPS. Spatial variations in T_0 can dramatically increase the amplitude of the FPS at the scale of the imposed fluctuations, effectively decoupling the large-scale and small-scale FPS. Unfortunately, this means that a model without fluctuations in T_0 will yield incorrect constraints on parameters if such fluctuations *are* present in the data. Interestingly, the nuisance caused by fluctuations in T_0 may actually be rather helpful if the cutoff in the FPS is in fact due to WDM, since in that case there would be no spatial fluctuations in the location of the cutoff – and the evolution with redshift of the cutoff would follow $\lambda_{\rm DM} \propto (1+z)^{1/2}$.

Moving away from Lyman-α and studying the small-scale Universe in the H I 21-cm line during the 'Dark Ages' [265] instead is currently almost science fiction, but ultimately may be the most convincing way of determining once and for all whether most of the Dark Matter in the Universe is warm or cold.

In the meantime, we have produced a new robust constraint on WDM from the most recent QSO spectra available from HIRES at high redshift. We have assumed a conservative thermal history for the IGM that is still consistent with reionization, and that gives the minimal size of the intergalactic structures. We have assumed that the intergalactic medium is optically thin, and that reionization happens uniformly in all the space. We aim to discuss

a more realistic reionization scenario in an upcoming publication. We have neglected the effect of undetected metals that may increase the power on the smallest scales, implying a weaker cutoff.

Appendix

5.A Convergence of the simulations in box-size

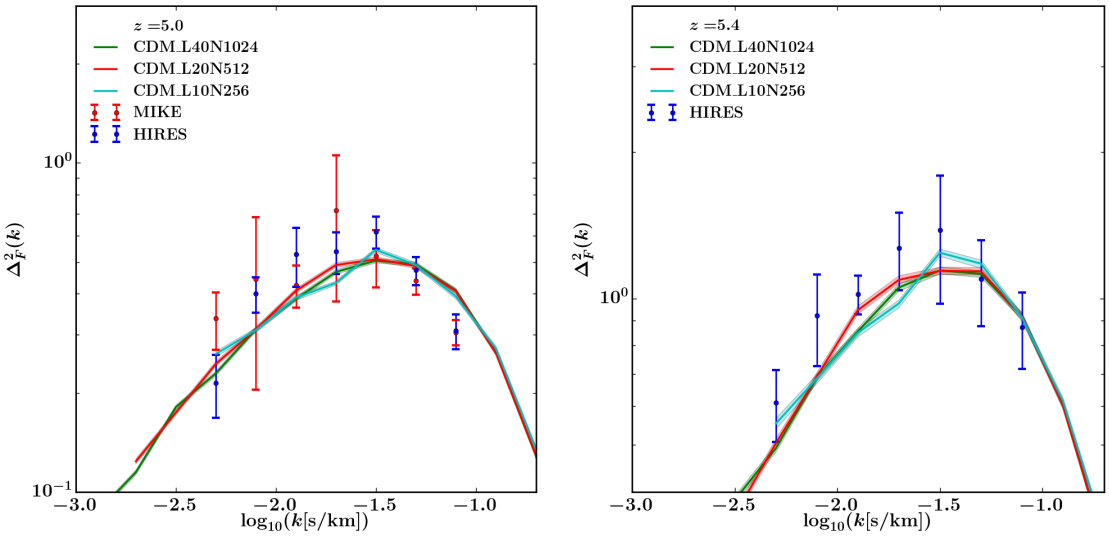

Figure 5.27: Study of the box-size needed in the numerical simulations to resolve the smallest scales probed by the HIRES and MIKE data samples. We show the FPS at $z = 5.0$ and $z = 5.4$ for three simulations without UVB and different box-sizes, yet same resolution. We have imposed a uniform temperature $T = 25\,\mathrm{K}$ in the post-processing of the spectra. We have applied the resolution of the HIRES spectrograph to the spectra, but we have excluded the effect of noise on the spectra. The FPS are normalized to the nominal observed optical depth of the observed spectra. The red solid line has a box-size $L = 10\,\mathrm{Mpc}/h$, the green solid line $L = 20\,\mathrm{Mpc}/h$, and the orange solid line $L = 40\,\mathrm{Mpc/h}$. The FPS for the case of $L = 10$, $L = 20\,\mathrm{Mpc}/h$, and $L = 40\,\mathrm{Mpc}/h$ agree with each other.

We have investigated the convergence of the FPS in box-size of the simulation with constant resolution. In section 5.B we have concluded that we need at least a number of particles $N = 1024^3$ and a boxsize $L = 20\,\mathrm{Mpc}/h$ to resolve the smallest scales reached by the data. Because we do not have the computing power to run a simulation with $L = 40\,\mathrm{Mpc}/h$ with this maximal resolution, we consider three simulations with $L = 10, 20, 40\,\mathrm{Mpc}/h$ and half the resolution. In this limit, we show in Figure 5.27 that the $L = 20\,\mathrm{Mpc/h}$ is sufficient to resolve the scales we intend to study.

5.B Numerical convergence

Before comparing the mock FPS to the observed FPS, we investigate to what extent the mock FPS is converged, both in terms of resolution and box size; the latter discussion can be found in Appendix 5.A. The gas temperature in our simulations that were performed without an imposed UVB is very low, and the gas distribution itself is not numerically converged at any of our resolutions. The effect of that on the FPS is shown in Fig. 5.15. For an imposed $T - \rho$ relation with $(T_0, \gamma) = (25\mathrm{K}, 1)$, the CDM FPS does show a cutoff at small scales, but the value of k_{max} increases with increasing particle count, N. The value of k_{max} for $N = 896^3$ and $N = 1024^3$ is nearly identical (see Fig. 5.15). We run our main analysis with the box size $L = 20\,\mathrm{Mpc}/h$ and $N = 1024^3$ of both DM and gas particles, the corresponding scale $k_{\mathrm{max,sim}}$ is therefore much larger than k_s.

Our resolution is higher than used previously [150] as the latter work was interested in hotter thermal histories – IGM with the temperature $T_0 \sim 10000 - 20000\,\mathrm{K}$ with a non-negligible thermal smoothing. Note that [150] also recongnized that $N = 512^3$ with $L = 20$ Mpc/h resolution is insufficient, but they applied a correcting factor to all power spectra. This factor was calibrated with a single simulation with $N = 896^3$, $L = 20\,\mathrm{Mpc}/h$. We instead rely on the intrinsic convergence of our simulations in the range of available data.

5.C Effect of noise

We investigate the effect of noise on the FPS. In our implementation of the noise, we have considered a Gaussian noise, with amplitude independent of flux or wavelength. In a spectrum from a bright quasar, the S/N is expected to increase with the flux. Because we have considered a S/N that is constant with flux and matches the S/N measured at the continuum level, we are likely underestimating the effect of noise in our analysis.

In some of the previous works on FPS in the Lyman-α forest, in particular [150, 235], the effect of noise on the flux PS is encoded with the application of a correction, that only depends on the chosen S/N and the redshift (in particular see Figure 16 in [150]), and not on other parameters of the IGM, such as the τ_{eff}. We have investigated whether the effect of noise is independent of the level of ionization of the IGM. In Figure 5.28 we show explicitly that the ratio between the FPS computed in the cases with and without noise depends on the value of the τ_{eff}, and the difference becomes larger on the smallest scales. This example was computed for a CDM simulation without, and with a uniform temperature $T = 2 \times 10^4\,\mathrm{K}$ imposed in post-processing. The effect of noise on the FPS is presumably being affected also by the temperature of examined spectra. Hence, we have resorted to including the effect of noise in our analysis by applying the noise to the spectra and then computing the resulting FPS.

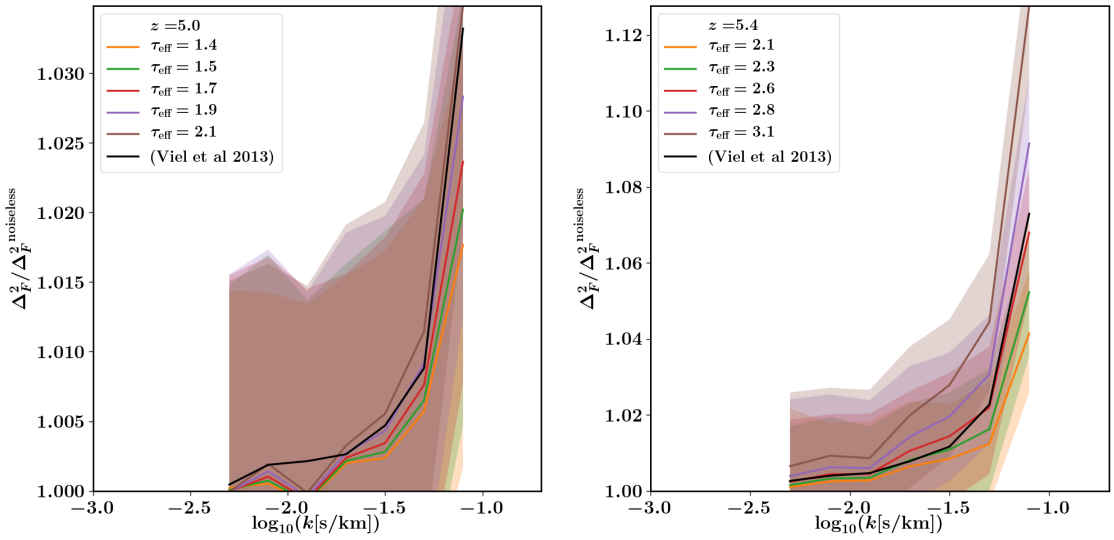

Figure 5.28: The effect of noise on FPS and its dependence from $\tau_{\rm eff}$. We show the ratio between the FPS computed with and without noise. We have considered a signal-to-noise ratio equal to 15, for a CDM simulation without UVB, and with imposed temperature in post-processing equal to $T = 2 \times 10^4$ K. The left (right) panel regards the redshift interval centered on $z = 5.0$ ($z = 5.4$). The solid lines refers to the mean of the ratio between the FPS computed with and without noise, the shaded region refer to the 1-σ uncertainty on the ratio. The black solid line is the correction for noise applied in [150], that is independent from $\tau_{\rm eff}$. We conclude that the effect of noise depends on $\tau_{\rm eff}$, and that accounting for noise only with a filter to the noiseless FPS is going to introduce a bias in the final estimate of the temperature.

5.D Estimation of mean flux uncertainties

Available measurements of mean flux at high redshifts are based on small samples of quasars. Data from [150] that we are using contains only 25 quasars with emission redshifts $4.48 \leq z_{\rm em} \leq 6.42$. Other works like [261] provide mean flux measurements also for only ~ 10 redshift intervals above $z = 5$. Even though quoted mean flux errors for individual spectra can be as low as $\sim 1\%$, tiny sample sizes suggest that undersampling of the density distribution is occurring.

To estimate this sampling error, we studied the distribution of mean flux for populations of mock spectra drawn from one of our simulations. To closely replicate the setup of [150], from 1000 lines of sight of the length $20\,{\rm Mpc}/h$ we prepared 142 l.o.s. of $140\,{\rm Mpc}/h$ by random concatenation (roughly corresponding to $\Delta z = 0.4$ used in [150] to bin the observations).

Next, we drew 1000 samples of the sizes 1, 10 and 100. For each population, we computed the standard as well as maximal deviations to gauge the sampling bias: Table 5.4. We see that typical error for $N_{sample} = 10$ is of the order of $4 - 5\%$.

On the other hand, the typical continuum level uncertainty is estimated to be $\sim 20\%$

[150]. Hence, uncertainty is dominated by continuum error.

Table 5.4: Means and standard deviations for populations of $140\,\mathrm{Mpc}/h$ mock spectra. $\bar{F}$ denotes averaging inside a population while angular brackets $\langle\rangle$ denote ensemble average.

z	N_{sample}	$\langle \bar{F} \rangle$	Standard Deviation
5.4	1	0.1136	± 0.0163 ($\pm 14.3\%$)
	10	0.1121	± 0.0056 ($\pm 5.0\%$)
	100	0.1121	± 0.0008 ($\pm 0.7\%$)
5.0	1	0.2086	± 0.0247 ($\pm 11.8\%$)
	10	0.2070	± 0.0078 ($\pm 3.8\%$)
	100	0.2065	± 0.0011 ($\pm 0.5\%$)

5.E Data analysis

Mock spectra are rescaled to match the corresponding experimental values of effective optical depth using the following procedure:

Algorithm 1 Rescaling of transmitted flux

```
function RescaleFluxes(spectra, τ_exp)
    τ ← −log⟨spectra⟩
    while |τ − τ_exp| > 10^−2 do
        x ← τ_exp/τ
        spectra ← spectra^x
        τ ← −log⟨spectra⟩
    return spectra
```

This algorithm is a linear rescaling of the optical depth $\tau_{eff} = -\log\langle F\rangle$ that is complicated by exponentiation: $\langle e^{\tau}\rangle \neq e^{\langle\tau\rangle}$.

Next, we apply Gaussian filtering to simulate the point-spread function of the instruments and rebin the spectra according to pixel sizes.

From rescaled and filtered spectra the flux contrast is computed $\delta_F(v) = \frac{F(v)}{\langle F\rangle} - 1$ and transformed into momentum space using FFT. Flux power spectrum is computed as follows:

$$\Delta_F^2(k) = \frac{1}{\pi} k P_F(k) \tag{5.E.1}$$

$$P_F(k) = V\left\langle |\tilde{\delta}(k)|^2 \right\rangle \tag{5.E.2}$$

$$\tilde{\delta}(k) = \frac{1}{V}\int dv e^{-ikv}\delta(v) \tag{5.E.3}$$

$$\delta(v) = \frac{F(v) - \langle F\rangle}{\langle F\rangle} \tag{5.E.4}$$

where V is the velocity interval over which the flux is given.

Flux is sampled in a linearly spaced velocity interval (v_{min}, v_{max}) with a step dv . To get the Fourier transform of the flux, we will use a Discrete Fourier Transform implemented by Fast Fourier Transform algorithm.

$$\tilde{\delta}(k) = \frac{1}{V}\int dv e^{-ikv}\delta(v) \tag{5.E.5}$$

$$\tilde{\delta}(k) \approx \frac{1}{V}\sum_{m=1}^{N} dv e^{-ik(v_{min}+mdv)}\delta(v_{min}+mdv) \tag{5.E.6}$$

$$= \frac{1}{V} dv e^{-ikv_{min}} \sum_{m=1}^{N} e^{-ikmdv}\delta(v_{min}+mdv) \tag{5.E.7}$$

Values of k are as well linearly sampled with a step $dk = \frac{2\pi}{Ndv} = \frac{2\pi}{V}$

$$\tilde{\delta}(ndk) \approx \frac{1}{V} dv e^{-i\,n\,dk\,v_{min}} \sum_{m=1}^{N} e^{-i\,n\,dk\,m\,dv}\delta(v_{min}+mdv) \tag{5.E.8}$$

$$= \frac{1}{V} dv e^{-i\,n\,dk\,v_{min}} \sum_{m=1}^{N} e^{-2\pi i\frac{nm}{N}}\delta(v_{min}+mdv) \tag{5.E.9}$$

The sum is exactly the Discrete Fourier Transform while the rest of the expression is the phase factor by which one has to multiply the output of the FFT to obtain the Fourier image.

Since the implementation of this is non-trivial and specific to a programming language, we present the Python code we use in Algorithm 2.

For computed power spectra we estimate the error bars on the mean using the bootstrap technique.

Finally, power spectra are averaged over logarithmically-spaced k-bins corresponding to the binning in data from [150]. For visual clarity we extend the number of bins to include also smaller scales.

Algorithm 2 Computation of flux power spectrum (Python)

```
# Given:
# spectra - array of spectra
# N - length of each spectrum
# V - velocity interval
import numpy as np
dv = V / N

freqs = np.fft.fftfreq(N) * (2. * np.pi / dv)
idx = np.argsort(freqs)
idx = idx[freqs[idx] >= 0]
freqs = freqs[idx] # select positive frequencies

mean = np.mean(spectra)

delta = (spectra - mean) / mean
fourier = np.fft.fft(delta)[idx] * dv / V
power_spectra = np.abs(fourier)**2 * V
dimless_power_spectra = power_spectra * freqs / np.pi
```

Bibliography

[1] PARTICLE DATA GROUP collaboration, *Review of Particle Physics*, *Phys. Rev.* **D98** (2018) 030001.

[2] ATLAS collaboration, *Observation of a new particle in the search for the Standard Model Higgs boson with the ATLAS detector at the LHC*, *Phys. Lett.* **B716** (2012) 1 [1207.7214].

[3] CMS collaboration, *Observation of a new boson at a mass of 125 GeV with the CMS experiment at the LHC*, *Phys. Lett.* **B716** (2012) 30 [1207.7235].

[4] ATLAS collaboration, *Combined measurements of Higgs boson production and decay using up to* 80 fb^{-1} *of proton-proton collision data at* $\sqrt{s} = 13$ *TeV collected with the ATLAS experiment*, [1909.02845].

[5] F. Bezrukov and M. Shaposhnikov, *Why should we care about the top quark Yukawa coupling?*, *J. Exp. Theor. Phys.* **120** (2015) 335 [1411.1923].

[6] CDF collaboration, *The CDF Detector: An Overview*, *Nucl. Instrum. Meth.* **A271** (1988) 387.

[7] D0 collaboration, *The D0 Detector*, *Nucl. Instrum. Meth.* **A338** (1994) 185.

[8] L. Evans and P. Bryant, *LHC Machine*, *Journal of Instrumentation* **3** (2008) S08001.

[9] F. Zwicky, *Die Rotverschiebung von extragalaktischen Nebeln*, *Helv. Phys. Acta* **6** (1933) 110.

[10] PLANCK collaboration, *Planck 2015 results. XIII. Cosmological parameters*, *Astron. Astrophys.* **594** (2016) A13 [1502.01589].

[11] Y. Sofue and V. Rubin, *Rotation curves of spiral galaxies*, *Ann. Rev. Astron. Astrophys.* **39** (2001) 137 [astro-ph/0010594].

[12] W. J. G. de Blok, F. Walter, E. Brinks, C. Trachternach, S.-H. Oh and R. C. Kennicutt, Jr., *High-Resolution Rotation Curves and Galaxy Mass Models from THINGS*, *Astron. J.* **136** (2008) 2648 [0810.2100].

[13] F. Lelli, S. S. McGaugh and J. M. Schombert, *SPARC: Mass Models for 175 Disk Galaxies with Spitzer Photometry and Accurate Rotation Curves*, *arXiv* (2016) [1606.09251].

[14] M. Korsaga, B. Epinat, P. Amram, C. Carignan, P. Adamczyk and A. Sorgho, *GHASP: an Hα kinematical survey of spiral galaxies – XIII. Distribution of luminous and dark matter in spiral and irregular nearby galaxies using Hα and HI rotation curves and WISE photometry*, [1909.08408].

[15] J. T. Kleyna, M. I. Wilkinson, N. W. Evans and G. Gilmore, *Ursa Major: A Missing low-mass CDM halo?*, *Astrophys. J.* **630** (2005) L141 [astro-ph/0507154].

[16] M. G. Walker, M. Mateo, E. W. Olszewski, J. Penarrubia, N. W. Evans and G. Gilmore, *A Universal Mass Profile for Dwarf Spheroidal Galaxies*, *Astrophys. J.* **704** (2009) 1274 [0906.0341].

[17] S. Giodini, L. Lovisari, E. Pointecouteau, S. Ettori, T. H. Reiprich and H. Hoekstra, *Scaling relations for galaxy clusters: properties and evolution*, *Space Sci. Rev.* **177** (2013) 247 [1305.3286].

[18] J. Silk et al., *Particle Dark Matter: Observations, Models and Searches*. Cambridge Univ. Press, Cambridge, 2010, 10.1017/CBO9780511770739, http://www.cambridge.org/uk/catalogue/catalogue.asp?isbn=9780521763684.

[19] C. S. Frenk, A. E. Evrard, S. D. M. White and F. J. Summers, *Galaxy dynamics in clusters*, *Astrophys. J.* **472** (1996) 460.

[20] H. Hoekstra, *Weak gravitational lensing*, *Proc. Int. Sch. Phys. Fermi* **186** (2014) 59 [1312.5981].

[21] PLANCK collaboration, *Planck 2018 results. VI. Cosmological parameters*, [1807.06209].

[22] M. Vogelsberger, S. Genel, V. Springel, P. Torrey, D. Sijacki, D. Xu et al., *Properties of galaxies reproduced by a hydrodynamic simulation*, Nature **509** (2014) 177.

[23] M. Vogelsberger, S. Genel, V. Springel, P. Torrey, D. Sijacki, D. Xu et al., *Introducing the Illustris Project: simulating the coevolution of dark and visible matter in the Universe*, *Mon. Not. Roy. Astron. Soc.* **444** (2014) 1518.

[24] J. Schaye, R. A. Crain, R. G. Bower, M. Furlong, M. Schaller, T. Theuns et al., *The EAGLE project: simulating the evolution and assembly of galaxies and their environments*, *Mon. Not. Roy. Astron. Soc.* **446** (2015) 521.

[25] V. Springel, R. Pakmor, A. Pillepich, R. Weinberger, D. Nelson, L. Hernquist et al., *First results from the IllustrisTNG simulations: matter and galaxy clustering*, *Mon. Not. Roy. Astron. Soc.* **475** (2018) 676.

[26] T. D. Brandt, *Constraints on MACHO Dark Matter from Compact Stellar Systems in Ultra-Faint Dwarf Galaxies*, *Astrophys. J.* **824** (2016) L31 [1605.03665].

[27] H. Niikura et al., *Microlensing constraints on primordial black holes with the Subaru/HSC Andromeda observation*, [1701.02151].

[28] S. Tremaine and J. E. Gunn, *Dynamical Role of Light Neutral Leptons in Cosmology*, *Phys. Rev. Lett.* **42** (1979) 407.

[29] J. Miralda-Escude, *A test of the collisional dark matter hypothesis from cluster lensing*, *Astrophys. J.* **564** (2002) 60 [astro-ph/0002050].

[30] D. Gorbunov, A. Khmelnitsky and V. Rubakov, *Is gravitino still a warm dark matter candidate?*, *JHEP* **12** (2008) 055 [0805.2836].

[31] A. Boyarsky, O. Ruchayskiy and D. Iakubovskyi, *A Lower bound on the mass of Dark Matter particles*, *JCAP* **0903** (2009) 005 [0808.3902].

[32] V. Domcke and A. Urbano, *Dwarf spheroidal galaxies as degenerate gas of free fermions*, *JCAP* **1501** (2015) 002 [1409.3167].

[33] S. D. M. White, C. S. Frenk and M. Davis, *Clustering in a neutrino-dominated universe*, *Astrophys. J.* **274** (1983) L1.

[34] B. W. Lee and S. Weinberg, *Cosmological Lower Bound on Heavy Neutrino Masses*, *Phys. Rev. Lett.* **39** (1977) 165.

[35] T. Marrodn Undagoitia and L. Rauch, *Dark matter direct-detection experiments*, *J. Phys.* **G43** (2016) 013001 [1509.08767].

[36] M. Battaglieri et al., *US Cosmic Visions: New Ideas in Dark Matter 2017: Community Report*, in *U.S. Cosmic Visions: New Ideas in Dark Matter College Park, MD, USA, March 23-25, 2017*, 2017, [1707.04591], http://lss.fnal.gov/archive/2017/conf/fermilab-conf-17-282-ae-ppd-t.pdf.

[37] T. Lin, *Dark matter models and direct detection*, *PoS* **333** (2019) 009 [1904.07915].

[38] G. Brooijmans et al., *Les Houches 2011: Physics at TeV Colliders New Physics Working Group Report*, in *Proceedings, 7th Les Houches Workshop on Physics at TeV Colliders: Les Houches, France, May 30-June 17, 2011*, pp. 221–463, 2012, [1203.1488], http://lss.fnal.gov/archive/preprint/fermilab-conf-12-924-t.shtml.

[39] WORKING GROUP 3 collaboration, *Beyond the Standard Model Physics at the HL-LHC and HE-LHC*, [1812.07831].

[40] J. Beacham et al., *Physics Beyond Colliders at CERN: Beyond the Standard Model Working Group Report*, [1901.09966].

[41] J. Alimena et al., *Searching for long-lived particles beyond the Standard Model at the Large Hadron Collider*, [1903.04497].

[42] J. Preskill, M. B. Wise and F. Wilczek, *Cosmology of the Invisible Axion*, *Phys. Lett.* **B120** (1983) 127.

[43] G. D. Martinez, J. S. Bullock, M. Kaplinghat, L. E. Strigari and R. Trotta, *Indirect Dark Matter Detection from Dwarf Satellites: Joint Expectations from Astrophysics and Supersymmetry*, *JCAP* **0906** (2009) 014 [0902.4715].

[44] A. V. Maccio, S. Paduroiu, D. Anderhalden, A. Schneider and B. Moore, *Cores in warm dark matter haloes: a Catch 22 problem*, *Mon. Not. Roy. Astron. Soc.* **424** (2012) 1105 [1202.1282].

[45] V. Springel, *The Cosmological simulation code GADGET-2*, *Mon. Not. Roy. Astron. Soc.* **364** (2005) 1105 [astro-ph/0505010].

[46] M. Vogelsberger, S. Genel, V. Springel, P. Torrey, D. Sijacki, D. Xu et al., *Properties of galaxies reproduced by a hydrodynamic simulation*, *Nature* **509** (2014) 177 [1405.1418].

[47] M. R. Lovell, C. S. Frenk, V. R. Eke, A. Jenkins, L. Gao and T. Theuns, *The properties of warm dark matter haloes*, *Mon. Not. Roy. Astron. Soc.* **439** (2014) 300 [1308.1399].

[48] S. Bose, W. A. Hellwing, C. S. Frenk, A. Jenkins, M. R. Lovell, J. C. Helly et al., *The COpernicus COmplexio: Statistical Properties of Warm Dark Matter Haloes*, *Mon. Not. Roy. Astron. Soc.* **455** (2016) 318 [1507.01998].

[49] S. Alekhin et al., *A facility to Search for Hidden Particles at the CERN SPS: the SHiP physics case*, *Rept. Prog. Phys.* **79** (2016) 124201 [1504.04855].

[50] A. D. Sakharov, *Violation of CP Invariance, C asymmetry, and baryon asymmetry of the universe*, *Pisma Zh. Eksp. Teor. Fiz.* **5** (1967) 32.

[51] T. Asaka and M. Shaposhnikov, *The nuMSM, dark matter and baryon asymmetry of the universe*, *Phys. Lett.* **B620** (2005) 17 [hep-ph/0505013].

[52] T. Asaka, S. Blanchet and M. Shaposhnikov, *The nuMSM, dark matter and neutrino masses*, *Phys. Lett.* **B631** (2005) 151 [hep-ph/0503065].

[53] S. Eijima, M. Shaposhnikov and I. Timiryasov, *Parameter space of baryogenesis in the νMSM*, *JHEP* **07** (2019) 077 [1808.10833].

[54] A. Boyarsky, M. Drewes, T. Lasserre, S. Mertens and O. Ruchayskiy, *Sterile Neutrino Dark Matter*, *Prog. Part. Nucl. Phys.* **104** (2019) 1 [1807.07938].

[55] E. Bulbul, M. Markevitch, A. Foster, R. K. Smith, M. Loewenstein and S. W. Randall, *Detection of An Unidentified Emission Line in the Stacked X-ray spectrum of Galaxy Clusters*, *Astrophys. J.* **789** (2014) 13 [1402.2301].

[56] A. Boyarsky, O. Ruchayskiy, D. Iakubovskyi and J. Franse, *Unidentified Line in X-Ray Spectra of the Andromeda Galaxy and Perseus Galaxy Cluster*, *Phys. Rev. Lett.* **113** (2014) 251301 [1402.4119].

[57] A. Boyarsky, J. Franse, D. Iakubovskyi and O. Ruchayskiy, *Checking the dark matter origin of 3.53 keV line with the Milky Way center*, *Phys. Rev. Lett.* **115** (2015) 161301 [1408.2503].

[58] O. Urban, N. Werner, S. W. Allen, A. Simionescu, J. S. Kaastra and L. E. Strigari, *A Suzaku Search for Dark Matter Emission Lines in the X-ray Brightest Galaxy Clusters*, *Mon. Not. Roy. Astron. Soc.* **451** (2015) 2447 [1411.0050].

[59] D. Iakubovskyi, E. Bulbul, A. R. Foster, D. Savchenko and V. Sadova, *Testing the origin of 3.55 keV line in individual galaxy clusters observed with XMM-Newton*, [1508.05186].

[60] J. Franse et al., *Radial Profile of the 3.55 keV line out to R_{200} in the Perseus Cluster*, *Astrophys. J.* **829** (2016) 124 [1604.01759].

[61] O. Ruchayskiy, A. Boyarsky, D. Iakubovskyi, E. Bulbul, D. Eckert, J. Franse et al., *Searching for decaying dark matter in deep XMMNewton observation of the Draco dwarf spheroidal*, *Mon. Not. Roy. Astron. Soc.* **460** (2016) 1390 [1512.07217].

[62] A. Neronov, D. Malyshev and D. Eckert, *Decaying dark matter search with NuSTAR deep sky observations*, *Phys. Rev.* **D94** (2016) 123504 [1607.07328].

[63] K. Perez, K. C. Y. Ng, J. F. Beacom, C. Hersh, S. Horiuchi and R. Krivonos, *Almost closing the MSM sterile neutrino dark matter window with NuSTAR*, *Phys. Rev.* **D95** (2017) 123002 [1609.00667].

[64] N. Cappelluti, E. Bulbul, A. Foster, P. Natarajan, M. C. Urry, M. W. Bautz et al., *Searching for the 3.5 keV Line in the Deep Fields with Chandra: the 10 Ms observations*, *Astrophys. J.* **854** (2018) 179 [1701.07932].

[65] S. Riemer-Srensen, *Constraints on the presence of a 3.5 keV dark matter emission line from Chandra observations of the Galactic centre*, *Astron. Astrophys.* **590** (2016) A71 [1405.7943].

[66] D. Malyshev, A. Neronov and D. Eckert, *Constraints on 3.55 keV line emission from stacked observations of dwarf spheroidal galaxies*, *Phys. Rev.* **D90** (2014) 103506 [1408.3531].

[67] S. Riemer-Srensen et al., *Dark matter line emission constraints from NuSTAR observations of the Bullet Cluster*, *Astrophys. J.* **810** (2015) 48 [1507.01378].

[68] M. E. Anderson, E. Churazov and J. N. Bregman, *Non-Detection of X-Ray Emission From Sterile Neutrinos in Stacked Galaxy Spectra*, *Mon. Not. Roy. Astron. Soc.* **452** (2015) 3905 [1408.4115].

[69] XQC collaboration, *Searching for keV Sterile Neutrino Dark Matter with X-ray Microcalorimeter Sounding Rockets*, *Astrophys. J.* **814** (2015) 82 [1506.05519].

[70] T. Tamura, R. Iizuka, Y. Maeda, K. Mitsuda and N. Y. Yamasaki, *An X-ray Spectroscopic Search for Dark Matter in the Perseus Cluster with Suzaku*, *Publ. Astron. Soc. Jap.* **67** (2015) 23 [1412.1869].

[71] N. Sekiya, N. Y. Yamasaki and K. Mitsuda, *A Search for a keV Signature of Radiatively Decaying Dark Matter with Suzaku XIS Observations of the X-ray Diffuse Background*, *Publ. Astron. Soc. Jap.* (2015) [1504.02826].

[72] HITOMI collaboration, *Hitomi constraints on the 3.5 keV line in the Perseus galaxy cluster*, *Astrophys. J.* **837** (2017) L15 [1607.07420].

[73] S. Dodelson and L. M. Widrow, *Sterile-neutrinos as dark matter*, *Phys. Rev. Lett.* **72** (1994) 17 [hep-ph/9303287].

[74] K. Bondarenko, A. Boyarsky, D. Gorbunov and O. Ruchayskiy, *Phenomenology of GeV-scale Heavy Neutral Leptons*, *JHEP* **11** (2018) 032 [1805.08567].

[75] P. Bodenheimer, *Depletion of Deuterium and Beryllium during Pre-Main Evolution*, *Astrophys. J.* **144** (1966) 103.

[76] R. I. Epstein, J. M. Lattimer and D. N. Schramm, *The origin of deuterium*, Nature **263** (1976) 198.

[77] G. Gamow, *The origin of elements and the separation of galaxies*, *Phys. Rev.* **74** (1948) 505.

[78] T. Otsuka, *Exotic nuclei and nuclear forces*, *Phys. Scripta* **T152** (2013) 014007.

[79] C. Pitrou, A. Coc, J.-P. Uzan and E. Vangioni, *Precision Big Bang Nucleosynthesis with the*

New Code PRIMAT, in *15th International Symposium on Origin of Matter and Evolution of the Galaxies (OMEG15) Kyoto, Japan, July 2-5, 2019*, 2019, [1909.12046].

[80] D. H. Wilkinson, *ANALYSIS OF NEUTRON BETA DECAY*, *Nucl. Phys.* **A377** (1982) 474.

[81] M. Pospelov and J. Pradler, *Metastable GeV-scale particles as a solution to the cosmological lithium problem*, *Phys. Rev.* **D82** (2010) 103514 [1006.4172].

[82] S. Dodelson, *Modern Cosmology*. Academic Press, Amsterdam, 2003, http://www.slac.stanford.edu/spires/find/books/www?cl=QB981:D62:2003.

[83] L. Kawano, *Let's go: Early universe. 2. Primordial nucleosynthesis: The Computer way*. 1992, http://inspirehep.net/search?p=FERMILAB-PUB-92-004-A.

[84] E. Lisi, S. Sarkar and F. L. Villante, *The big bang nucleosynthesis limit on N(neutrino)*, *Phys. Rev.* **D59** (1999) 123520 [hep-ph/9901404].

[85] L. Mendoza and C. J. Hogan, *A java calculator of standard big bang nucleosynthesis*, [astro-ph/9904334].

[86] A. Arbey, *AlterBBN: A program for calculating the BBN abundances of the elements in alternative cosmologies*, *Comput. Phys. Commun.* **183** (2012) 1822 [1106.1363].

[87] R. Consiglio, P. F. de Salas, G. Mangano, G. Miele, S. Pastor and O. Pisanti, *PArthENoPE reloaded*, *Comput. Phys. Commun.* **233** (2018) 237 [1712.04378].

[88] PARTICLE DATA GROUP collaboration, *Review of Particle Physics*, *Chin. Phys.* **C40** (2016) 100001.

[89] Y. I. Izotov and T. X. Thuan, *The Primordial Abundance of ^{4}He: Evidence for Non-Standard Big Bang Nucleosynthesis*, *Astrophys. J.* **710** (2010) L67 [1001.4440].

[90] Y. I. Izotov, T. X. Thuan and N. G. Guseva, *A new determination of the primordial He abundance using the He i λ10830 emission line: cosmological implications*, *Mon. Not. Roy. Astron. Soc.* **445** (2014) 778 [1408.6953].

[91] F. Iocco, G. Mangano, G. Miele, O. Pisanti and P. D. Serpico, *Primordial Nucleosynthesis: from precision cosmology to fundamental physics*, *Phys. Rept.* **472** (2009) 1 [0809.0631].

[92] R. Cooke and M. Fumagalli, *Measurement of the primordial helium abundance from the intergalactic medium*, *Nat. Astron.* **2** (2018) 957 [1810.06561].

[93] R. J. Cooke, M. Pettini and C. C. Steidel, *One Percent Determination of the Primordial Deuterium Abundance*, *Astrophys. J.* **855** (2018) 102 [1710.11129].

[94] R. I. Epstein, J. M. Lattimer and D. N. Schramm, *The Origin of deuterium*, *Nature* **263** (1976) 198.

[95] B. E. Wood, J. L. Linsky, G. Hebrard, G. M. Williger, H. W. Moos and W. P. Blair, *Two new low Galactic D/H measurements from FUSE*, *Astrophys. J.* **609** (2004) 838 [astro-ph/0403606].

[96] T. M. Bania, R. T. Rood and D. S. Balser, *The cosmological density of baryons from observations of 3He+ in the Milky Way*, *Nature* **415** (2002) 54.

[97] K. A. Olive, D. N. Schramm, S. T. Scully and J. W. Truran, *Low mass stars and the He-3 problem*, *Astrophys. J.* **479** (1997) 752 [astro-ph/9610039].

[98] M. Spite and F. Spite, *Lithium abundance at the formation of the Galaxy*, Nature **297** (1982) 483.

[99] L. Sbordone et al., *The metal-poor end of the Spite plateau. 1: Stellar parameters, metallicities and lithium abundances*, *Astron. Astrophys.* **522** (2010) A26 [1003.4510].

[100] Planck Collaboration, N. Aghanim, Y. Akrami, M. Ashdown, J. Aumont, C. Baccigalupi et al., *Planck 2018 results. VI. Cosmological parameters*, *ArXiv e-prints* (2018) [1807.06209].

[101] R. H. Cyburt, B. D. Fields, K. A. Olive and T.-H. Yeh, *Big Bang Nucleosynthesis: 2015*, *Rev. Mod. Phys.* **88** (2016) 015004 [1505.01076].

[102] M. Kawasaki and T. Moroi, *Electromagnetic cascade in the early universe and its application to the big bang nucleosynthesis*, *Astrophys. J.* **452** (1995) 506 [astro-ph/9412055].

[103] G. Mangano, G. Miele, S. Pastor, T. Pinto, O. Pisanti and P. D. Serpico, *Relic neutrino decoupling including flavor oscillations*, *Nucl. Phys.* **B729** (2005) 221 [hep-ph/0506164].

[104] A. D. Dolgov, S. H. Hansen, G. Raffelt and D. V. Semikoz, *Cosmological and astrophysical bounds on a heavy sterile neutrino and the KARMEN anomaly*, *Nucl. Phys.* **B580** (2000) 331 [hep-ph/0002223].

[105] A. D. Dolgov, S. H. Hansen, G. Raffelt and D. V. Semikoz, *Heavy sterile neutrinos: Bounds from big bang nucleosynthesis and SN1987A*, *Nucl. Phys.* **B590** (2000) 562 [hep-ph/0008138].

[106] O. Ruchayskiy and A. Ivashko, *Restrictions on the lifetime of sterile neutrinos from primordial nucleosynthesis*, *JCAP* **1210** (2012) 014 [1202.2841].

[107] M. Kawasaki, P. Kernan, H.-S. Kang, R. J. Scherrer, G. Steigman and T. P. Walker, *Big bang nucleosynthesis constraints on the tau-neutrino mass*, *Nucl. Phys.* **B419** (1994) 105.

[108] S. Hannestad, *What is the lowest possible reheating temperature?*, *Phys. Rev.* **D70** (2004) 043506 [astro-ph/0403291].

[109] B. Gough, *GNU Scientific Library Reference Manual - Third Edition*. Network Theory Ltd., 3rd ed., 2009, https://dl.acm.org/citation.cfm?id=1538674.

[110] C. Pitrou, A. Coc, J.-P. Uzan and E. Vangioni, *Precision big bang nucleosynthesis with improved Helium-4 predictions*, *Phys. Rept.* **754** (2018) 1 [1801.08023].

[111] E. Grohs, G. M. Fuller, C. T. Kishimoto, M. W. Paris and A. Vlasenko, *Neutrino energy transport in weak decoupling and big bang nucleosynthesis*, *Phys. Rev.* **D93** (2016) 083522 [1512.02205].

[112] E. P. Hubble, *Extragalactic nebulae*, *Astrophys. J.* **64** (1926) 321.

[113] H. Shapley and A. Ames, *A Survey of the External Galaxies Brighter than the Thirteenth Magnitude*, *Annals of Harvard College Observatory* **88** (1932) 41.

[114] E. Hubble, *The Distribution of Extra-Galactic Nebulae*, *Astrophys. J.* **79** (1934) 8.

[115] M. Colless et al., *The 2dF Galaxy Redshift Survey: Final data release*, [astro-ph/0306581].

[116] J. R. Gott, III, M. Juric, D. Schlegel, F. Hoyle, M. Vogeley, M. Tegmark et al., *A map of the universe*, *Astrophys. J.* **624** (2005) 463 [astro-ph/0310571].

[117] L. S. Sparke and J. S. Gallagher, *Galaxies in the universe: an introduction*. Cambridge Univ. Press, 2010.

[118] F. Fontanot, G. De Lucia, P. Monaco, R. S. Somerville and P. Santini, *The Many Manifestations of Downsizing: Hierarchical Galaxy Formation Models confront Observations*, *Mon. Not. Roy. Astron. Soc.* **397** (2009) 1776 [0901.1130].

[119] BOSS collaboration, *The clustering of galaxies in the SDSS-III Baryon Oscillation Spectroscopic Survey: baryon acoustic oscillations in the Data Releases 10 and 11 Galaxy samples*, *Mon. Not. Roy. Astron. Soc.* **441** (2014) 24 [1312.4877].

[120] E. Aubourg et al., *Cosmological implications of baryon acoustic oscillation measurements*, *Phys. Rev.* **D92** (2015) 123516 [1411.1074].

[121] DES collaboration, *Dark Energy Survey Year 1 Results: A Precise H0 Estimate from DES Y1, BAO, and D/H Data*, *Mon. Not. Roy. Astron. Soc.* **480** (2018) 3879 [1711.00403].

[122] Ya. B. Zeldovich, *Gravitational instability: An Approximate theory for large density perturbations*, *Astron. Astrophys.* **5** (1970) 84.

[123] M. Crocce, S. Pueblas and R. Scoccimarro, *Transients from initial conditions in cosmological simulations*, *Monthly Notices of the Royal Astronomical Society* **373** (2006) 369381.

[124] J. Makino and T. Saitoh, *Astrophysics with GRAPE*, *PTEP* **2012** (2012) 01A303.

[125] J. Barnes and P. Hut, *A Hierarchical 0 Nlogn Force Calculation Algorithm*, *Nature* **324** (1986) 446.

[126] M. J. Berger and P. Colella, *Local Adaptive Mesh Refinement for Shock Hydrodynamics*, *Journal of Computational Physics* **82** (1989) 64.

[127] R. A. Gingold and J. J. Monaghan, *Smoothed particle hydrodynamics: theory and application to non-spherical stars.*, *Mon. Not. Roy. Astron. Soc.* **181** (1977) 375.

[128] J. J. Monaghan, *Smoothed particle hydrodynamics*, *Ann. Rev. Astron. Astrophys.* **30** (1992) 543.

[129] N. Katz, D. H. Weinberg and L. Hernquist, *Cosmological simulations with TreeSPH*, *Astrophys. J.Suppl.* **105** (1996) 19 [astro-ph/9509107].

[130] V. Springel et al., *Simulating the joint evolution of quasars, galaxies and their large-scale distribution*, *Nature* **435** (2005) 629 [astro-ph/0504097].

[131] V. Springel, C. S. Frenk and S. D. M. White, *The large-scale structure of the Universe*, *Nature* **440** (2006) 1137 [astro-ph/0604561].

[132] V. Springel et al., *First results from the IllustrisTNG simulations: matter and galaxy clustering*, *Mon. Not. Roy. Astron. Soc.* **475** (2018) 676 [1707.03397].

[133] A. Boyarsky, J. Lesgourgues, O. Ruchayskiy and M. Viel, *Lyman-α constraints on warm and on warm-plus-cold dark matter models*, J. Cosmology Astropart. Phys. **5** (2009) 012 [0812.0010].

[134] A. Schneider, R. E. Smith and D. Reed, *Halo mass function and the free streaming scale*, *Mon. Not. Roy. Astron. Soc.* **433** (2013) 1573 [1303.0839].

[135] R. E. Angulo, O. Hahn and T. Abel, *The warm dark matter halo mass function below the cut-off scale*, *Mon. Not. Roy. Astron. Soc.* **434** (2013) 3337 [1304.2406].

[136] M. R. Lovell, S. Bose, A. Boyarsky, S. Cole, C. S. Frenk, V. Gonzalez-Perez et al., *Satellite galaxies in semi-analytic models of galaxy formation with sterile neutrino dark matter*, *Mon. Not. Roy. Astron. Soc.* **461** (2016) 60 [1511.04078].

[137] M. R. Lovell, S. Bose, A. Boyarsky, R. A. Crain, C. S. Frenk, W. A. Hellwing et al., *Properties of Local Group galaxies in hydrodynamical simulations of sterile neutrino dark matter cosmologies*, *Mon. Not. Roy. Astron. Soc.* **468** (2017) 4285 [1611.00010].

[138] R. Li, C. S. Frenk, S. Cole, L. Gao, S. Bose and W. A. Hellwing, *Constraints on the identity of the dark matter from strong gravitational lenses*, *Mon. Not. Roy. Astron. Soc.* **460** (2016) 363 [1512.06507].

[139] D. Erkal, V. Belokurov, J. Bovy and J. L. Sanders, *The number and size of subhalo-induced gaps in stellar streams*, *Mon. Not. Roy. Astron. Soc.* **463** (2016) 102 [1606.04946].

[140] S. Tremaine and J. E. Gunn, *Dynamical role of light neutral leptons in cosmology*, *Physical Review Letters* **42** (1979) 407.

[141] A. V. Maccio, S. Paduroiu, A. Schneider and B. Moore, *Cores in warm dark matter haloes: a Catch 22 problem*, *Mon. Not. Roy. Astron. Soc.* **424** (2012) 1105 [1202.1282].

[142] S. Shao, L. Gao, T. Theuns and C. S. Frenk, *The phase-space density of fermionic dark matter haloes*, *Mon. Not. Roy. Astron. Soc.* **430** (2013) 2346 [1209.5563].

[143] J. F. Navarro, V. R. Eke and C. S. Frenk, *The cores of dwarf galaxy haloes*, *Mon. Not. Roy. Astron. Soc.* **283** (1996) L72 [astro-ph/9610187].

[144] F. Governato, C. Brook, L. Mayer, A. Brooks, G. Rhee, J. Wadsley et al., *Bulgeless dwarf galaxies and dark matter cores from supernova-driven outflows*, Nature **463** (2010) 203 [0911.2237].

[145] A. Pontzen and F. Governato, *How supernova feedback turns dark matter cusps into cores*, *Mon. Not. Roy. Astron. Soc.* **421** (2012) 3464 [1106.0499].

[146] K. A. Oman, J. F. Navarro, A. Fattahi, C. S. Frenk, T. Sawala, S. D. M. White et al., *The unexpected diversity of dwarf galaxy rotation curves*, *Mon. Not. Roy. Astron. Soc.* **452** (2015) 3650 [1504.01437].

[147] R. Adhikari et al., *A White Paper on keV Sterile Neutrino Dark Matter*, *JCAP* **1701** (2017) 025 [1602.04816].

[148] U. Seljak, A. Makarov, P. McDonald and H. Trac, *Can sterile neutrinos be the dark matter?*, *Phys. Rev. Lett.* **97** (2006) 191303 [astro-ph/0602430].

[149] M. Viel, J. Lesgourgues, M. G. Haehnelt, S. Matarrese and A. Riotto, *Can sterile neutrinos be ruled out as warm dark matter candidates?*, *Phys. Rev. Lett.* **97** (2006) 071301 [astro-ph/0605706].

[150] M. Viel, G. D. Becker, J. S. Bolton and M. G. Haehnelt, *Warm dark matter as a solution to the small scale crisis: New constraints from high redshift Lyman-α forest data*, Phys. Rev. D **88** (2013) 043502 [1306.2314].

[151] E. Boera, G. D. Becker, J. S. Bolton and F. Nasir, *Revealing Reionization with the Thermal History of the Intergalactic Medium: New Constraints from the Lyα Flux Power Spectrum*, *Astrophys. J.* **872** (2019) 101 [1809.06980].

[152] P. Bode, J. P. Ostriker and N. Turok, *Halo formation in warm dark matter models*, *Astrophys. J.* **556** (2001) 93 [astro-ph/0010389].

[153] A. Boyarsky, J. Lesgourgues, O. Ruchayskiy and M. Viel, *Realistic sterile neutrino dark matter with keV mass does not contradict cosmological bounds*, *Phys. Rev. Lett.* **102** (2009) 201304 [0812.3256].

[154] L. Covi, H.-B. Kim, J. E. Kim and L. Roszkowski, *Axinos as dark matter*, *JHEP* **05** (2001) 033 [hep-ph/0101009].

[155] K.-Y. Choi, J. E. Kim and L. Roszkowski, *Review of axino dark matter*, *J. Korean Phys. Soc.* **63** (2013) 1685 [1307.3330].

[156] T. Moroi, H. Murayama and M. Yamaguchi, *Cosmological constraints on the light stable gravitino*, *Phys. Lett.* **B303** (1993) 289.

[157] X.-D. Shi and G. M. Fuller, *A New dark matter candidate: Nonthermal sterile neutrinos*, *Phys. Rev. Lett.* **82** (1999) 2832 [astro-ph/9810076].

[158] M. Laine and M. Shaposhnikov, *Sterile neutrino dark matter as a consequence of nuMSM-induced lepton asymmetry*, *JCAP* **0806** (2008) 031 [0804.4543].

[159] K. Kashiyama and M. Oguri, *Detectability of Small-Scale Dark Matter Clumps with Pulsar Timing Arrays*, [1801.07847].

[160] J. S. Bullock and M. Boylan-Kolchin, *Small-Scale Challenges to the ΛCDM Paradigm*, *Ann. Rev. Astron. Astrophys.* **55** (2017) 343 [1707.04256].

[161] B. Moore, S. Ghigna, F. Governato, G. Lake, T. R. Quinn, J. Stadel et al., *Dark matter substructure within galactic halos*, *Astrophys. J.* **524** (1999) L19 [astro-ph/9907411].

[162] A. A. Klypin, A. V. Kravtsov, O. Valenzuela and F. Prada, *Where are the missing Galactic satellites?*, *Astrophys. J.* **522** (1999) 82 [astro-ph/9901240].

[163] A. Fattahi, J. F. Navarro, T. Sawala, C. S. Frenk, L. V. Sales, K. Oman et al., *The cold dark*

matter content of Galactic dwarf spheroidals: no cores, no failures, no problem, [1607.06479].

[164] R. A. Flores and J. R. Primack, *Observational and theoretical constraints on singular dark matter halos*, *Astrophys. J.* **427** (1994) L1 [astro-ph/9402004].

[165] B. Moore, *Evidence against dissipation-less dark matter from observations of galaxy haloes*, *Nature* **370** (1994) 629.

[166] M. Boylan-Kolchin, J. S. Bullock and M. Kaplinghat, *Too big to fail? The puzzling darkness of massive Milky Way subhaloes*, *Mon. Not. Roy. Astron. Soc.* **415** (2011) L40 [1103.0007].

[167] M. Boylan-Kolchin, J. S. Bullock and M. Kaplinghat, *The Milky Way's bright satellites as an apparent failure of LCDM*, *Mon. Not. Roy. Astron. Soc.* **422** (2012) 1203 [1111.2048].

[168] S. Mashchenko, J. Wadsley and H. M. P. Couchman, *Stellar Feedback in Dwarf Galaxy Formation*, *Science* **319** (2008) 174 [0711.4803].

[169] J. Wang, C. S. Frenk, J. F. Navarro, L. Gao and T. Sawala, *The missing massive satellites of the Milky Way*, *Mon. Not. Roy. Astron. Soc.* **424** (2012) 2715 [1203.4097].

[170] T. Sawala et al., *The APOSTLE simulations: solutions to the Local Group's cosmic puzzles*, *Mon. Not. Roy. Astron. Soc.* **457** (2016) 1931 [1511.01098].

[171] Q. Guo, A. P. Cooper, C. Frenk, J. Helly and W. A. Hellwing, *The Milky Way system in Λ cold dark matter cosmological simulations*, *Mon. Not. Roy. Astron. Soc.* **454** (2015) 550 [1503.08508].

[172] K. A. Oman, J. F. Navarro, L. V. Sales, A. Fattahi, C. S. Frenk, T. Sawala et al., *Missing dark matter in dwarf galaxies?*, *Mon. Not. Roy. Astron. Soc.* **460** (2016) 3610 [1601.01026].

[173] G. Despali, S. Vegetti, S. D. M. White, C. Giocoli and F. C. van den Bosch, *Modelling the line-of-sight contribution in substructure lensing*, *Mon. Not. Roy. Astron. Soc.* **475** (2018) 5424 [1710.05029].

[174] K. T. Inoue, R. Takahashi, T. Takahashi and T. Ishiyama, *Constraints on warm dark matter from weak lensing in anomalous quadruple lenses*, *Mon. Not. Roy. Astron. Soc.* **448** (2015) 2704 [1409.1326].

[175] D. Gilman, S. Birrer, T. Treu, C. R. Keeton and A. Nierenberg, *Probing the nature of dark matter by forward modelling flux ratios in strong gravitational lenses*, *Mon. Not. Roy. Astron. Soc.* **481** (2018) 819 [1712.04945].

[176] S. Birrer, A. Amara and A. Refregier, *Lensing substructure quantification in RXJ1131-1231: A 2 keV lower bound on dark matter thermal relic mass*, *JCAP* **1705** (2017) 037 [1702.00009].

[177] EUCLID THEORY WORKING GROUP collaboration, *Cosmology and fundamental physics with the Euclid satellite*, *Living Rev. Rel.* **16** (2013) 6 [1206.1225].

[178] L. Amendola et al., *Cosmology and fundamental physics with the Euclid satellite*, *Living Rev. Rel.* **21** (2018) 2 [1606.00180].

[179] L. Gao and T. Theuns, *Lighting the Universe with filaments*, *Science* **317** (2007) 1527 [0709.2165].

[180] L. Gao, T. Theuns and V. Springel, *Star forming filaments in warm dark matter models*, *Mon. Not. Roy. Astron. Soc.* **450** (2015) 45 [1403.2475].

[181] S. Cantalupo, F. Arrigoni-Battaia, J. X. Prochaska, J. F. Hennawi and P. Madau, *A cosmic web filament revealed in Lyman-α emission around a luminous high-redshift quasar*, Nature **506** (2014) 63 [1401.4469].

[182] P. Madau, A. Meiksin and M. J. Rees, *21 Centimeter Tomography of the Intergalactic Medium at High Redshift*, *Astrophys. J.* **475** (1997) 429 [astro-ph/9608010].

[183] S. Tulin and H.-B. Yu, *Dark Matter Self-interactions and Small Scale Structure*, [1705.02358].

[184] XENON collaboration, *First Dark Matter Search Results from the XENON1T Experiment*, *Phys. Rev. Lett.* **119** (2017) 181301 [1705.06655].

[185] PANDAX-II collaboration, *Dark Matter Results From 54-Ton-Day Exposure of PandaX-II Experiment*, *Phys. Rev. Lett.* **119** (2017) 181302 [1708.06917].

[186] N. Y. Gnedin and L. Hui, *Probing the Universe with the Lyalpha forest - I. Hydrodynamics of the low-density intergalactic medium*, *Mon. Not. Roy. Astron. Soc.* **296** (1998) 44 [arXiv:astro-ph/9706219].

[187] L. Hui and N. Y. Gnedin, *Equation of state of the photoionized intergalactic medium*, *Mon. Not. Roy. Astron. Soc.* **292** (1997) 27 [astro-ph/9612232].

[188] F. Haardt and P. Madau, *Radiative Transfer in a Clumpy Universe. II. The Ultraviolet Extragalactic Background*, *Astrophys. J.* **461** (1996) 20 [astro-ph/9509093].

[189] T. Theuns, A. Leonard, G. Efstathiou, F. R. Pearce and P. A. Thomas, *P^3M-SPH simulations of the Lyalpha forest*, *Mon. Not. Roy. Astron. Soc.* **301** (1998) 478 [astro-ph/9805119].

[190] P. R. Upton Sanderbeck, A. D'Aloisio and M. J. McQuinn, *Models of the thermal evolution of the intergalactic medium after reionization*, *Mon. Not. Roy. Astron. Soc.* **460** (2016) 1885 [1511.05992].

[191] G. Giesen, J. Lesgourgues, B. Audren and Y. Ali-Haimoud, *CMB photons shedding light on dark matter*, *JCAP* **1212** (2012) 008 [1209.0247].

[192] V. Poulin, P. D. Serpico and J. Lesgourgues, *Dark Matter annihilations in halos and high-redshift sources of reionization of the universe*, *JCAP* **1512** (2015) 041 [1508.01370].

[193] V. Poulin, J. Lesgourgues and P. D. Serpico, *Cosmological constraints on exotic injection of electromagnetic energy*, *JCAP* **1703** (2017) 043 [1610.10051].

[194] SDSS collaboration, *Evidence for reionization at Z 6: Detection of a Gunn-Peterson trough in a Z = 6.28 quasar*, *Astron. J.* **122** (2001) 2850 [astro-ph/0108097].

[195] J. E. Gunn and B. A. Peterson, *On the Density of Neutral Hydrogen in Intergalactic Space.*, *Astrophys. J.* **142** (1965) 1633.

[196] D. K. Hazra and G. F. Smoot, *Witnessing the reionization history using Cosmic Microwave Background observation from Planck*, *JCAP* **1711** (2017) 028 [1708.04913].

[197] THE HISTORY OF REIONIZATION ARRAY collaboration, *A Roadmap for Astrophysics and Cosmology with High-Redshift 21 cm Intensity Mapping*, [1907.06440].

[198] I. Pris et al., *The Sloan Digital Sky Survey quasar catalog: tenth data release*, *Astron. Astrophys.* **563** (2014) A54 [1311.4870].

[199] P. J. Francis, P. C. Hewett, C. B. Foltz, F. H. Chaffee, R. J. Weymann and S. L. Morris, *A High Signal-to-Noise Ratio Composite Quasar Spectrum*, *Astrophys. J.* **373** (1991) 465.

[200] T. Theuns, A. Leonard, G. Efstathiou, F. R. Pearce and P. A. Thomas, *P**3M-SPH simulations of the lyman-alpha forest*, *Mon. Not. Roy. Astron. Soc.* **301** (1998) 478 [astro-ph/9805119].

[201] F. Haardt and P. Madau, *Radiative Transfer in a Clumpy Universe. II. The Ultraviolet Extragalactic Background*, *Astrophys. J.* **461** (1996) 20 [astro-ph/9509093].

[202] R. A. C. Croft, *Ionizing Radiation Fluctuations and Large-Scale Structure in the Ly alpha Forest*, *Astrophys. J.* **610** (2004) 642 [astro-ph/0310890].

[203] P. McDonald, U. Seljak, R. Cen, P. Bode and J. P. Ostriker, *Physical effects on the Lyα forest flux power spectrum: damping wings, ionizing radiation fluctuations and galactic winds*, *Mon. Not. Roy. Astron. Soc.* **360** (2005) 1471 [astro-ph/0407378].

[204] G. D. Becker, F. B. Davies, S. R. Furlanetto, M. A. Malkan, E. Boera and C. Douglass, *Evidence for Large-Scale Fluctuations in the Metagalactic Ionizing Background Near Redshift Six*, *ArXiv e-prints* (2018) [1803.08932].

[205] S. E. I. Bosman, X. Fan, L. Jiang, S. Reed, Y. Matsuoka, G. Becker et al., *New constraints on Lyman-α opacity with a sample of 62 quasarsat z ¿ 5.7*, *Mon. Not. Roy. Astron. Soc.* **479** (2018) 1055 [1802.08177].

[206] Planck Collaboration, R. Adam, N. Aghanim, M. Ashdown, J. Aumont, C. Baccigalupi et al., *Planck intermediate results. XLVII. Planck constraints on reionization history*, A&A **596** (2016) A108 [1605.03507].

[207] D. J. Mortlock, S. J. Warren, B. P. Venemans, M. Patel, P. C. Hewett, R. G. McMahon et al., *A luminous quasar at a redshift of z = 7.085*, Nature **474** (2011) 616 [1106.6088].

[208] F. B. Davies, J. F. Hennawi, E. Bañados, Z. Lukić, R. Decarli, X. Fan et al., *Quantitative Constraints on the Reionization History from the IGM Damping Wing Signature in Two Quasars at z ¿ 7*, *ArXiv e-prints* (2018) [1802.06066].

[209] J. Schaye, R. A. Crain, R. G. Bower and al., *The EAGLE project: simulating the evolution and assembly of galaxies and their environments*, *Mon. Not. Roy. Astron. Soc.* **446** (2015) 521 [1407.7040].

[210] J. Oñorbe, J. F. Hennawi and Z. Lukić, *Self-consistent Modeling of Reionization in Cosmological Hydrodynamical Simulations*, *Astrophys. J.* **837** (2017) 106 [1607.04218].

[211] F. Haardt and P. Madau, *Modelling the UV/X-ray cosmic background with CUBA*, in *Clusters of Galaxies and the High Redshift Universe Observed in X-rays*, D. M. Neumann and J. T. V. Tran, eds., ArXiv astro-ph/0106018, 2001, [arXiv:astro-ph/0106018].

[212] R. Scoccimarro, L. Hui, M. Manera and K. C. Chan, *Large-scale bias and efficient generation of initial conditions for nonlocal primordial non-Gaussianity*, Phys. Rev. D **85** (2012) 083002 [1108.5512].

[213] PLANCK collaboration, *Planck 2015 results. XIII. Cosmological parameters*, *Astron. Astrophys.* **594** (2016) A13 [1502.01589].

[214] M. Viel, J. Schaye and C. M. Booth, *The impact of feedback from galaxy formation on the Lyman α transmitted flux*, *Mon. Not. Roy. Astron. Soc.* **429** (2013) 1734 [1207.6567].

[215] A. Lewis, A. Challinor and A. Lasenby, *Efficient computation of CMB anisotropies in closed FRW models*, *Astrophys. J.* **538** (2000) 473 [astro-ph/9911177].

[216] J. Ghiglieri and M. Laine, *Improved determination of sterile neutrino dark matter spectrum*, *JHEP* **11** (2015) 171 [1506.06752].

[217] T. Venumadhav, F.-Y. Cyr-Racine, K. N. Abazajian and C. M. Hirata, *Sterile neutrino dark matter: Weak interactions in the strong coupling epoch*, *Phys. Rev.* **D94** (2016) 043515 [1507.06655].

[218] A. H. Pawlik, A. Rahmati, J. Schaye, M. Jeon and C. Dalla Vecchia, *The Aurora radiation-hydrodynamical simulations of reionization: calibration and first results*, *Mon. Not. Roy. Astron. Soc.* **466** (2017) 960 [1603.00034].

[219] T. Theuns, M. Viel, S. Kay, J. Schaye, R. F. Carswell and P. Tzanavaris, *Galactic Winds in the Intergalactic Medium*, *Astrophys. J.* **578** (2002) L5 [astro-ph/0208418].

[220] R. P. C. Wiersma, J. Schaye and B. D. Smith, *The effect of photoionization on the cooling rates of enriched, astrophysical plasmas*, *Mon. Not. Roy. Astron. Soc.* **393** (2009) 99 [0807.3748].

[221] G. Altay and T. Theuns, *URCHIN: a reverse ray tracer for astrophysical applications*, *Mon. Not. Roy. Astron. Soc.* **434** (2013) 748 [1304.4235].

[222] A. A. Meiksin, *The physics of the intergalactic medium*, *Reviews of Modern Physics* **81** (2009) 1405 [0711.3358].

[223] S. H. Hansen, J. Lesgourgues, S. Pastor and J. Silk, *Constraining the window on sterile neutrinos as warm dark matter*, *Mon. Not. Roy. Astron. Soc.* **333** (2002) 544 [astro-ph/0106108].

[224] M. Viel, J. Lesgourgues, M. G. Haehnelt, S. Matarrese and A. Riotto, *Constraining warm dark matter candidates including sterile neutrinos and light gravitinos with WMAP and the Lyman-alpha forest*, *Phys. Rev.* **D71** (2005) 063534 [astro-ph/0501562].

[225] J. Baur, N. Palanque-Delabrouille, C. Yèche, A. Boyarsky, O. Ruchayskiy, É. Armengaud et al., *Constraints from Ly-α forests on non-thermal dark matter including resonantly-produced sterile neutrinos*, J. Cosmology Astropart. Phys. **12** (2017) 013 [1706.03118].

[226] J. Miralda-Escude and M. J. Rees, *Tests for the minihalo model of the Lyman-alpha forest*, *Mon. Not. Roy. Astron. Soc.* **260** (1993) 617.

[227] N. Y. Gnedin and L. Hui, *Probing the Universe with the Lyalpha forest - I. Hydrodynamics of the low-density intergalactic medium*, *Mon. Not. Roy. Astron. Soc.* **296** (1998) 44 [astro-ph/9706219].

[228] A. Garzilli, T. Theuns and J. Schaye, *The broadening of Lyman-α forest absorption lines*, *Mon. Not. Roy. Astron. Soc.* **450** (2015) 1465 [1502.05715].

[229] A. Rorai, R. F. Carswell, M. G. Haehnelt, G. D. Becker, J. S. Bolton and M. T. Murphy, *A new measurement of the intergalactic temperature at z 2.55-2.95*, *Mon. Not. Roy. Astron. Soc.* **474** (2018) 2871 [1711.00930].

[230] T. Theuns, J. Schaye and M. G. Haehnelt, *Broadening of QSO Lyα forest absorbers*, *Mon. Not. Roy. Astron. Soc.* **315** (2000) 600 [astro-ph/9908288].

[231] SDSS collaboration, *The Ninth Data Release of the Sloan Digital Sky Survey: First Spectroscopic Data from the SDSS-III Baryon Oscillation Spectroscopic Survey*, *Astrophys. J.Suppl.* **203** (2012) 21 [1207.7137].

[232] J. Baur, N. Palanque-Delabrouille, C. Yèche, C. Magneville and M. Viel, *Lyman-alpha forests cool warm dark matter*, *JCAP* **1608** (2016) 012 [1512.01981].

[233] U. Seljak, A. Makarov, P. McDonald and H. Trac, *Can sterile neutrinos be the dark matter?*, *Phys. Rev. Lett.* **97** (2006) 191303 [astro-ph/0602430].

[234] A. Garzilli, A. Boyarsky and O. Ruchayskiy, *Cutoff in the Lyman α forest power spectrum: warm IGM or warm dark matter?*, *Phys. Lett.* **B773** (2017) 258 [1510.07006].

[235] V. Iršič, M. Viel, M. G. Haehnelt, J. S. Bolton, S. Cristiani, G. D. Becker et al., *New constraints on the free-streaming of warm dark matter from intermediate and small scale Lyman-α forest data*, Phys. Rev. D **96** (2017) 023522 [1702.01764].

[236] V. Iršič, M. Viel, M. G. Haehnelt, J. S. Bolton and G. D. Becker, *First constraints on fuzzy dark matter from Lyman-α forest data and hydrodynamical simulations*, *Phys. Rev. Lett.* **119** (2017) 031302 [1703.04683].

[237] R. Murgia, V. Iri and M. Viel, *Novel constraints on noncold, nonthermal dark matter from Lyman-α forest data*, *Phys. Rev.* **D98** (2018) 083540 [1806.08371].

[238] G. D. Becker, J. S. Bolton, M. G. Haehnelt and W. L. W. Sargent, *Detection of extended He II reionization in the temperature evolution of the intergalactic medium*, *Mon. Not. Roy. Astron. Soc.* **410** (2011) 1096 [1008.2622].

[239] A. P. Calverley, G. D. Becker, M. G. Haehnelt and J. S. Bolton, *Measurements of the UV background at 4.6 ¡ z ¡ 6.4 using the quasar proximity effect*, *Mon. Not. Roy. Astron. Soc.* **412** (2011) 2543 [1011.5850].

[240] G. D. Becker, M. Rauch and W. L. W. Sargent, *The Evolution of Optical Depth in the Ly-alpha Forest: Evidence Against Reionization at z 6*, *Astrophys. J.* **662** (2007) 72 [astro-ph/0607633].

[241] J. Baur, N. Palanque-Delabrouille, C. Yeche, A. Boyarsky, O. Ruchayskiy, . Armengaud et al., *Constraints from Ly-α forests on non-thermal dark matter including resonantly-produced sterile neutrinos*, *JCAP* **1712** (2017) 013 [1706.03118].

[242] N. Kaiser, *Clustering in real space and in redshift space*, *Mon. Not. Roy. Astron. Soc.* **227** (1987) 1.

[243] N. Kaiser and J. A. Peacock, *Power-spectrum analysis of one-dimensional redshift surveys*, *Astrophys. J.* **379** (1991) 482.

[244] C. McGill, *The redshift projection. I - Caustics and correlation functions*, *Mon. Not. Roy. Astron. Soc.* **242** (1990) 428.

[245] R. Scoccimarro, *Redshift-space distortions, pairwise velocities and nonlinearities*, *Phys. Rev.* **D70** (2004) 083007 [astro-ph/0407214].

[246] V. Desjacques and A. Nusser, *Redshift distortions in one-dimensional power spectra*, *Mon. Not. Roy. Astron. Soc.* **351** (2004) 1395 [astro-ph/0401544].

[247] H. J. Mo, Y. P. Jing and G. Borner, *Analytical approximations to the low-order statistics of dark matter distributions*, *Mon. Not. Roy. Astron. Soc.* **286** (1997) 979 [astro-ph/9607143].

[248] J. Miralda-Escudé and M. J. Rees, *Reionization and thermal evolution of a photoionized intergalactic medium.*, *Mon. Not. Roy. Astron. Soc.* **266** (1994) 343.

[249] T. Abel and M. G. Haehnelt, *Radiative Transfer Effects during Photoheating of the Intergalactic Medium*, *Astrophys. J.* **520** (1999) L13 [astro-ph/9903102].

[250] J. Miralda-Escude and J. P. Ostriker, *What produces the ionizing background at large redshift?*, *Astrophys. J.* **350** (1990) 1.

[251] M. McQuinn, *Constraints on X-ray emissions from the reionization era*, *Mon. Not. Roy. Astron. Soc.* **426** (2012) 1349 [1206.1335].

[252] L. Hui and Z. Haiman, *The Thermal Memory of Reionization History*, *Astrophys. J.* **596** (2003) 9 [astro-ph/0302439].

[253] J. Oñorbe, J. F. Hennawi, Z. Lukić and M. Walther, *Constraining Reionization with the z = 5-6 Ly alpha Forest Power Spectrum: The Outlook after Planck*, *Astrophys. J.* **847** (2017) 63 [1703.08633].

[254] P. Jakobsen, A. Boksenberg, J. M. Deharveng, P. Greenfield, R. Jedrzejewski and F. Paresce, *Detection of intergalactic ionized helium absorption in a high-redshift quasar*, Nature **370** (1994) 35.

[255] J. Schaye, T. Theuns, M. Rauch, G. Efstathiou and W. L. W. Sargent, *The thermal history of the intergalactic medium**, *Mon. Not. Roy. Astron. Soc.* **318** (2000) 817 [astro-ph/9912432].

[256] P. La Plante, H. Trac, R. Croft and R. Cen, *Helium Reionization Simulations. II. Signatures of Quasar Activity on the IGM*, *Astrophys. J.* **841** (2017) 87 [1610.02047].

[257] D. Syphers and J. M. Shull, *Hubble Space Telescope/Cosmic Origins Spectrograph Observations of the Quasar Q0302-003: Probing the He II Reionization Epoch and QSO Proximity Effects*, *Astrophys. J.* **784** (2014) 42.

[258] P. McDonald, J. Miralda-Escude, M. Rauch, W. L. W. Sargent, T. A. Barlow and R. Cen, *A measurement of the temperature-density relation in the intergalactic medium using a new Lyman-alpha absorption line fitting method*, *Astrophys. J.* **562** (2001) 52 [astro-ph/0005553].

[259] A. Lidz, C. A. Faucher-Giguere, A. Dall'Aglio, M. McQuinn, C. Fechner, M. Zaldarriaga et al., *A Measurement of Small Scale Structure in the 2.2 ¡ z ¡ 4.2 Lyman-alpha Forest*, *Astrophys. J.* **718** (2010) 199 [0909.5210].

[260] J. S. Bolton, G. D. Becker, S. Raskutti, J. S. B. Wyithe, M. G. Haehnelt and W. L. W. Sargent, *Improved measurements of the intergalactic medium temperature around quasars: possible evidence for the initial stages of He II reionization at z = 6*, *Mon. Not. Roy. Astron. Soc.* **419** (2012) 2880.

[261] G. D. Becker, J. S. Bolton, P. Madau, M. Pettini, E. V. Ryan-Weber and B. P. Venemans, *Evidence of patchy hydrogen reionization from an extreme Lyα trough below redshift six*, *Mon. Not. Roy. Astron. Soc.* **447** (2015) 3402 [1407.4850].

[262] J. Schaye, *Model-independent Insights into the Nature of the Ly alpha Forest and the Distribution of Matter in the Universe*, *Astrophys. J.* **559** (2001) 507 [arXiv:astro-ph/0104272].

[263] C. A. Faucher-Giguere, A. Lidz, M. Zaldarriaga and L. Hernquist, *A New Calculation of the Ionizing Background Spectrum and the Effects of HeII Reionization*, *Astrophys. J.* **703** (2009) 1416 [0901.4554].

[264] F. Haardt and P. Madau, *Radiative Transfer in a Clumpy Universe. IV. New Synthesis Models of the Cosmic UV/X-Ray Background*, *Astrophys. J.* **746** (2012) 125 [1105.2039].

[265] J. R. Pritchard and A. Loeb, *21 cm cosmology in the 21st century*, *Reports on Progress in Physics* **75** (2012) 086901 [1109.6012].